Characterisation of Paleochannels in Arid Environments Using P-band Synthetic Aperture Radar

Femke Graveland



Characterisation of Paleochannels in Arid Environments Using P-band Synthetic Aperture Radar

by

Femke Graveland

ESA Supervisor:	Björn Rommen
TU Delft Supervisor:	Prof. Dr. Ir. Evert C. Slob
External Committee Member:	Prof. Dr. Jan van der Kruk
Project Duration:	March 2026 - August 2026
Faculty:	Faculty of Civil Engineering and Geosciences, Delft University of Technology

TU Delft ETH zürich RWTH AACHEN UNIVERSITY

Preface

This thesis was conducted as part of the Joint Master's Programme in Applied Geophysics at TU Delft, ETH Zurich, and RWTH Aachen, and completed during an internship within the Climate Action, Sustainability and Science Department of the European Space Agency (ESA) at ESTEC in Noordwijk. The work explores the potential of the recently launched BIOMASS mission for the detection and characterisation of paleochannels in arid environments using P-band Synthetic Aperture Radar observations.

The past months have provided a unique opportunity to work at the intersection of remote sensing, geophysics, and planetary-scale Earth observation. Developing the methodology presented in this thesis required not only scientific investigation, but also extensive processing of newly available BIOMASS data and the exploration of approaches for interpreting subsurface signals in challenging desert environments. The opportunity to contribute to one of ESA's Earth Explorer missions during its commissioning phase has been both exciting and rewarding.

I would like to express my gratitude to my ESA supervisor, Björn Rommen, for providing this opportunity and for his continuous guidance, enthusiasm, and constructive feedback throughout the project. His expertise and encouragement were invaluable during both the scientific and practical aspects of this research. My sincere thanks go to my TU Delft supervisor, Evert Slob, for his guidance, critical insights, and thoughtful feedback throughout the thesis process. Finally, I would like to thank my family, friends, and fellow ESA intern colleagues for their support, patience, and encouragement throughout this project. In particular, I am grateful to everyone who provided feedback, technical assistance, or simply motivation during the final stages of writing and revision.

Femke Graveland
Delft, August 2026

Summary

Buried paleochannels preserved beneath aeolian sand provide valuable information on past hydrological conditions, landscape evolution, and potential groundwater resources. However, many of these features are concealed beneath metres of dry sediment and are therefore difficult to detect using optical remote sensing alone. The European Space Agency's BIOMASS mission provides the first fully polarimetric spaceborne P-band Synthetic Aperture Radar (SAR) observations, creating new opportunities for subsurface investigations in arid environments.

This thesis investigates the capability of BIOMASS P-band SAR to detect and characterize buried paleochannel systems in the Kufrah Basin (eastern Sahara) and the Paleo-Kuiseb system (Namib Desert). This thesis represents the first investigation of paleochannel detection and coherence-derived effective-depth retrieval using fully polarimetric spaceborne BIOMASS P-band SAR observations. A semi-physical workflow was developed that combines polarimetric amplitude and phase analysis, dielectric-roughness inversion, dielectric-equivalent moisture estimation, interferometric coherence analysis, and coherence-derived effective penetration depth retrieval. The methodology was supported by synthetic forward modelling, Monte Carlo uncertainty analysis, optical-radar data fusion, and geomorphological validation using drainage-network datasets and digital elevation models.

The results show that P-band observations reveal linear and dendritic geomorphological structures that are weakly expressed or absent in comparable L-band and optical imagery. Polarimetric decomposition indicates that the radar response is dominated primarily by surface and volume scattering, while double-bounce scattering is largely negligible. Several candidate paleochannel features are expressed consistently in amplitude imagery, decomposition products, coherence anomalies, and optical-radar fusion products. In contrast, the HH-VV co-polarized phase difference revealed organised drainage-like and dendritic spatial patterns that were broadly consistent with those observed in the amplitude imagery. However, phase-profile analysis did not identify a consistent paleochannel-specific signature, and channel-background phase contrasts remained small relative to the local spatial variability.

A dielectric-roughness inversion framework based on both a simplified Fresnel model and the Improved Integral Equation Model (I2EM) was implemented to estimate dielectric properties, effective roughness, dielectric-equivalent moisture content, and effective penetration depth. While the two inversion approaches produced different dielectric and roughness estimates, they yielded effective penetration depth products that agreed closely in spatial pattern, with a pixel-wise correlation of 0.924 and a mean bias of 0.067 m. This suggests that the coherence-derived depth retrieval is substantially more robust to the choice of backscatter model than the intermediate dielectric and roughness parameters.

Regional-scale application of the retrieval framework demonstrates that BIOMASS observations preserve coherent geomorphological patterns over hundreds of kilometres. In the Kufrah Basin, paleodrainage networks appear as elongated zones of elevated dielectric constant, elevated moisture-equivalent values, and reduced effective penetration depth. In the Namib Desert, the retrieval is strongly influenced by dune fields, drainage systems, interdune corridors, and bedrock-controlled terrain. Across both regions, the greatest effective penetration depths occur over broad, dry, and relatively homogeneous sandy surfaces, whereas reduced effective penetration depths are associated with areas of increased geomorphological complexity.

Synthetic forward modelling demonstrates that buried paleochannel structures can generate coherent anomalies in backscatter and interferometric coherence under favourable dry conditions. Monte Carlo analyses further show that the proposed framework is capable of reproducing the location and geometry of buried channel structures under realistic perturbations of environmental and acquisition parameters, although uncertainty increases where dielectric contrasts and burial depths are greatest.

The retrieved effective penetration depth estimates should not be interpreted as direct measurements of paleochannel burial depth. Instead, they represent effective coherence-derived penetration scales

describing the vertical extent over which coherent P-band scattering contributes to the interferometric response. Consequently, the resulting products are best interpreted as indicators of penetration potential and scattering-volume complexity rather than definitive subsurface maps.

Overall, the results demonstrate that BIOMASS P-band SAR provides a promising new capability for paleochannel investigations in arid environments. The principal contribution is the development of an integrated retrieval framework that combines polarimetric, interferometric, dielectric, and geomorphological information for identifying candidate paleochannel systems. Although direct subsurface validation remains necessary, the developed workflow provides a valuable regional screening tool that can guide future field investigations and support the reconstruction of paleohydrological networks in desert environments.

Contents

Preface i

Summary ii

Nomenclature xiii

1 Introduction 1

2 Theoretical Background 3
2.1 Synthetic Aperture Radar fundamentals . . . 3
2.1.1 Complex SAR measurements and interferometry . . . 3
2.2 Paleochannels in arid environments . . . 4
2.2.1 Representative paleochannel systems . . . 4
2.2.2 Flow directions of paleochannels . . . 5
2.3 Microwave subsurface imaging in arid environments . . . 6
2.4 Dielectric, moisture, and salinity controls on penetration . . . 6
2.4.1 Typical dielectric properties of arid environments . . . 6
2.4.2 Role of moisture and salinity . . . 7
2.4.3 Dielectric mixing models . . . 7
2.5 Scattering mechanisms relevant to paleochannel detection . . . 8
2.5.1 Surface scattering . . . 9
2.5.2 Volume scattering . . . 9
2.5.3 Odd- and double-bounce scattering . . . 9
2.5.4 Polarimetric decomposition . . . 9
2.6 HH-VV phase difference . . . 9
2.7 Effective penetration depth inversion . . . 10
2.7.1 Coherence as a proxy for subsurface structure . . . 10
2.7.2 Vertical wavenumber and sensitivity to depth . . . 11
2.7.3 Physical interpretation of effective penetration depth . . . 11

3 Methods 13
3.1 Study areas . . . 13
3.2 BIOMASS data products . . . 13
3.3 Amplitude and phase analysis . . . 14
3.3.1 Difference between L-band and P-band . . . 14
3.4 Effective penetration depth estimation . . . 15
3.4.1 Methodological overview . . . 15
3.4.2 Input data and pre-processing . . . 16
3.4.3 Interferometric coherence estimation . . . 17
3.4.4 Geometric and radiometric ancillary variables . . . 17
3.4.5 Radar wavelength and roughness parameter . . . 18
3.4.6 LUT Inversion . . . 18
3.4.7 Baseline, slant range, and vertical wavenumber . . . 22
3.4.8 Effective depth from coherence magnitude . . . 23
3.4.9 Regional-scale depth inversion . . . 24
3.5 Forward model and validation framework . . . 25
3.5.1 Model objective and role in the methodology . . . 26
3.5.2 Baseline configuration and model assumptions . . . 26
3.5.3 Scene representation and physical parameterisation . . . 28
3.5.4 Surface scattering contribution . . . 29
3.5.5 Subsurface scattering contribution . . . 30

3.5.6 Coherent superposition and copolar phase difference . . . 31
3.5.7 Simulated interferometric coherence . . . 32
3.5.8 Model outputs and detection observables . . . 33
3.5.9 Monte Carlo uncertainty quantification . . . 33
3.5.10 Geomorphological validation using D8 topographic modelling . . . 35
3.5.11 Optical corroboration of SAR-derived paleochannel candidates . . . 35

4 Results **37**
4.1 Preprocessing . . . 37
4.2 Phase and amplitude analysis . . . 38
4.2.1 Difference between L-band and P-band . . . 41
4.2.2 Decompositions . . . 42
4.3 Effective penetration depth inversion . . . 43
4.3.1 Comparison of Fresnel and I2EM retrieval results . . . 43
4.3.2 Volumetric moisture inversion . . . 46
4.3.3 Regional-scale effective penetration depth inversion results . . . 47
4.3.4 Ascending versus descending acquisitions . . . 50
4.4 Validation methods . . . 52
4.4.1 Validation model results . . . 53
4.4.2 Regional drainage network context . . . 53

5 Discussion **57**
5.1 Interpretation of P-band amplitude and phase signatures . . . 57
5.2 Scattering-mechanism interpretation . . . 58
5.3 Dielectric, roughness, and effective depth retrieval . . . 58
5.3.1 Consistency between observed backscatter and LUT Response . . . 58
5.3.2 Full swath effective depth inversion . . . 60
5.3.3 Influence of perpendicular baseline on effective penetration depth retrieval . . . 61
5.3.4 Influence of acquisition geometry . . . 63
5.3.5 Moisture interpretation . . . 63
5.4 Forward-model validation and uncertainty . . . 64
5.5 External validation and geomorphological consistency . . . 64
5.6 Limitations of the methodology . . . 65
5.7 Implications for BIOMASS paleochannel studies . . . 65
5.8 Future research directions . . . 66

6 Conclusion **68**

References **70**

A Relevant sections Research Module **75**
A.1 Principles of P-band SAR . . . 75
A.2 BIOMASS system and data acquisition . . . 75
A.2.1 Applications into arid environments . . . 76
A.3 Physics of electromagnetic propagation and subsurface scattering . . . 76

B Methodological details and sensitivity analyses **79**
B.1 Scene-centre baseline geometry . . . 79
B.2 Influence of multilooking on the co-polarization ratio . . . 80
B.3 Correlation-length parameterisation for the I2EM LUT . . . 81
B.4 Calibration of the roughness-activation function . . . 84
B.5 Lee filter window size selection . . . 86
B.6 Improved integral equation model (I2EM) . . . 86
B.6.1 Adaptations for Lookup-Table Inversion . . . 88

C Additional Results **89**
C.1 HH-VV phase difference analysis . . . 89
C.1.1 HV-VV phase difference analysis . . . 95
C.2 Additional Fresnel-I2EM retrieval diagnostics . . . 96
C.3 Additional ascending-descending comparison diagnostics . . . 99

C.4 Validation model . . . 104
C.4.1 Phase-profile response . . . 104
C.4.2 Monte Carlo retrieval statistics . . . 104
C.4.3 Profile-based retrieval assessment . . . 105

D Methods Evaluated During Development and Future Research Directions 107
D.1 Empirical HV-based moisture retrieval using the Oh et al. (1992) Model . . . 107
D.1.1 Original model . . . 107
D.1.2 Implemented simplification . . . 108
D.1.3 Reasons for exclusion . . . 108
D.1.4 Future research directions . . . 108
D.2 AIEM-Mironov physical moisture retrieval framework . . . 109
D.2.1 Original model . . . 109
D.2.2 Implemented simplification . . . 109
D.2.3 Reasons for exclusion . . . 109
D.2.4 Future research directions . . . 110
D.3 Decomposition-constrained multilayer coherence inversion . . . 110
D.3.1 Original concept . . . 110
D.3.2 Implemented approach . . . 110
D.3.3 Reasons for exclusion . . . 111
D.3.4 Future research directions . . . 111

E Automated topographic modeling using the D8 algorithm 112

F Code availability and statement on the use of artificial intelligence 114

List of Figures

2.1 BIOMASS Coverage and Interest Regions 5

3.1 Flowchart Depth Inversion 16
3.2 Geometry used for scene-centre estimation of the perpendicular baseline and slant range. The line-of-sight vector ℓ extends from the master satellite position $\mathbf{s}_1$ to the scene-centre target $\mathbf{x}_t$. The baseline vector $\mathbf{B}$ connects the master and secondary acquisition positions, and its component perpendicular to the line-of-sight defines the perpendicular baseline $B_\perp$. The slant range is given by $R = \|\boldsymbol{\ell}\|$. 23
3.3 Workflow of the synthetic forward-model and validation framework. 25
3.4 Conceptual geometry of the synthetic Bir Safsaf validation model. A buried calcified pebble-gravel paleochannel (CPG) is embedded within a small-pebble alluvium (SPA) background and covered by a uniform modern sand sheet (MSS). Complex dielectric permittivities assigned to each material are indicated. The channel burial depth d_{CPG} is 1.5 m. This simplified geometry was used to evaluate the sensitivity of the forward model to dielectric contrasts and subsurface channel structure. 26
3.5 Synthetic paleochannel model used for validation. Shown are the prescribed channel membership, surface-depth variation, buried-layer dielectric properties, moisture content, roughness, incidence angle, dimensionless roughness (k_s), and vertical wavenumber ($k_{z,\mathrm{vol}}$). 27

4.1 Comparison between a single HH intensity acquisition acquired on 1 May 2026 and a temporally stacked HH intensity image generated from acquisitions between 28 April and 13 May 2026. 38
4.2 Stacked HH, HV, VH, and VV backscatter images for the reference scene located in the Sahara acquired in May 2026. For visualisation purposes, the cross-polarized channels (HV and VH) are displayed using a different intensity scale than the co-polarized channels (HH and VV) because of their substantially lower backscatter levels. 39
4.3 Wrapped HH phase, wrapped VV phase, and the corresponding HH-VV phase difference for the Sahara study area. Phase values are displayed in the range $[-\pi, \pi]$ rad. 40
4.4 HH-VV phase-difference imagery displayed over the full BIOMASS swath coverage. The red polygon indicates the reference scene analysed in this study. Right: enlarged view of the highlighted area showing coherent drainage-like and dendritic phase patterns visible within the phase-difference product. 41
4.5 Comparison of the study area in BIOMASS P-band imagery, the JAXA ALOS PALSAR-2 annual L-band mosaic, and optical imagery displayed in Google Earth. The red, blue, and yellow boxes highlight representative features discussed in the text. 41
4.6 Pauli RGB decomposition and corresponding decomposition components for the Sahara study area. In the Pauli RGB image, blue represents odd-bounce scattering, green represents volume scattering, and red represents even-bounce scattering. The optical image is included for visual comparison, while the three panels on the right show the individual odd-bounce, even-bounce, and volume scattering components. 43
4.7 Input datasets used for the depth inversion workflow, including HH backscatter (σ^0_{HH}), VV backscatter (σ^0_{VV}), interferometric coherence ($|\gamma|$), and incidence angle (θ). 44
4.8 Comparison of retrieval results obtained using the Fresnel LUT (left column) and I2EM LUT (centre column). The right column shows the corresponding difference maps ($\mathrm{Fresnel} - \mathrm{I2EM}$) for dielectric constant, normalised roughness, and effective penetration depth. . 45
4.9 Pixel-wise comparison of Fresnel and I2EM retrievals for dielectric constant, normalised roughness, and effective penetration depth. The red line denotes the one-to-one relationship. 46

4.10 Three-dimensional visualisation of the effective penetration depth derived from the Fresnel LUT (Model 1), the I2EM LUT (Model 2), and the resulting difference ($d_{\mathrm{eff,M1}} - d_{\mathrm{eff,M2}}$). The retrieved values represent the estimated subsurface volume from which detectable radar backscatter could potentially originate rather than the depth to a discrete buried reflector. 46
4.11 Comparison of dielectric-equivalent moisture retrievals obtained using the Topp, Dobson, and CRIM dielectric mixing models. The upper row shows moisture estimates derived from the Fresnel inversion framework, whereas the lower row shows moisture estimates derived from the I2EM inversion framework. 47
4.12 Regional retrieval results for the Kufrah Basin derived from BIOMASS Level-1C observations. The retrieved dielectric constant (ε') and effective penetration depth (d_{eff}) products exhibit spatially coherent patterns across multiple adjacent BIOMASS frames. Several linear and dendritic anomalies remain continuous over large distances and are visible across frame boundaries, demonstrating the preservation of regional-scale geomorphological structure within the inversion products. 48
4.13 Regional retrieval results for the southern transition zone between the Sahara and the Sahel. From left to right: effective penetration depth (d_{eff}), dielectric-equivalent volumetric moisture content (m_v), and dielectric constant (ε'). The retrievals show a pronounced regional transition from hyper-arid desert conditions in the north to increasingly elevated dielectric and moisture-equivalent responses toward the south, accompanied by reduced effective penetration depths. 49
4.14 Regional retrieval results for the Namib Desert study area derived from BIOMASS Level-1C observations. From left to right: effective penetration depth retrieved from the descending acquisition, effective penetration depth retrieved from the ascending acquisition, retrieved dielectric constant (ε'), and dielectric-equivalent volumetric moisture content (m_v). 50
4.15 Comparison of ascending and descending retrieval products. Rows show dielectric constant, volumetric moisture content, and effective penetration depth. Difference maps are computed as ascending minus descending. 51
4.16 Comparison of effective penetration depth retrieved from ascending and descending acquisitions. 52
4.17 Simulated BIOMASS observables derived from the synthetic paleochannel model. Panels show HH and VV backscatter, co-polarized backscatter differences, HH-VV phase difference, HH and VV coherence, analytical coherence, attenuation, and layer-induced phase delay. 53
4.18 HydroRIVERS drainage network overlaid on the BIOMASS acquisition swaths. (a) Regional overview of the drainage network across the full acquisition area. Blue lines represent HydroRIVERS channels and grayscale imagery corresponds to the BIOMASS scenes. (b) Detailed view of the analysis region, outlined by the red polygon, showing the density and spatial organization of drainage pathways within the study area. HydroRIVERS data are derived from the HydroSHEDS hydrographic database (Lehner & Grill, 2013). 54
4.19 Drainage-network extraction derived from the digital elevation model using a D8 flow-routing algorithm. Panels show the DEM input, sink-filled DEM, D8 flow-direction index, logarithmically scaled flow accumulation, and stream masks derived using flow-accumulation thresholds of 100 and 500 pixels. 54
4.20 Comparison of BIOMASS-derived paleochannel indicators with Sentinel-2 optical imagery and ancillary datasets. Shown are the Sentinel-2 RGB composite, BIOMASS coherence, coherence anomaly, phase anomaly, NDWI-derived moisture indicator, clay mineral index, bare soil index, vegetation index, radar texture, flow accumulation, combined paleochannel score, and the final paleochannel detection overlay. 56

5.1 Comparison between observed STA-derived backscatter distributions and the scattering responses represented within the I2EM lookup table at the median scene incidence angle ($25.2°$). Left: HH-VV backscatter space showing observed measurements and achievable LUT responses. Centre: distribution of the co-polarization difference ($VV - HH$). Right: marginal HH and VV distributions. While the absolute HH and VV backscatter levels are reproduced reasonably well, the observed polarization difference is systematically shifted towards lower values than predicted by the LUT. 59
5.2 Retrieved dielectric constant (ε') and normalised roughness (k_s) as a function of the observed co-polarization difference ($VV - HH$). The red dashed line denotes the minimum polarization difference represented within the lookup table. Retrievals associated with low observed $VV - HH$ values increasingly accumulate at LUT boundaries, indicating that observations near the edge of the modelled parameter space force solutions towards the limits of the inversion domain. 59
5.3 Influence of perpendicular baseline selection on retrieved effective penetration depth. (a) Relationship between absolute perpendicular baseline magnitude and median retrieved effective penetration depth for all analysed scene pairs. Colours indicate different BIOMASS stacks and the dashed line shows the pooled linear regression. (b) Distribution of median retrieved effective penetration depths obtained from all available baseline pairings within each BIOMASS stack. Boxes indicate the interquartile range, horizontal lines indicate the median, and individual points correspond to retrievals derived from different baseline pairs. 61
5.4 Example of baseline-dependent effective penetration depth retrievals for a single BIOMASS stack. Different baseline pairs produce systematically different median effective penetration depth estimates despite originating from the same acquisition stack. 62
5.5 Retrieved effective penetration depth maps for all available baseline pairs within the representative BIOMASS stack shown in Figure 5.4. The spatial distribution of the effective penetration depth anomalies remains largely consistent, whereas the absolute depth magnitude varies with baseline selection. 62

B.1 Sensitivity of the observed co-polarization difference ($VV - HH$) to multilooking window size. Histograms (left column) and HH-VV scatter clouds (right column) are shown for multilooking factors of 12×2, 24×4, and 36×6 pixels. The red dashed line indicates the median observed polarization difference, whereas the black dotted line denotes the minimum $VV - HH$ value represented within the LUT. The discrepancy remains largely unchanged across all multilooking configurations. 81
B.2 Sensitivity of simulated HH and VV backscatter to the assumed correlation-length-to-RMS-height ratio (L/s) for representative roughness values at $\varepsilon' = 3.0$ and $\theta = 26°$. . . 82
B.3 Influence of L/s mismatch on the retrieved dielectric constant and roughness parameter. Synthetic observations were generated using different true correlation-length ratios and inverted using a LUT constructed with the nominal value $L/s = 6$. The dashed line indicates the ratio used in the LUT generation. 83
B.4 Calibration of the empirical roughness-activation function against the normalised I2EM roughness response. Left: comparison between the normalised I2EM response and the adopted activation function. Middle: fitted β values obtained for different representative dielectric constants with $a = 1$ fixed. Right: fitted β values obtained for different correlation-length assumptions. 85
B.5 Lee Filter Size Comparison 86

C.1 Location of the extracted HH-VV phase-difference cross-sections for the first Sahara region of interest. The highlighted regions indicate the mapped paleochannel extent and the profile locations used for analysis. 90
C.2 Range and azimuth profiles of the HH-VV phase difference extracted through the paleochannel in the first Sahara region of interest. Shaded regions indicate the mapped channel extent. 91

C.3 Location of the extracted HH-VV phase-difference cross-sections for the second Sahara region of interest. The highlighted regions indicate the mapped paleochannel extent and the profile locations used for analysis. 92
C.4 Range and azimuth profiles of the HH-VV phase difference extracted through the paleochannel in the second Sahara region of interest. Shaded regions indicate the mapped channel extent. 93
C.5 Definition of the channel and background regions used for the HH-VV phase-difference analysis in the region of interest. The magenta box denotes the interpreted paleochannel region, while the cyan boxes denote neighbouring background regions used for comparison. The grayscale image corresponds to the stacked BIOMASS backscatter. 94
C.6 Azimuth-averaged HH-VV phase-difference profile extracted across the region of interest. The magenta shaded region indicates the interpreted paleochannel extent, while the grey shaded regions indicate the background reference areas. Horizontal dashed lines denote the mean phase differences within the channel and background regions. Although local phase variations are present, the channel and background means differ by only approximately 0.001 rad, indicating no pronounced paleochannel-specific phase signature. 95
C.7 Wrapped HV phase, wrapped VV phase, and the corresponding HV-VV phase difference for the Sahara study area. Phase values are displayed in the range $[-\pi, \pi]$ rad. 96
C.8 Comparison of intermediate retrieval products derived using the Fresnel LUT (Model 1) and I2EM LUT (Model 2). Rows show normalised roughness (k_s), RMS roughness, and dielectric-corrected vertical wavenumber (k_z). The right column presents the corresponding difference maps (Model 1 minus Model 2). Substantial differences are observed in the retrieved roughness parameters, whereas the resulting vertical wavenumber products exhibit greater spatial consistency despite localized variations. 97
C.9 Regional normalised surface roughness (k_s) retrieval derived from the I2EM inversion framework for the full BIOMASS coverage of the Kufrah Basin. The product exhibits substantial spatial variability across the regional mosaic and highlights broad geomorphological contrasts between homogeneous desert surfaces and more heterogeneous terrain. Several linear, branching, and localized anomalies remain visible across multiple BIOMASS frames, while scene-to-scene variations are also apparent throughout the regional swath. 98
C.10 Overlap between the ascending and descending BIOMASS acquisitions. 99
C.11 Comparison of effective penetration depth retrievals derived from ascending and descending acquisitions. 99
C.12 Comparison of dielectric constant retrievals derived from ascending and descending acquisitions. 100
C.13 Empirical cumulative distribution of absolute depth differences between ascending and descending retrievals. 100
C.14 Empirical cumulative distribution of absolute dielectric differences between ascending and descending retrievals. 101
C.15 Median depth difference as a function of incidence angle. 101
C.16 Median dielectric difference as a function of incidence angle. 102
C.17 Overlay of ascending and descending depth products within the overlapping region. . . 103
C.18 Cross-channel profile through the centre of the synthetic paleochannel showing the HH-VV phase difference together with the normalised channel-membership function and buried-reflector geometry. 104
C.19 Monte Carlo mean and standard-deviation maps for dielectric constant, moisture content, and buried-reflector depth obtained from repeated perturbations of acquisition and environmental parameters. 105
C.20 Cross-channel profiles showing Monte Carlo mean estimates, nominal solutions, and 5th-95th percentile uncertainty bounds for dielectric constant, moisture content, and buried-reflector depth. 105

C.21 Coherence-derived burial-depth estimation. The left panel shows the retrieved depth profile together with Monte Carlo uncertainty bounds and the prescribed burial depth. The right panel illustrates the predicted relationship between burial depth and retrieval uncertainty obtained from first-order noise propagation. 106

List of Tables

2.1 Representative relative dielectric constants of dry sand in arid environments reported in literature. 7

3.1 BIOMASS Level-1C STA datasets used in this study. 14
3.2 Nominal parameter ranges used in the joint HH-VV and I2EM-LUT inversions. 18
3.3 Nominal parameter values used in the baseline Bir Safsaf forward-model simulation. . . 28
3.4 Input-parameter uncertainty specification used in the Monte Carlo uncertainty propagation. Relative uncertainties are defined as fractions of the nominal parameter value, while absolute uncertainties are specified in native units. 34
3.5 Weights assigned to the indicators used in the composite paleochannel score. 36

Nomenclature

Symbol	Description
ε^*	Complex dielectric permittivity
ε'	Real part of dielectric permittivity (dielectric constant)
ε''	Imaginary part of dielectric permittivity (dielectric loss factor)
m_v	Volumetric soil moisture content
ϕ	Porosity
S_w	Water saturation
f	Radar frequency
λ	Radar wavelength
c	Speed of light in vacuum
θ	Local incidence angle
θ_t	Transmission angle within the medium
σ^0	Normalised radar backscatter coefficient
S	Complex SAR signal
$\phi_{\mathrm{HH-VV}}$	Co-polarized phase difference (CPD)
γ	Complex interferometric coherence
$\lvert\gamma\rvert$	Coherence magnitude
$B_\perp$	Perpendicular interferometric baseline
R	Slant range distance
k_z	Vertical wavenumber
$k_{z,\mathrm{vol}}$	Dielectric-corrected vertical wavenumber
d	Buried reflector depth
d_{eff}	Effective coherence-derived penetration depth
s	RMS surface height
k_s	Dimensionless surface roughness parameter
R_{pp}	Fresnel reflection coefficient for polarization pp
T_{pp}	Fresnel transmission coefficient for polarization pp
G_r	Roughness activation function
E_{surf}	Surface-scattering contribution
E_{sub}	Subsurface-scattering contribution
E_{tot}	Total scattered field
α_e	Electromagnetic attenuation coefficient
ϕ_{prop}	Propagation phase delay
M	Continuous paleochannel membership function
C	Binary paleochannel mask
H	Polarimetric entropy
A	Polarimetric anisotropy
α	Cloude-Pottier alpha angle
N_{MC}	Number of Monte Carlo realizations
σ_Φ	Standard deviation of simulated CPD
θ_i	Incidence angle in air
k	Radar wavenumber ($2\pi/\lambda$)
L	Surface correlation length
η	Correlation-length-to-RMS-height ratio
$\tan\delta$	Dielectric loss tangent
J	LUT inversion cost function

1

Introduction

Arid and hyperarid regions preserve extensive records of past hydrological activity in the form of buried or abandoned drainage networks, commonly referred to as paleochannels. These fossil river systems provide critical evidence of former humid climatic phases, constrain the long-term evolution of desert landscapes, and could host groundwater resources that remain essential in water-scarce regions (Paillou, 2017; Paillou et al., 2020; Ul Islam et al., 2016). In many deserts, paleochannels are buried beneath meters of aeolian sand, rendering them largely invisible to optical remote sensing, which primarily reflects surface mineralogy and vegetation cover (Kim, 2023; Ul Islam et al., 2016).

Synthetic Aperture Radar (SAR) offers a unique capability to overcome this limitation. As an active microwave remote sensing technique, SAR can penetrate dry, low-loss materials such as aeolian sand, allowing subsurface structures to influence the observed backscatter amplitude and phase (Grandjean et al., 2001; Paillou, 2017). Numerous studies have demonstrated that low-frequency SAR systems, particularly L-band, are capable of revealing buried paleodrainage systems in desert environments including the Sahara, Namib, and Thar deserts (Monika et al., 2022; Paillou et al., 2012; Ul Islam et al., 2016). However, L-band penetration depth remains limited in many settings, especially where moisture, salinity, or surface roughness introduce attenuation and decorrelation (Lasne et al., 2008; Liu et al., 2021).

The European Space Agency's (ESA) BIOMASS mission represents a major advance in radar remote sensing of terrestrial environments. As ESA's seventh Earth Explorer mission, BIOMASS was primarily designed to measure global forest above-ground biomass and improve estimates of the terrestrial carbon cycle (Le Toan et al., 2011). Following its launch in April 2025, BIOMASS remains in the early stages of its operational lifetime, with new observations continuing to be acquired and released. Consequently, investigations exploiting spaceborne P-band SAR data represent a highly current and rapidly developing area of research. The mission carries the first spaceborne P-band SAR operating at 432-438 MHz, a frequency range capable of penetrating vegetation canopies as well as dry, low-loss desert sands (Le Toan et al., 2011; Paillou, 2017).

In hyperarid environments, P-band signals may penetrate several metres into aeolian sand sheets, enabling the detection of buried paleochannels and other subsurface geomorphological features that remain inaccessible to higher-frequency spaceborne SAR systems (Grandjean et al., 2001; Paillou, 2017). In addition, BIOMASS provides fully polarimetric observations, allowing the exploitation of phase, coherence, and scattering characteristics as indicators of subsurface structure and dielectric heterogeneity (Cloude & Papathanassiou, 1998; Lasne et al., 2008).

Despite this potential, several challenges complicate the interpretation of P-band SAR observations in desert environments. Subsurface penetration is not a directly measurable quantity, but an effective outcome of complex interactions between wavelength, acquisition geometry, scattering mechanisms, and the dielectric properties of the medium (Lasne et al., 2008; Ulaby & Long, 2014). Variations in soil moisture, salinity, mineral composition, and surface roughness may affect radar observables in competing or non-unique ways (Paillou et al., 2003; Shahidi et al., 1975). Furthermore, coherence-

based indicators of penetration depth are sensitive not only to subsurface structure but also to non-geophysical factors such as spatial heterogeneity, noise, and acquisition geometry. (Xiong et al., 2017).

Although the capability of SAR, and particularly low-frequency L-band SAR, to detect buried drainage systems has been demonstrated in a variety of arid environments (Monika et al., 2022; Paillou, 2017; Paillou et al., 2009, 2012, 2020; Ul Islam et al., 2016), the conditions under which such detections remain reliable are still not fully understood. Previous studies have primarily relied on L-band spaceborne observations and airborne radar campaigns, whereas the potential of fully polarimetric spaceborne P-band observations has not yet been systematically investigated. In particular, the combined influence of dielectric contrast, acquisition geometry, moisture variability, and scattering depth on P-band observables remains difficult to quantify in the absence of direct subsurface measurements. Furthermore, while coherence-based depth retrieval approaches have been explored using L-band SAR (Liu et al., 2021; Zhu et al., 2023), their applicability to spaceborne P-band observations has not yet been systematically evaluated.

This thesis addresses these knowledge gaps through three research questions:

1. How do dielectric contrast, reflection depth, and surface roughness influence the sensitivity of copolarized phase difference (CPD) and interferometric coherence to buried paleochannel structure?
2. Can physically interpretable estimates of effective penetration depth be derived from spaceborne P-band SAR observations in the absence of direct subsurface validation data?
3. How sensitive are CPD, coherence, and effective-depth estimates to uncertainty in soil moisture and surface roughness, and under which conditions do the retrievals become unreliable or non-unique?

Because no coincident subsurface validation data are available for the analysed BIOMASS acquisitions, the objective is not to retrieve true paleochannel burial depth. Instead, the developed framework seeks to derive physically interpretable indicators of penetration potential and scattering-volume structure that may be associated with buried paleodrainage systems. The resulting products are therefore intended as regional-scale screening tools rather than definitive subsurface reconstructions.

This thesis contributes to addressing these knowledge gaps through the development of an integrated retrieval framework for paleochannel characterisation using fully polarimetric BIOMASS P-band observations. The framework integrates dielectric, polarimetric, interferometric, and geomorphological information to identify and characterize candidate paleochannel systems. In addition, a synthetic forward model and Monte Carlo sensitivity analysis are used to evaluate retrieval performance across a range of realistic environmental conditions and to identify the conditions under which CPD, coherence, and effective-depth estimates remain sensitive to subsurface structure rather than being dominated by decorrelation, noise, or retrieval non-uniqueness.

The remainder of this thesis is structured as follows. Chapter 2 reviews the physical principles underlying microwave subsurface imaging in desert environments, including dielectric behaviour, scattering mechanisms, polarimetric observables, and penetration-depth theory. Chapter 3 describes the data, processing workflow, inversion methodology, and validation framework developed in this thesis. Chapter 4 presents the results of the paleochannel detection, retrieval experiments, and validation analyses. Chapter 5 discusses the interpretation of the retrieved observables, evaluates the robustness and limitations of the proposed methodology, and places the findings in the context of previous paleochannel and subsurface SAR studies. Finally, Chapter 6 revisits the research questions, summarizes the principal findings, and outlines implications and recommendations for future BIOMASS-based paleochannel investigations.

2

Theoretical Background

2.1. Synthetic Aperture Radar fundamentals

Synthetic Aperture Radar (SAR) is an active microwave remote sensing technique that produces high-resolution imagery by transmitting electromagnetic pulses and measuring the radiation backscattered from the Earth's surface (Abdelkareem et al., 2020). Unlike optical sensors, SAR operates independently of solar illumination and is only weakly affected by atmospheric conditions, enabling reliable day-and-night observations under nearly all weather conditions (Nurmemet et al., 2025). The radar backscatter response depends on surface roughness, geometry, and dielectric properties, which are strongly controlled by soil moisture and salinity. These properties make SAR particularly valuable for environmental and geophysical studies, including the detection of buried geomorphological structures in arid environments (Paillou, 2017).

Polarization in SAR refers to the orientation of the electric field vector of the transmitted and received electromagnetic waves. By exploiting different combinations of horizontal (H) and vertical (V) polarization states, Polarimetric Synthetic Aperture Radar (PolSAR) enables the retrieval of complementary information on the physical, dielectric, and geometric properties of surface and subsurface targets (Cloude & Papathanassiou, 1998). Current SAR systems operate in single-polarization, dual-polarization, or full-polarimetric modes. Full-polarimetric, or quad-pol, systems measure the complete 2×2 Sinclair scattering matrix composed of the HH, HV, VH, and VV channels, where the first and second letters denote the transmit and receive polarizations, respectively. (Ulaby & Long, 2014).

In arid environments, co-polarized channels (HH and VV) are commonly used for penetration and coherence analyses, while cross-polarized returns (HV/VH) provide additional sensitivity to heterogeneous and volumetric scattering processes (Abdelkareem et al., 2020; Liu et al., 2021; Paillou, 2017).

2.1.1. Complex SAR measurements and interferometry

The radar observations described above are recorded as complex-valued measurements containing both amplitude and phase information. For each pixel, the received signal can be expressed as

$$S = Ae^{j\phi}, \tag{2.1}$$

where A denotes the signal amplitude and ϕ the signal phase. The amplitude primarily describes the strength of the radar return and is influenced by the dielectric properties, roughness, and geometry of the observed target. The phase contains information about the propagation path length and is therefore sensitive to subtle changes in topography, dielectric properties, and subsurface structure. While amplitude forms the basis of conventional SAR imagery, many advanced retrieval techniques exploit the phase information contained within the complex signal. One of the most widely used phase-based techniques is Interferometric SAR (InSAR), which exploits the phase difference between two SAR acquisitions observing the same area from slightly different positions.

The complex interferogram is formed by multiplying one acquisition with the complex conjugate of the second,

$$I = S_1 S_2^*, \tag{2.2}$$

where S_1 and S_2 are the complex SAR measurements and $(\cdot)^*$ denotes complex conjugation. The resulting interferometric phase contains information about the relative propagation path difference between the two observations.

A key geometric parameter in interferometric SAR is the perpendicular baseline $B_\perp$, defined as the separation between the acquisition positions projected perpendicular to the radar line-of-sight. Together with the radar wavelength, incidence angle, and slant range, the baseline determines the sensitivity of the interferometric measurement to vertical structure through the vertical wavenumber. In low-loss arid environments, where radar signals may penetrate several metres into dry sediments, this sensitivity forms the basis for coherence-based investigations of subsurface scattering structure.

Interferometric coherence quantifies the similarity between two complex SAR observations and ranges between zero and one. High coherence indicates stable and spatially homogeneous scattering behaviour, whereas reduced coherence may result from temporal decorrelation, geometric decorrelation, noise, or distributed subsurface scattering. In this thesis, interferometric coherence forms the primary observable used in the effective depth-retrieval framework described in Chapter 3.4.8. Only the concepts required for understanding the retrieval methodology are introduced here. A more detailed discussion of SAR signal formation, BIOMASS acquisition geometry, P-band imaging principles, and interferometric processing is provided in Appendix A.

BIOMASS operates as a fully polarimetric P-band SAR system, enabling the combined analysis of amplitude, phase, coherence, and polarimetric observables for subsurface investigations. Further information on the BIOMASS acquisition concept and system characteristics is presented in Appendix A.

2.2. Paleochannels in arid environments

The principal subsurface target considered in this thesis is the paleochannel. Paleochannels are buried or abandoned relic drainage systems that are no longer active at the surface (Monika et al., 2022; Ul Islam et al., 2016). In arid environments, they are commonly preserved beneath aeolian sand cover and may occur as former river channels, alluvial deposits, paleosoils, or other fluvial landforms that record past hydrological and geomorphological conditions (Paillou, 2017; Paillou et al., 2020). Because these features are often concealed beneath dry sediments, their identification typically requires geophysical or remote-sensing techniques capable of probing the shallow subsurface.

Detection using optical remote sensing alone is frequently challenging, as optical sensors primarily capture surface characteristics such as vegetation, mineral composition, and albedo (Kim, 2023; Ul Islam et al., 2016). In contrast, Synthetic Aperture Radar (SAR) can penetrate dry surficial sand under favourable conditions, enabling the detection of buried drainage structures in hyperarid regions including the Sahara, Namib, and Thar deserts (Monika et al., 2022; Paillou, 2017; Paillou et al., 2012). Depending on the composition of the channel fill and surrounding sediments, paleochannels may appear as either bright or dark linear features in SAR imagery. Their detectability is fundamentally controlled by the penetration of microwave signals into dry desert sediments, which depends on radar wavelength and the electromagnetic properties of the subsurface.

2.2.1. Representative paleochannel systems

Several paleochannel systems have been extensively investigated using SAR observations and provide important examples of buried drainage networks in arid environments. Among the most well documented are the Kufrah paleodrainage system in North Africa and the Paleo-Kuiseb system in Namibia. These areas overlap with the BIOMASS Data coverage (Figure 2.1).

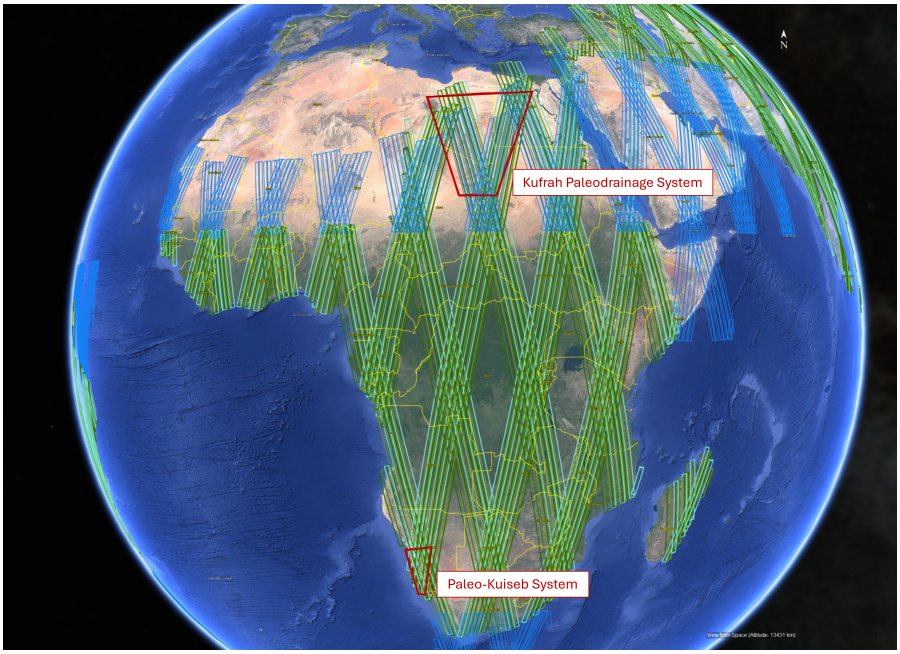

Figure 2.1: BIOMASS Coverage and Interest Regions

The Kufrah paleodrainage system

The Kufrah paleodrainage system in eastern Libya is one of the largest known buried river systems in the Sahara. Previous SAR investigations using SIR-A/B and ALOS PALSAR revealed extensive paleochannels concealed beneath aeolian sand cover, where detection is facilitated by dielectric and roughness contrasts between buried fluvial materials and the overlying sand sheet (Paillou, 2017; Paillou et al., 2012).

The Paleo-Kuiseb system

The Paleo-Kuiseb system in the Namib Desert provides a contrasting example of paleodrainage preservation within an active dune field. ALOS-2 PALSAR-2 observations revealed paleochannel remnants preserved between linear dunes, documenting progressive northward migration of the river system during dune encroachment (Paillou et al., 2020).

Together, the Kufrah and Paleo-Kuiseb systems provide representative examples of paleodrainage preservation in arid environments and demonstrate the capability of SAR observations to reveal buried fluvial structures beneath extensive sand cover.

2.2.2. Flow directions of paleochannels

Flow direction can provide useful geomorphological context when distinguishing paleochannels from other linear landforms. Because drainage pathways are controlled by regional topography and geological structure, Digital Elevation Models (DEMs) are commonly used to identify drainage patterns and basin-scale gradients associated with former fluvial systems. However, the original surface expression of paleochannels is often obscured by aeolian deposition in hyperarid environments, limiting the effectiveness of topographic analysis alone (Kim, 2023; Paillou, 2017; Ul Islam et al., 2016). In the Kufrah Basin, previously mapped paleodrainage systems generally exhibit northeast-southwest orientations linked to regional structural and topographic controls (Paillou et al., 2012). In the Namib Desert, the Paleo-Kuiseb system trends approximately southeast-northwest towards the Atlantic coast and has been modified by long-term dune migration (Paillou et al., 2020). Consequently, flow direction should be regarded as a supporting indicator and interpreted together with SAR observations and other geomorphological evidence rather than as a definitive criterion for paleochannel identification (Abdelkareem et al., 2020; Monika et al., 2022; Paillou, 2017).

2.3. Microwave subsurface imaging in arid environments

The ability of SAR to image subsurface features depends primarily on sensor wavelength and the dielectric properties of the medium (Grandjean et al., 2001; Liu et al., 2021). Longer wavelengths generally achieve greater penetration into dry, low-loss materials such as aeolian sand. These wind-deposited sediments, which form dunes and sand sheets in arid environments, are particularly favourable for microwave subsurface imaging because of their low moisture content, low dielectric permittivity, and low dielectric losses (Liu et al., 2021; Monika et al., 2022; Paillou, 2017).

Reported penetration depths increase with wavelength, ranging from approximately 0.2-0.5 m at C-band (4-8 GHz), 0.8-2.9 m at L-band (1-2 GHz), and expected 5-14 m at P-band (0.435 GHz) under very dry conditions (Grandjean et al., 2001; Liu et al., 2021; Paillou, 2017; Ul Islam et al., 2016). Controlled airborne microwave experiments in the Negev Desert have confirmed the detection of buried objects at comparable frequencies, supporting these theoretical estimates (Daniels et al., 2003). A review of previous SAR subsurface-imaging studies in arid environments is provided in Appendix A.2.1.

The increased penetration of lower-frequency radar systems arises from reduced electromagnetic attenuation within dry sediments. For a plane wave propagating through a low-loss dielectric medium, the attenuation coefficient α is approximately proportional to

$$\alpha \propto f\sqrt{\varepsilon''}, \tag{2.3}$$

where α is the electromagnetic attenuation coefficient, f is frequency, and ε'' is the dielectric loss factor.

Lower radar frequencies therefore experience reduced attenuation and can propagate deeper into dry, low-loss materials such as aeolian sand. In addition, the longer wavelength of P-band reduces sensitivity to small-scale surface roughness, allowing a larger fraction of the radar energy to penetrate beneath the surface before being scattered.

The European Space Agency's BIOMASS mission is the first spaceborne P-band SAR system, operating at 432-438 MHz. Its potential for paleochannel detection has been identified as a secondary mission objective, as P-band backscatter over hyperarid sand sheets is expected to be strongly influenced by subsurface scattering (Paillou et al., 2011). Owing to its reduced sensitivity to small-scale surface roughness and greater penetration depth relative to shorter-wavelength systems, P-band is expected to reveal older and more deeply buried hydrological features that may remain undetected at L-band (Paillou, 2017; Perna et al., 2019). Airborne studies in Tunisia and Morocco have demonstrated that P-band backscatter can be strongly influenced by subsurface scattering and improve detection and mapping of buried alluvial systems (Paillou, 2017; Perna et al., 2019).

A more detailed discussion of electromagnetic propagation and penetration in low-loss media is provided in Appendix A.3.

2.4. Dielectric, moisture, and salinity controls on penetration

Electromagnetic wave propagation in soils is governed by the complex dielectric permittivity,

$$\varepsilon^* = \varepsilon' - j\varepsilon''. \tag{2.4}$$

In this thesis, dielectric properties are expressed as relative permittivity. The real component, ε', controls wave velocity, reflection behaviour, and dielectric contrast, whereas the imaginary component, ε'', governs dielectric losses and therefore directly controls signal attenuation and penetration depth. Since soil moisture increases both components of the complex permittivity, it strongly influences the detectability of buried structures in arid environments (Hallikainen et al., 1985; Topp et al., 1980; Ulaby et al., 1986).

2.4.1. Typical dielectric properties of arid environments

Dry aeolian sand is characterised by a low real relative dielectric permittivity, ε', typically ranging between 2 and 4, and very low dielectric losses, ε'', both of which favour deep radar penetration. Table 2.1 provides representative values of the real part of the relative permittivity, ε', for arid environments relevant to this thesis.

Table 2.1: Representative relative dielectric constants of dry sand in arid environments reported in literature.

Region	Sand type / context	Dielectric constant
Kufrah Basin, Libya	Uniform sand sheets	3.08 (Liu et al., 2021)
Namib Desert, Namibia	Silicate sand in linear dunes	2.80 (Paillou et al., 2020)
Bir Safsaf, Egypt	Modern surface sand sheet	2.85 (Paillou et al., 2003)
Bir Safsaf, Egypt	Compacted underlying sand layers	2.95 (Paillou et al., 2003)
El-Gallaba Plain, Egypt	Windblown dry surface sand	3.04 (Gaber et al., 2011)
Grand Erg Oriental, Tunisia	Fine-grained, hematite-rich dry sand	2.6 (Mätzler, 1998)

Although dry sands exhibit relatively stable dielectric properties, even small amounts of moisture can substantially increase permittivity and dielectric losses, thereby reducing radar penetration depth and enhancing dielectric contrasts between subsurface layers (Paillou et al., 2001; Shahidi et al., 1975).

However, moisture is not the only source of dielectric contrast, as differences in lithology and mineral composition can also create detectable contrasts between surface sands and underlying materials in arid environments. In several desert environments, bedrock typically exhibits significantly higher dielectric constants, approximately 4-7, than overlying sands. This produces dielectric contrasts of approximately 2-3 in relative permittivity, which are favourable for subsurface radar detection.(Elsherbini & Sarabandi, 2010; Liu et al., 2021). Additional contrast arises from alluvial and calcified deposits. Calcified pebble-gravel layers associated with paleochannel beds show elevated permittivity compared to both small pebble alluvium and surface sands, enabling their geophysical delineation (Paillou et al., 2003). Mineralogical variations further modulate dielectric properties, as iron-rich components such as hematite increase dielectric losses and effective permittivity in sandy plains, whereas paleochannel fills composed primarily of quartz tend to retain lower dielectric constants near 2.8 (Zhu et al., 2023).

2.4.2. Role of moisture and salinity

Moisture and salinity are among the primary controls on the dielectric properties of desert soils. Increasing moisture raises both the real and imaginary components of the complex dielectric permittivity, thereby modifying dielectric contrast and electromagnetic attenuation simultaneously. Salinity primarily increases dielectric losses through enhanced ionic conductivity, reducing radar penetration depth (Lasne et al., 2008).

In hyperarid environments such as the Kufrah Basin and the Selima Sand Sheet, volumetric moisture contents commonly remain below 1% (Paillou, 2017). Under these dry conditions, aeolian sands exhibit low dielectric constants and low attenuation, favouring deep radar penetration. However, even modest increases in moisture content can substantially increase permittivity and alter the radar response.

The resulting dielectric contrasts can enhance the detectability of buried subsurface features. For example, wet paleosoils and saturated sediment layers may exhibit dielectric constants substantially higher than the surrounding dry sands, producing strong subsurface reflections (Paillou et al., 2001; Paillou et al., 2003). In evaporitic environments, saline brines can further increase dielectric losses and generate distinctive radar amplitude and phase signatures (Lasne et al., 2008). Consequently, variations in moisture and salinity represent key controls on radar penetration and the detectability of buried paleochannels in arid environments.

2.4.3. Dielectric mixing models

Dielectric mixing models describe the relationship between soil moisture and dielectric permittivity and are widely used in microwave remote sensing (Dobson et al., 1985; Hallikainen et al., 1985; Mironov et al., 2009; Topp et al., 1980). In this thesis, they are used to convert retrieved dielectric constants into dielectric-equivalent moisture estimates. Although these estimates do not represent direct measurements of soil moisture, they provide a physically interpretable framework for relating dielectric anomalies to variations in subsurface material properties.

Several models were considered, ranging from empirical relationships to physically based mixture formulations. The three models used in this study are the Topp model, the Dobson model, and the Complex Refractive Index Model (CRIM).

Topp model

The Topp model (Topp et al., 1980) provides an empirical relationship between volumetric soil moisture content and the real component of dielectric permittivity:

$$\varepsilon'(m_v) = 3.03 + 9.3m_v + 146m_v^2 - 76.7m_v^3. \tag{2.5}$$

where m_v is the volumetric soil moisture content and ε' is the real part of the relative dielectric permittivity. The model was derived from time-domain reflectometry measurements in mineral soils and remains one of the most widely used dielectric relationships in remote sensing applications. Because it does not explicitly account for soil composition, bulk density, or salinity, its applicability may be limited in highly heterogeneous or saline desert environments (Lasne et al., 2008).

Dobson model

The Dobson model (Dobson et al., 1985) represents soil as a mixture of mineral particles, air, and water, while accounting for the effects of soil texture, bulk density, and frequency-dependent dielectric behaviour. The original formulation is semi-empirical and provides a physically based relationship between volumetric moisture content and dielectric permittivity. In this study, a simplified Dobson-based mixing formulation was used,

$$\varepsilon^* = (1-\phi)\varepsilon_s + \phi(1-S_w)\varepsilon_a + \phi S_w \varepsilon_w^*, \tag{2.6}$$

where ϕ is porosity, S_w is water saturation, and ε_s, ε_a, and ε_w^* are the dielectric permittivities of the soil matrix, air, and water, respectively. The volumetric moisture content is related to saturation through

$$m_v = \phi S_w. \tag{2.7}$$

The resulting estimates should therefore be interpreted as Dobson-inspired dielectric-equivalent moisture estimates rather than outputs of the complete Dobson model.

Complex Refractive Index Model (CRIM)

The Complex Refractive Index Model (CRIM) relates the dielectric permittivity of a heterogeneous medium to the volumetric fractions of its constituents through a refractive-index mixing approach (Hallikainen et al., 1985; Ulaby et al., 1986).

For a three-phase soil consisting of solids, air, and water, the effective permittivity can be expressed as

$$\sqrt{\varepsilon_{\text{eff}}} = (1-\phi)\sqrt{\varepsilon_s} + (\phi - m_v)\sqrt{\varepsilon_a} + m_v\sqrt{\varepsilon_w}, \tag{2.8}$$

where ϕ is the porosity, m_v the volumetric moisture content, and ε_s, ε_a, and ε_w are the dielectric permittivities of the soil matrix, air, and water, respectively. The effective dielectric permittivity is then obtained as

$$\varepsilon_{\text{eff}} = \left[(1-\phi)\sqrt{\varepsilon_s} + (\phi - m_v)\sqrt{\varepsilon_a} + m_v\sqrt{\varepsilon_w}\right]^2. \tag{2.9}$$

Because the model is based on refractive-index mixing, it provides a physically intuitive representation of the dielectric behaviour of soil-water-air mixtures and is widely used for relating dielectric permittivity to volumetric moisture content in remote-sensing applications.

2.5. Scattering mechanisms relevant to paleochannel detection

In arid environments, the identification of paleochannels using SAR relies on the interaction between microwave signals and the subsurface. This interaction is characterised by several scattering mechanisms, including surface scattering, volume scattering, and more complex interactions such as odd- and double-bounce scattering.

2.5.1. Surface scattering

Surface scattering is important for distinguishing surficial sand cover from buried geological structures. In hyperarid environments, smooth aeolian sands typically produce weak backscatter due to specular reflection, whereas rough buried bedrock or coarse calcified pebble-gravel deposits generate stronger returns (Paillou, 2017; Paillou et al., 2003). Pure surface scattering is characterised by a high HH-VV correlation, approaching unity (Paillou et al., 2003). Consequently, contrasts between buried rough surfaces and surrounding sediments may produce linear backscatter patterns associated with paleochannels (Paillou, 2017; Paillou et al., 2020).

2.5.2. Volume scattering

Volume scattering occurs when radar waves interact with distributed scatterers such as gravel, cobbles, or heterogeneous channel-fill sediments. Coarse alluvial deposits can enhance volume scattering and produce bright radar signatures, whereas fine-grained alluvium generally yields weaker returns (Paillou, 2017; Ul Islam et al., 2016). Volume scattering is the primary contributor to cross-polarized backscatter (HV/VH), and elevated HV/HH ratios therefore indicate increased subsurface heterogeneity (Paillou et al., 2003). As volume scattering increases, HH-VV correlation decreases, providing a useful discriminator between homogeneous sand sheets and complex alluvial fills (Gaber et al., 2015; Paillou et al., 2003).

2.5.3. Odd- and double-bounce scattering

Odd- and double-bounce scattering mechanisms are commonly analysed using polarimetric decomposition. Significant HH-VV phase differences may arise from saline surfaces, subsurface interfaces, or anisotropic media such as stratified sands and paleosoils (Freeman & Farr, 2007; Lasne et al., 2008; Paillou et al., 2001). These processes generate differential propagation and reflection behaviour between H- and V-polarized waves, producing phase shifts that can indicate subsurface structure. Because long-wavelength systems penetrate more deeply into dry sediments, subsurface and volume-scattering contributions are expected to be more significant at P-band than at shorter wavelengths (Paillou, 2017).

The combined influence of these scattering mechanisms determines the appearance of paleochannels in SAR imagery. Fine-grained or moisture-rich channel fills often appear as dark linear features (“radar rivers”), whereas coarse gravels, buried bedrock, or strong dielectric contrasts may produce bright anomalies (Paillou, 2017; Paillou et al., 2003; Ul Islam et al., 2016). Consequently, amplitude signatures alone are rarely diagnostic and should be interpreted together with polarimetric, phase, coherence, and geomorphological information.

2.5.4. Polarimetric decomposition

Polarimetric decomposition techniques separate observed backscatter into physically interpretable scattering components, typically including surface, volume, and double-bounce scattering. Common model-based approaches include the Freeman-Durden and Yamaguchi decompositions, while eigen-based methods such as the Pauli and Cloude-Pottier decompositions derive parameters describing dominant scattering behaviour and randomness (Cloude & Pottier, 1997; Freeman & Durden, 1998; Lee & Pottier, 2009; Yamaguchi et al., 2005). These products can aid the interpretation of dielectric heterogeneity, alluvial deposits, and buried paleochannel structures in arid environments.

2.6. HH-VV phase difference

The copolarized HH-VV phase difference (CPD) has been identified as a valuable observable for subsurface investigations in arid environments. Experimental studies at the Pyla Dune coastal dune system in southwestern France demonstrated that HH-VV phase signatures could trace buried paleosoils, which act as proxies for moist paleochannels, down to depths of approximately 6.5 m, whereas HH and HV amplitude signatures disappeared beyond approximately 4 m (Grandjean et al., 2001; Paillou et al., 2003). These observations suggest that phase information may remain sensitive to buried subsurface structures even when amplitude-based indicators become weak or ambiguous.

The physical origin of CPD lies in the different propagation and reflection behaviour of horizontally and vertically polarized waves. Paleochannels often contain higher concentrations of moisture or salts

than the surrounding dry aeolian sand, creating dielectric gradients between the channel fill and surrounding sediments (Lasne et al., 2008). Because H and V polarizations respond differently to these gradients, the reflected signals may acquire different phase shifts, producing a measurable HH-VV phase difference (Grandjean et al., 2001; Lasne et al., 2008). Additional phase differences may arise from anisotropic subsurface conditions, such as stratified sand layers or oxidation patterns associated with former water flow, which cause horizontally and vertically polarized waves to propagate at different velocities (Grandjean et al., 2001).

Salinity can further modify phase behaviour. Experimental and modelling studies have shown that while HH and VV backscatter amplitudes are largely insensitive to salinity under completely dry conditions, even small amounts of moisture activate the ionic properties of dissolved salts and can produce measurable changes in the copolarized phase difference (Lasne et al., 2008).

Nevertheless, elevated HH-VV phase differences are not unique indicators of paleochannels. Similar signatures may arise from saline surfaces, evaporitic crusts, anisotropic dune stratification, or other dielectric discontinuities unrelated to buried drainage systems (Freeman & Farr, 2007; Lasne et al., 2008). CPD anomalies should therefore be interpreted together with amplitude, coherence, and geomorphological context.

Overall, CPD provides a subsurface-sensitive observable that complements conventional SAR amplitude measurements by responding to dielectric contrasts, moisture variations, salinity effects, and subsurface stratigraphy within buried drainage systems (Grandjean et al., 2001; Lasne et al., 2008).

2.7. Effective penetration depth inversion

One of the primary objectives of subsurface SAR studies is to infer the depth at which significant radar interactions occur beneath the surface. Unlike directly observable quantities such as backscatter intensity, penetration depth cannot be measured from SAR observations alone. Instead, it must be inferred from observables that are sensitive to the vertical distribution of scatterers and propagation effects within the subsurface. Among these observables, coherence has emerged as one of the most widely used indicators of depth-dependent scattering behaviour.

Whereas amplitude primarily reflects scattering strength and phase records propagation and reflection behaviour, coherence is sensitive to the spatial distribution of scattering contributions within the medium. Because P-band signals can penetrate multiple metres into dry desert sediments, coherence measurements may retain sensitivity to scattering contributions originating from deeper subsurface layers than is typically possible at shorter wavelengths. Consequently, coherence-based approaches provide a physically motivated framework for investigating subsurface structure and estimating effective penetration depth in hyperarid environments.

2.7.1. Coherence as a proxy for subsurface structure

Coherence quantifies the similarity between two complex SAR signals in both amplitude and phase. Depending on the observation configuration, coherence can be evaluated between different polarimetric channels, between repeated acquisitions, or between interferometric image pairs (Bamler & Hartl, 1998; Cloude & Papathanassiou, 1998; Rosen et al., 2000).

In low-loss environments such as hyperarid deserts, interferometric coherence derived from repeated acquisitions can provide indirect information on subsurface structure because radar signals may interact with multiple scattering layers beneath the surface. Variations in dielectric properties, scattering depth, surface roughness, and volumetric heterogeneity can alter the phase and amplitude relationships between coherent returns, leading to measurable changes in coherence (Elsherbini & Sarabandi, 2010; Liu et al., 2021; Xiong et al., 2017). As the vertical distribution of scatterers increases, scattering contributions arrive with different propagation paths and phases. The resulting phase dispersion reduces the measured coherence, providing an indirect indication of distributed subsurface scattering.

Reduced coherence may therefore indicate increased scattering complexity, volume contributions, or changes in the effective location of the dominant scattering phase centre. The phase centre represents the effective location from which the dominant coherent radar signal appears to originate. Changes in the vertical distribution of scatterers can shift the phase centre and modify the observed coherence re-

sponse. Conversely, high coherence generally indicates stable and spatially homogeneous scattering processes. While coherence alone cannot uniquely determine penetration depth, it provides a physically meaningful observable that is sensitive to the vertical distribution of scatterers within the medium.

For this reason, coherence has been widely employed in studies of vegetation structure, snow and ice stratigraphy, and subsurface radar investigations, where it is often interpreted as an indirect indicator of depth-dependent scattering behaviour (Cloude & Papathanassiou, 1998; Liu et al., 2021; Papathanassiou & Cloude, 2001). In arid environments, this sensitivity makes coherence a particularly useful observable for investigating subsurface structure and estimating effective radar penetration depth.

The sensitivity of coherence to vertical variations within the scattering medium is governed by the vertical wavenumber, which determines how strongly changes in scattering depth influence the observed interferometric response.

2.7.2. Vertical wavenumber and sensitivity to depth

The sensitivity of an interferometric radar system to vertical structure is governed by its vertical wavenumber, which quantifies the rate at which interferometric phase changes with height or depth (Bamler & Hartl, 1998; Rosen et al., 2000). Although BIOMASS Stack products are derived from multiple acquisitions, depth retrieval in this thesis is performed on individual interferometric image pairs. For a single interferometric pair, the vertical wavenumber can be expressed as

$$k_z = \frac{4\pi B_\perp}{\lambda R \sin\theta}, \tag{2.10}$$

where $B_\perp$ is the perpendicular baseline, λ is the radar wavelength, R is the slant range, and θ is the incidence angle. This expression provides a simplified conceptual description of interferometric sensitivity and forms the basis for the pairwise depth-retrieval framework adopted in this thesis. The vertical wavenumber is therefore controlled by radar wavelength, acquisition geometry, incidence angle, and the perpendicular baseline between observations. Larger vertical wavenumbers correspond to greater sensitivity to vertical variations, whereas smaller values reduce the ability of the system to distinguish scattering contributions originating from different depths.

In subsurface applications, the vertical wavenumber is particularly important because it determines how strongly distributed scattering within the medium affects the observed interferometric response. Changes in dielectric permittivity influence wave propagation, refraction, and phase velocity, thereby modifying the effective vertical sensitivity of the radar signal within the medium (Bamler & Hartl, 1998; Paillou et al., 2006; Rosen et al., 2000).

As a result, vertical wavenumber provides a key link between acquisition geometry, coherence behaviour, and the sensitivity of radar observations to subsurface structure.

2.7.3. Physical interpretation of effective penetration depth

The concept of effective penetration depth requires careful interpretation in SAR applications. Rather than representing a directly observed quantity, effective penetration depth is generally inferred from observables such as backscatter intensity, phase behaviour, coherence, and polarimetric scattering characteristics (Lasne et al., 2008; Paillou, 2017).

The effective penetration depth is commonly defined as the characteristic distance over which the radar wave attenuates within a medium. It depends primarily on dielectric losses, moisture content, salinity, frequency, and the structural properties of the subsurface (Heggy et al., 2001; Lasne et al., 2008). Under hyperarid conditions, penetration depths may reach several metres, whereas moist or conductive materials can reduce penetration to only a few centimetres.

Various approaches have been proposed for relating radar observables to penetration depth. These broadly fall into two categories:

1. Propagation-based approaches, which use phase delays, attenuation, or dielectric modelling to estimate the depth of subsurface interactions (Liu et al., 2021; Paillou et al., 2006);

2. Coherence-based approaches, which relate changes in coherence or interferometric response to the vertical distribution of scattering contributions within the medium (Cloude & Papathanassiou, 2003; Kellndorfer et al., 2010; Papathanassiou & Cloude, 2001).

These approaches do not necessarily retrieve a discrete geological boundary. Instead, they typically provide information on the vertical extent of the coherence-contributing scattering volume. In this thesis, this quantity is referred to as the effective coherence-derived depth. Consequently, penetration-depth retrieval should generally be interpreted as an estimate of where coherent radar interactions occur within the subsurface rather than as a direct measurement of geological layer depth.

3

Methods

3.1. Study areas

This thesis investigates two arid regions containing previously mapped paleochannel systems: the Kufrah Basin in the eastern Sahara and the Paleo-Kuiseb system in the Namib Desert (Section 2.2.1). These study areas were selected because they represent two of the best-documented paleochannel systems identified using low-frequency SAR observations and provide contrasting settings for paleochannel preservation in arid environments. The Kufrah Basin contains regionally extensive paleodrainage systems preserved beneath relatively continuous sand sheets, whereas the Paleo-Kuiseb system is hosted within an active dune-field environment characterised by strong geomorphological heterogeneity, interdune valleys, and ongoing aeolian reworking (Paillou et al., 2012, 2020). Together, these sites provide an opportunity to evaluate the robustness of BIOMASS-based paleochannel detection and retrieval across distinct modes of paleochannel preservation and varying surface and subsurface conditions. The availability of previously mapped paleochannels further enables comparison with existing geomorphological interpretations.

Both study areas are covered by ascending and descending BIOMASS acquisitions, enabling the same paleochannel systems to be observed from different viewing geometries. This provides an opportunity to evaluate the influence of acquisition geometry and channel orientation on the observed radar response. Because no direct subsurface validation data, such as Ground Penetrating Radar (GPR) profiles, are available for the analysed BIOMASS acquisitions, validation is based on comparison with previously mapped paleochannels and on consistency between radar-derived observables, geomorphological context, and published drainage interpretations.

3.2. BIOMASS data products

ESA BIOMASS Level-1C Stack (STA) products were used as the primary dataset. Each Level-1C Stack product consists of seven repeat-pass SAR acquisitions acquired over the same area. These acquisitions are co-registered, geometrically aligned, and phase calibrated onto a common spatial grid, allowing direct pixel-by-pixel comparison (Aresys], 2025; Piantanida & Boniardi, 2025).

The seven acquisitions within each stack were acquired over a period of approximately two weeks during the BIOMASS commissioning phase. The availability of multiple acquisitions enables the formation of numerous interferometric pairs with different perpendicular baselines and temporal separations. While only two acquisitions are required to form a single interferometric pair, the seven-acquisition stack provides a range of possible acquisition combinations.

The analysed Level-1C stacks originate from multiple BIOMASS sub-swaths (S1-S3), tracks, and frames and were acquired over a period spanning January to July 2026 during the BIOMASS commissioning phase. An overview of the datasets used in this study is provided in Table 3.1. The dataset includes both ascending and descending acquisitions.

Table 3.1: BIOMASS Level-1C STA datasets used in this study.

Study area	Orbit direction	Tracks	Frames
Kufrah Basin	Ascending, Descending	T018, T040	F008-020, F130-146
Paleo-Kuiseb	Ascending, Descending	T003, T040	F287-291, F175-177

In ascending acquisitions, the satellite travels from south to north, whereas in descending acquisitions it travels from north to south. Consequently, the study areas were observed under multiple viewing geometries. The Level-1C products are derived from Level-1A Single-Look Complex (SLC) observations and provide fully polarimetric measurements in the HH, HV, VH, and VV channels. Additional metadata, including acquisition dates, incidence angle, orbit geometry, and baseline information, are also provided and were used in the subsequent retrieval workflow (Aresys], 2025; Piantanida, 2025; Piantanida & Boniardi, 2025). The BIOMASS Level-1C Stack products analysed in this study are publicly available through the ESA Multi-Mission Algorithm and Analysis Platform (MAAP) catalogue (https://explorer.maap.eo.esa.int/?q=BiomassLevel1c), enabling full reproducibility of the data selection and processing workflow. The processing scripts developed for this thesis are openly available at https://github.com/femke2001/MSc-Thesis.git.

3.3. Amplitude and phase analysis

The Level-1C products provide co-registered complex SAR measurements for each polarization channel. From these data, amplitude images and copolarized phase differences were derived and analysed to identify spatially coherent patterns potentially associated with buried paleochannels.

Amplitude products were generated for each polarization channel and compared both individually and through the HH-VV amplitude difference. The copolarized phase difference ($HH - VV$) was derived from the complex radar measurements and restricted to the range $[-\pi, \pi]$ following standard polarimetric conventions (Cloude & Papathanassiou, 1998; Lee & Pottier, 2009). Low-amplitude pixels affected by noise or decorrelation were excluded using a signal-based mask.

To quantify phase variations across candidate paleochannel features, rectangular regions of interest (ROIs) were defined over the interpreted channel and adjacent background areas. Mean phase values were calculated for both regions using circular statistics to account for the wrapped nature of the phase observations. In addition, cross-channel phase profiles were generated by computing the circular mean phase for each range pixel over the full azimuth extent of the ROI. This spatial averaging reduces speckle-related fluctuations while preserving broad phase trends across the channel and surrounding terrain.

The resulting profiles were used to compare phase behaviour within the paleochannel and adjacent background areas. To support interpretation of scattering mechanisms, polarimetric decomposition products were generated using the ESA BIOMASS quick-look processing utilities (`bioqlk.py` and `PolSARpro` (European Space Agency (ESA), 2025) and). Pauli RGB images were used for qualitative visualization of dominant scattering behaviour, while Cloude-Pottier parameters, including entropy (H), anisotropy (A), and alpha angle (α), were used to investigate spatial variations in scattering mechanisms.

The resulting amplitude, phase, and decomposition products were examined for spatially coherent anomalies and compared across multiple scenes and candidate paleochannel locations. These observables provide complementary information on scattering behaviour and were used to guide the interpretation of potential subsurface structures prior to coherence-based depth retrieval.

3.3.1. Difference between L-band and P-band

To provide additional context for the observed BIOMASS P-band signatures, a qualitative comparison was performed with ALOS PALSAR L-band imagery and high-resolution optical imagery from Google Earth. Such a comparison is relevant because radar penetration depth generally increases with wavelength. While L-band (approximately 23 cm wavelength) is capable of limited penetration into dry sandy soils, P-band (approximately 69 cm wavelength) can penetrate substantially deeper in arid environments owing to its longer wavelength and reduced attenuation within dry sediments (Le Toan et al.,

2011). Consequently, P-band observations may reveal subsurface features that are only weakly visible, or entirely absent, in L-band imagery.

3.4. Effective penetration depth estimation

The amplitude, phase, coherence, and polarimetric decomposition products described in the preceding sections are based on established SAR processing techniques and existing BIOMASS processing utilities. The methodological developments introduced in this thesis begin with the effective-depth retrieval workflow, which combines dielectric–roughness inversion, coherence analysis, and acquisition geometry to derive an effective penetration depth estimate from BIOMASS P-band observations.

3.4.1. Methodological overview

To assess whether observed backscatter and phase anomalies may originate from subsurface scattering, a semi-physical effective penetration depth inversion was implemented. The objective is not to retrieve an exact physical boundary, but rather to estimate an effective depth scale over which coherent P-band scattering may contribute to the measured response. This provides a first-order indication of the subsurface volume within which paleochannel-related sediments could plausibly influence the radar signal. The workflow combines co-polarized radar backscatter, interferometric coherence magnitude, and acquisition geometry to estimate the real dielectric constant ε', the dimensionless roughness parameter ks, the corresponding volumetric moisture content m_v, and an effective penetration depth parameter d_{eff}. Candidate Level-1C scene pairs are first screened using spatially averaged VV interferometric coherence. Coherence is estimated from the VV channel and subsequently smoothed using a moving-window average to reduce speckle-related fluctuations and provide a more robust measure of scene-wide coherence. The VV channel was selected because it consistently exhibited higher and more spatially stable coherence than the HH channel across the analysed BIOMASS acquisitions.

Different baseline-selection strategies were adopted for the local and regional analyses. For the detailed single-scene retrievals, the median smoothed coherence was computed for each candidate interferometric pair, and the pair exhibiting the highest median coherence was selected. This approach minimises the influence of decorrelation noise and maximises retrieval stability. For the regional full-swath inversions, the interferometric pair with the largest available perpendicular baseline was selected from each stack. This choice increases sensitivity to vertical scattering structure while providing more consistent effective penetration depth estimates at regional scale, as demonstrated in the baseline-sensitivity analysis presented in Section 5.3.3.

The selected interferometric pair is then analysed using two complementary lookup-table inversion strategies. The first employs a reduced-parameter co-polarized forward model, while the second uses an I2EM-generated rough-surface lookup table. Both approaches retrieve dielectric constant and effective surface roughness, after which the dielectric estimates are converted to volumetric moisture content and combined with interferometric coherence to derive effective penetration depth. During the development of this methodology several other models were considered. Due to time constraints or lack of P-Band validation data, these could not be implemented. An overview of these methods as well as the simplifications and further research directions is given in Appendix D.

The complete processing chain, from interferometric-pair selection and dielectric-roughness inversion to moisture estimation and effective depth retrieval, is summarised in the workflow shown in Figure 3.1.

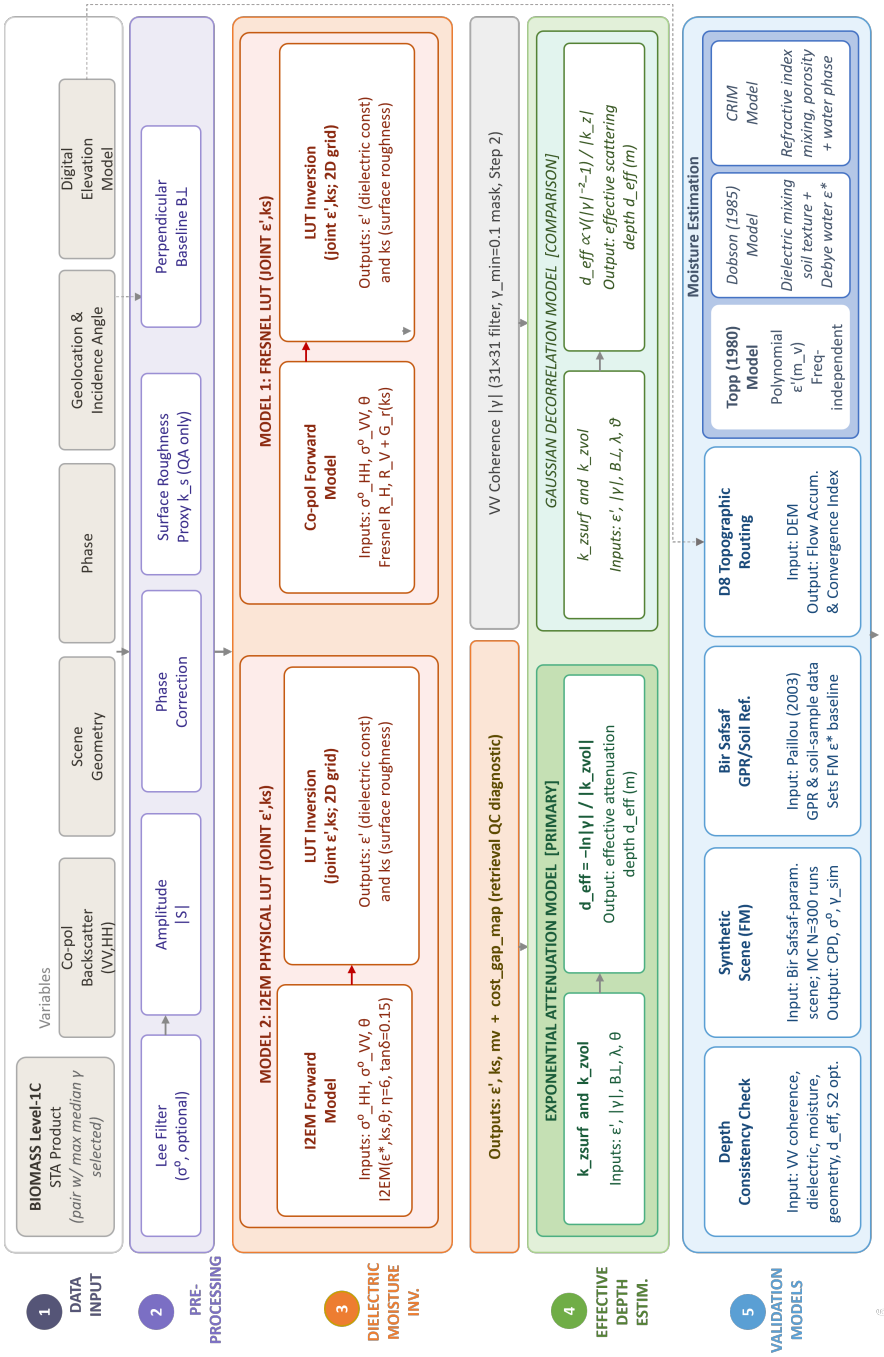

Figure 3.1: Flowchart Depth Inversion

3.4.2. Input data and pre-processing

Candidate Level-1C acquisition pairs were evaluated using the median smoothed VV coherence. For the local retrieval experiments, the pair exhibiting the highest median coherence was selected in order to minimise temporal and geometric decorrelation and maximise retrieval stability. Complex SAR data were reconstructed for all four polarimetric channels, with VV used for coherence estimation and HH and VV jointly used for dielectric-roughness inversion. The VV channel was selected for coherence analysis because it consistently exhibited higher and more spatially stable coherence across the analysed BIOMASS acquisitions.

The Level-1C STA products provide co-registered master and secondary acquisitions on a common grid, and identical raster dimensions were verified for all processed pairs. Prior to inversion, coherence, backscatter, and incidence-angle products were multilooked using a 12×2 pixel window in range and azimuth, respectively, to reduce speckle and improve statistical stability while preserving pixel-wise alignment between all retrieval inputs. A sensitivity analysis of the co-polarization ratio ($VV - HH$) with respect to multilooking window size is presented in Appendix B.2.

After multilooking, all products were resampled onto a common inversion grid. These operations ensured pixel-wise alignment between coherence, radiometric, geometric, and retrieval products prior to LUT inversion.

3.4.3. Interferometric coherence estimation

The coherence magnitude is defined as

$$\gamma_{\mathrm{mag}}(\mathbf{x}) = |\gamma(\mathbf{x})|, \qquad 0 \leq \gamma_{\mathrm{mag}} \leq 1. \tag{3.1}$$

Coherence was computed using the implementation provided in the ESA BIOMASS quick-look processing tools (`bioqlk.py`; (European Space Agency (ESA), 2025)), which estimate coherence through local spatial averaging of complex-valued SAR measurements. In this study, coherence was calculated from the VV channel of the master and secondary acquisitions:

$$\gamma_{VV}(\mathbf{x}) = \frac{\left\langle \widetilde{S}_{VV}^{(1)}(\mathbf{x}) \widetilde{S}_{VV}^{(2)\,*}(\mathbf{x}) \right\rangle}{\sqrt{\left\langle |\widetilde{S}_{VV}^{(1)}(\mathbf{x})|^2 \right\rangle \left\langle |\widetilde{S}_{VV}^{(2)}(\mathbf{x})|^2 \right\rangle}}, \tag{3.2}$$

with the coherence magnitude given by

$$\gamma_{\mathrm{mag}}(\mathbf{x}) = |\gamma_{VV}(\mathbf{x})|. \tag{3.3}$$

To reduce speckle-related fluctuations, the coherence magnitude was spatially averaged using a 5×5 moving window and subsequently multilooked to the inversion grid together with the radiometric products. This reduces estimator variance and improves coherence stability at the expense of spatial resolution. The resulting coherence field was used both for interferometric pair selection and for the effective penetration-depth retrieval.

3.4.4. Geometric and radiometric ancillary variables

Incidence angle and radiometric backscatter were extracted from the master BIOMASS Stack product. The local incidence angle θ was obtained from the geometric metadata and converted into a raster matching the SAR image grid. The co-polarized normalised radar cross section, σ^0, was used as input for the dielectric inversion.

Because SAR backscatter may be stored either in logarithmic units (dB) or linear power units, a unit-consistency check was performed prior to the inversion. When the backscatter was provided in dB, it was converted to linear power according to

$$\sigma^0_{\mathrm{lin}}(\mathbf{x}) = 10^{\sigma^0_{\mathrm{dB}}(\mathbf{x})/10}. \tag{3.4}$$

If the input backscatter was already stored in linear units, no additional conversion was applied. All subsequent calculations were performed using linear backscatter values.

To reduce speckle while retaining spatial heterogeneity, an 5×5 Lee filter was implemented. The optimal window size was evaluated in Appendix B.5. For each pixel $\mathbf{x}$, local image statistics were computed within a moving window $\mathcal{W}_{\mathbf{x}}$ centred on that pixel. The local mean and variance are

$$\mu(\mathbf{x}) = \frac{1}{N} \sum_{i \in \mathcal{W}_{\mathbf{x}}} I_i, \qquad v_I(\mathbf{x}) = \frac{1}{N} \sum_{i \in \mathcal{W}_{\mathbf{x}}} I_i^2 - \mu^2(\mathbf{x}), \tag{3.5}$$

where I is the linear-intensity image and $\mathcal{W}_{\mathbf{x}}$ denotes the moving window. The filtered intensity is then computed as

$$I_{\mathrm{Lee}}(\mathbf{x}) = \mu(\mathbf{x}) + W(\mathbf{x})\left[I(\mathbf{x}) - \mu(\mathbf{x})\right], \tag{3.6}$$

where the adaptive Lee weight is defined as

$$W(\mathbf{x}) = \frac{v_I(\mathbf{x})}{v_I(\mathbf{x}) + v_n}, \tag{3.7}$$

and v_n is a scene-level noise-variance proxy estimated from the median of the local variances. The dependence of $W(\mathbf{x})$ on the moving window is therefore implicit through the locally estimated mean and variance. Regions with high local variance receive larger weights and preserve more spatial detail, whereas homogeneous regions are smoothed more strongly.

3.4.5. Radar wavelength and roughness parameter

All retrievals used the BIOMASS centre frequency of 435 MHz, corresponding to a wavelength of $\lambda = 0.689$ m.

Surface roughness was represented by the wavelength-normalised roughness parameter

$$k_s = \frac{2\pi s}{\lambda}, \tag{3.8}$$

where s is the RMS surface height (Fung et al., 1992).

Throughout this thesis, k_s denotes the dimensionless wavelength-normalised roughness parameter. Although it is expressed in terms of the radar wavenumber and RMS surface height, k_s is treated as a single roughness parameter and not as the product of two independently retrieved variables.

3.4.6. LUT Inversion

Two inversion approaches were implemented. The first uses a simplified co-polarized forward model with a joint HH-VV LUT inversion. The second uses a lookup table generated from the Improved Integral Equation Model (I2EM). Both approaches retrieve dielectric constant and effective surface roughness from the co-polarized BIOMASS observations. Lookup-table approaches are widely used in microwave remote sensing because they provide a computationally efficient framework for solving nonlinear electromagnetic inversion problems while maintaining physical interpretability (Fung et al., 1992; Ulaby & Long, 2014; Ulaby et al., 1986).

Table 3.2: Nominal parameter ranges used in the joint HH-VV and I2EM-LUT inversions.

Parameter	Nominal range/value	Interpretation
ε'	2.5-12	Dry to weakly moist sandy/alluvial sediments
k_s	0.046-0.456	Equivalent to RMS height of 5-50 mm at P-band
θ	$22°$-$35°$	BIOMASS incidence-angle range
m_v	0-0.35	Moisture lookup range for dielectric-model interpretation
$\tan\delta$	0.15	I2EM dielectric loss-tangent assumption
L/s	6	I2EM correlation-length/RMS-height ratio
$\gamma_{\min}$	0.1	Minimum coherence for depth retrieval

Model 1: Joint HH-VV Dielectric-Roughness LUT Inversion

The nominal dielectric retrieval was implemented as a two-parameter lookup-table inversion using the co-polarized HH and VV backscatter channels. A reduced-parameter forward model was adopted in which the dielectric dependence is represented through the Fresnel reflection coefficients (Ulaby & Long, 2014; Ulaby et al., 1986)

$$R_H(\varepsilon', \theta) = \frac{\cos\theta - \sqrt{\varepsilon' - \sin^2\theta}}{\cos\theta + \sqrt{\varepsilon' - \sin^2\theta}}, \tag{3.9}$$

$$R_V(\varepsilon', \theta) = \frac{\varepsilon'\cos\theta - \sqrt{\varepsilon' - \sin^2\theta}}{\varepsilon'\cos\theta + \sqrt{\varepsilon' - \sin^2\theta}}, \tag{3.10}$$

where ε' is the real relative permittivity and θ is the local incidence angle.

The use of both co-polarized channels provides complementary sensitivity to dielectric and roughness effects, reducing ambiguity in the retrieval. Surface roughness is represented using the empirical roughness-activation function,

$$G_r(k_s) = 1 - \exp[-\beta(k_s)^a], \tag{3.11}$$

where k_s is the wavelength-normalised roughness parameter defined in Equation 3.8, and β and a are dimensionless calibration constants. The formulation was motivated by the observations of Campbell and Shepard (1996), who showed that radar backscatter increases approximately exponentially with wavelength-scaled surface roughness before approaching a saturation level. Inspired by this behaviour, an empirical roughness-activation function was introduced in this study to provide a simple, monotonic representation of the roughness contribution to backscatter. Unlike the relationships proposed by Campbell and Shepard (1996), the present formulation is not derived from field measurements and does not constitute a physical scattering model. Instead, it serves as a computationally efficient approximation whose parameters were calibrated against I2EM simulations. For the adopted parameterization, $\beta = 2.72$ and $a = 1.0$. The resulting function reproduces the general increase of radar response with wavelength-normalised roughness predicted by rough-surface scattering models such as IEM and I2EM (Fung et al., 1992; Hsieh et al., 1997). The value of β was obtained by fitting the roughness response of the simplified model to the normalised I2EM roughness dependence (Appendix B.4).

The resulting co-polarized forward model is

$$\widehat{\sigma}^0_{pp} = g_{pp}|R_{pp}|^2 G_r(k_s)\cos^{p_\theta}\theta, \tag{3.12}$$

where $pp \in \{HH, VV\}$, g_{pp} is a scene-level calibration factor, and p_θ is an empirical exponent controlling the incidence-angle dependence of the model. In the nominal implementation, $p_\theta = 1$ was adopted. The squared Fresnel coefficient represents the first-order dependence of backscatter power on dielectric contrast, while $G_r(k_s)$ accounts for the influence of wavelength-normalised surface roughness. The incidence-angle term provides a simplified approximation of the angular variation in backscatter and should not be interpreted as a rigorous physical scattering model.

The model is not intended to reproduce the full electromagnetic behaviour of rough-surface scattering. Instead, it provides a computationally efficient approximation of the first-order dependence of co-polarized backscatter on dielectric contrast, roughness, and incidence angle, suitable for generation of the reduced-parameter lookup table (Fung et al., 1992; Ulaby & Long, 2014; Ulaby et al., 1986).

Because the simplified forward model does not predict absolute backscatter levels directly, separate gain factors were estimated for the HH and VV channels. A reference prediction was computed using a dry-soil dielectric constant $\varepsilon'_{\mathrm{ref}} = 3.0$,

$$\widehat{\sigma}^{0,\mathrm{ref}}_{pp}(\mathbf{x}) = |R_{pp}(\varepsilon'_{\mathrm{ref}}, \theta(\mathbf{x}))|^2 G_r(k_s(\mathbf{x}))\cos^{p_\theta}\theta(\mathbf{x}), \tag{3.13}$$

and the gain factor was estimated as

$$g_{pp} = \mathrm{median}\left(\frac{\sigma^0_{pp,\mathrm{obs}}}{\widehat{\sigma}^{0,\mathrm{ref}}_{pp}}\right). \tag{3.14}$$

The inversion was performed on an 80×80 lookup table spanning

$$\varepsilon' \in [2.5, 12.0], \qquad k_s \in [0.046, 0.456]. \tag{3.15}$$

These ranges correspond to dry to weakly moist sandy sediments and RMS surface heights of approximately 5 mm to 5 cm at the BIOMASS P-band wavelength (Dobson et al., 1985; Ulaby & Long, 2014; Ulaby et al., 1986).

For each candidate pair $(\varepsilon'_i, k_{s,j})$, predicted HH and VV backscatter values were computed and compared with the observations in logarithmic space. The cost function was defined as

$$\begin{aligned} J(\varepsilon'_i, k_{s,j}; \mathbf{x}) = w_{HH} \left[\log_{10} \sigma^0_{HH,\mathrm{obs}}(\mathbf{x}) - \log_{10} \widehat{\sigma}^0_{HH,ij}(\mathbf{x})\right]^2 \\ + w_{VV} \left[\log_{10} \sigma^0_{VV,\mathrm{obs}}(\mathbf{x}) - \log_{10} \widehat{\sigma}^0_{VV,ij}(\mathbf{x})\right]^2 . \end{aligned} \tag{3.16}$$

The retrieved parameter pair was obtained as

$$(\varepsilon'_{\mathrm{est}}(\mathbf{x}), k_{s,\mathrm{est}}(\mathbf{x})) = \arg \min_{\varepsilon'_i, k_{s,j}} J(\varepsilon'_i, k_{s,j}; \mathbf{x}). \tag{3.17}$$

The use of both HH and VV channels provides a more constrained retrieval than a single-channel inversion, although the dielectric-roughness trade-off remains an inherent limitation because both properties influence co-polarized backscatter amplitudes (Baghdadi et al., 2006; Fung et al., 1992; Oh et al., 1992). Consequently, the retrieved k_s values should be interpreted as effective roughness parameters rather than direct measurements of RMS surface height.

Model 2: I2EM-based dielectric-roughness LUT inversion

As a physically based sensitivity test, the reduced-parameter co-polarized forward model was replaced by a lookup table generated using the Improved Integral Equation Model (I2EM). The I2EM model belongs to the IEM family of rough-surface scattering models and extends the original Integral Equation Model through improved treatment of roughness effects over a wider range of surface conditions (Fung et al., 1992; Hsieh et al., 1997).

The I2EM LUT was generated over the same parameter space used in the nominal retrieval,

$$\varepsilon' \in [2.5, 12.0], \qquad k_s \in [0.046, 0.456], \qquad \theta \in [22^\circ, 35^\circ]. \tag{3.18}$$

For each roughness value, RMS height was obtained from

$$s = \frac{k_s \, \lambda}{2\pi}, \tag{3.19}$$

where λ is the BIOMASS P-band wavelength. Because independent measurements of surface correlation length were unavailable, the correlation length was parameterised as

$$L = \eta s, \qquad \eta = 6, \tag{3.20}$$

where η is the correlation-length-to-RMS-height ratio. The derivation, justification, and sensitivity analysis of this assumption are provided in Appendix B.3. This parameterization preserves a two-parameter retrieval comparable to the nominal inversion, but implies that the retrieved roughness should be interpreted as an effective roughness under a fixed correlation-length assumption.

The complex dielectric permittivity was represented as

$$\varepsilon^* = \varepsilon' - j\varepsilon'', \qquad \varepsilon'' = \tan\delta \, \varepsilon', \tag{3.21}$$

where a fixed loss tangent of $\tan\delta = 0.15$ was adopted in the nominal LUT.

For the dielectric range considered in this thesis, the low-loss approximation ($\varepsilon'' \ll \varepsilon'$) is assumed, such that the real part of the permittivity primarily controls scattering behaviour, while the imaginary part mainly affects attenuation (Ulaby et al., 1986). The I2EM implementation nonetheless requires specification of the full complex permittivity, and therefore a representative loss tangent was prescribed to account for finite dielectric losses.

The I2EM LUT provides predicted co-polarized backscatter values

$$\left[\widehat{\sigma}^0_{HH}, \widehat{\sigma}^0_{VV}\right] = \mathcal{F}_{\mathrm{I2EM}}\left(\varepsilon', k_s, \theta; \eta, \tan\delta\right), \tag{3.22}$$

where $\mathcal{F}_{\mathrm{I2EM}}$ denotes the Improved Integral Equation Model forward operator (Fung et al., 1992; Hsieh et al., 1997). In contrast to the reduced-parameter forward model, I2EM explicitly accounts for the interaction between dielectric properties, roughness geometry, incidence angle, and polarization through an electromagnetic rough-surface scattering formulation.

The lookup table was generated using an open-source Python implementation of I2EM developed by Mallett (2024), which follows the IEM/I2EM formulations described by Fung et al. (1992) and Hsieh et al. (1997). For each combination of $(\varepsilon', k_s, \theta)$, the I2EM model was evaluated to compute the corresponding co-polarized backscatter coefficients σ^0_{HH} and σ^0_{VV}. The resulting backscatter values were stored in a three-dimensional lookup table covering the complete retrieval parameter space.

During inversion, observed BIOMASS backscatter values were compared with the pre-computed LUT entries using the same joint HH-VV cost function as the nominal retrieval. The parameter combination producing the minimum cost was retained as the retrieved dielectric constant and effective roughness parameter.

The IEM family of models has been extensively applied for the simulation and retrieval of soil dielectric properties and surface roughness from SAR observations because it explicitly represents the dependence of radar backscatter on dielectric contrast, RMS height, correlation length, incidence angle, and polarization (Baghdadi et al., 2006; K.-S. Chen et al., 2000; Choker et al., 2017; Fung et al., 1992). The I2EM LUT therefore provides a more physically based rough-surface scattering representation than the reduced-parameter forward model, although uncertainty associated with the assumed correlation-length parameterization remains an important limitation.

Cross-polarized HV backscatter was not included in the final LUT. Although I2EM is capable of simulating cross-polarized scattering, computation of the HV channel is substantially more expensive than the co-polarized channels. Furthermore, the conditioning analysis indicated that inclusion of HV produced only limited improvement in resolving the dielectric-roughness ambiguity relative to the additional computational cost. Consequently, the final I2EM inversion was performed using only the co-polarized HH and VV backscatter channels.

Conversion from dielectric constant to volumetric moisture

After the joint HH-VV inversion, the retrieved dielectric constant $\varepsilon'_{\mathrm{est}}$ is converted to volumetric moisture content m_v using selected dielectric mixing relationships (Dobson et al., 1985; Hallikainen et al., 1985; Topp et al., 1980). This step is a post-inversion interpretation rather than an independent radar inversion. For each dielectric model, a one-dimensional lookup table is constructed:

$$m_{v,k} \in [0, 0.35], \tag{3.23}$$

and

$$\varepsilon'_k = f_{\mathrm{dielectric}}(m_{v,k}). \tag{3.24}$$

The volumetric moisture estimate is then obtained by nearest matching:

$$m_{v,\mathrm{est}}(\mathbf{x}) = \arg\min_{m_{v,k}} \left|\varepsilon'_{\mathrm{est}}(\mathbf{x}) - f_{\mathrm{dielectric}}(m_{v,k})\right|. \tag{3.25}$$

This conversion was applied using the Topp, Dobson, and CRIM dielectric relationships. The primary purpose of this step was to translate retrieved dielectric properties into a more intuitive and physically

interpretable variable that can be related to variations in subsurface moisture conditions. Moisture content is widely used in hydrological and remote-sensing studies and provides a common framework for comparing dielectric anomalies with independent environmental observations. The resulting moisture maps should be interpreted as effective dielectric-equivalent moisture estimates rather than direct in-situ soil-moisture measurements. This distinction is important because salinity, mineralogy, porosity, compaction, and buried sediment type may also influence the dielectric response in arid environments.

Retrieval quality control and non-uniqueness diagnostics
To identify poorly constrained pixels, the inversion retains both the best-fitting and second-best-fitting LUT solutions. A cost-gap diagnostic is defined as

$$\Delta J(\mathbf{x}) = J_2(\mathbf{x}) - J_1(\mathbf{x}), \tag{3.26}$$

where J_1 and J_2 are the lowest and second-lowest LUT costs, respectively. Low values of ΔJ indicate that multiple (ε', k_s) combinations provide similarly good fits and that the retrieval is therefore poorly determined. Maps of ΔJ were retained and analysed alongside the retrieved dielectric and depth products to identify regions where the inversion was poorly constrained.

Pixels were also flagged when the retrieved solution reached the lower or upper limits of the LUT domain, when the residual cost was anomalously large, or when they occurred within edge regions affected by resampling or missing-data artefacts. These diagnostics were used to interpret the retrieval maps and to distinguish robust spatial patterns from areas of high inversion ambiguity.

3.4.7. Baseline, slant range, and vertical wavenumber

The effective-depth retrieval framework requires estimates of the perpendicular baseline $B_\perp$ and the corresponding vertical wavenumber. The perpendicular baseline is defined as the component of the separation vector between two SAR acquisitions that is perpendicular to the radar line-of-sight. In interferometric SAR, $B_\perp$ controls the sensitivity of the acquisition geometry to vertical structure and therefore directly influences the depth sensitivity of the retrieval. Depending on the processing workflow, $B_\perp$ was obtained either from orbit-state-vector geometry or from the baseline metadata supplied with the BIOMASS product.

The provenance of the adopted baseline is stated for each retrieval experiment. When derived from orbit information, the baseline geometry was evaluated at the scene centre using the master and secondary satellite state vectors. Figure 3.2 illustrates the geometric quantities used in the calculation. The baseline vector $\mathbf{B}$ connects the two acquisition positions, while the line-of-sight vector $\boldsymbol{\ell}$ extends from the master satellite position to the scene-centre target. The perpendicular baseline $B_\perp$ is the component of $\mathbf{B}$ perpendicular to the radar line-of-sight., and the slant range R is given by the distance between the master satellite and the scene centre. A detailed derivation of the scene-centre baseline geometry is provided in Appendix B.1 .

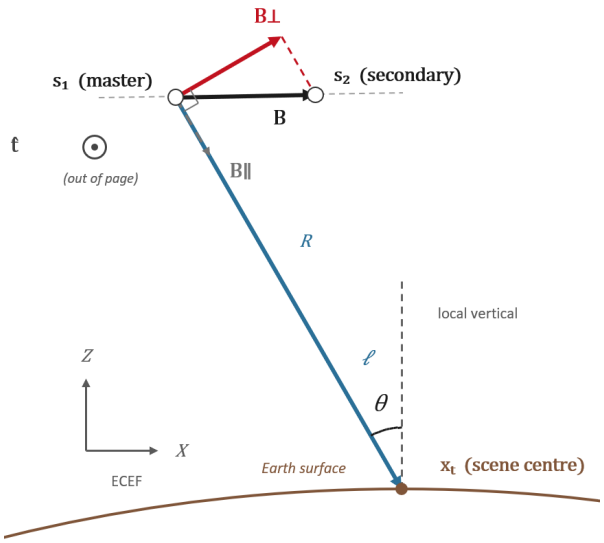

Figure 3.2: Geometry used for scene-centre estimation of the perpendicular baseline and slant range. The line-of-sight vector $\boldsymbol{\ell}$ extends from the master satellite position $\mathbf{s}_1$ to the scene-centre target $\mathbf{x}_t$. The baseline vector $\mathbf{B}$ connects the master and secondary acquisition positions, and its component perpendicular to the line-of-sight defines the perpendicular baseline $B_\perp$. The slant range is given by $R = \|\boldsymbol{\ell}\|$.

The surface vertical wavenumber was then calculated for each pixel using

$$k_{z,\mathrm{surf}}(\mathbf{x}) = \frac{4\pi}{\lambda} \frac{|B_\perp|}{R \sin\theta(\mathbf{x})}, \tag{3.27}$$

where λ is the radar wavelength and θ is the local incidence angle. The vertical wavenumber describes the sensitivity of the interferometric acquisition geometry to vertical structure and therefore controls the depth sensitivity of the coherence-based retrieval. To approximately account for wave propagation within a dielectric medium, a dielectric-corrected vertical wavenumber was calculated as

$$k_{z,\mathrm{vol}}(\mathbf{x}) = k_{z,\mathrm{surf}}(\mathbf{x}) \frac{\varepsilon'_{\mathrm{est}}(\mathbf{x}) \cos\theta(\mathbf{x})}{\sqrt{\varepsilon'_{\mathrm{est}}(\mathbf{x}) - \sin^2\theta(\mathbf{x})}}, \tag{3.28}$$

where $\varepsilon'_{\mathrm{est}}$ is the retrieved real relative permittivity. Under the low-loss approximation ($\varepsilon'' \ll \varepsilon'$), this correction accounts for refractive effects and the reduced propagation velocity of the wave within the subsurface medium. Both $k_{z,\mathrm{surf}}$ and $k_{z,\mathrm{vol}}$ were evaluated. The final effective-depth retrieval used $k_{z,\mathrm{vol}}$, thereby approximately accounting for dielectric refraction within the retrieved medium.

3.4.8. Effective depth from coherence magnitude

The final step converts interferometric coherence magnitude into a coherence-derived depth scale. For numerical stability, coherence values were clipped to the interval $[10^{-6}, 0.999999]$.

The primary retrieval adopts an exponential attenuation model in which coherence decreases exponentially with increasing penetration depth. Assuming uniform volumetric decorrelation, coherence can be expressed as

$$|\gamma| = \exp(-|k_{z,\mathrm{vol}}|\, d_{\mathrm{eff}})\,, \tag{3.29}$$

where d_{eff} represents the effective vertical extent contributing to the interferometric phase signal. Solving Equation 3.29 for depth yields

$$d_{\mathrm{eff}}(\mathbf{x}) = -\frac{\ln|\gamma(\mathbf{x})|}{|k_{z,\mathrm{vol}}(\mathbf{x})|}, \tag{3.30}$$

where $|\gamma|$ is the coherence magnitude and $k_{z,\mathrm{vol}}$ is the dielectric-corrected vertical wavenumber defined in Equation 3.28.

This formulation represents a simplified effective-depth interpretation of volume-decorrelation theory, in which a reduction in interferometric coherence is associated with an increasing vertical extent of the scattering volume (Cloude & Papathanassiou, 2003; Papathanassiou & Cloude, 2001; Treuhaft et al., 1996).

The retrieved quantity d_{eff} should be interpreted as a coherence-derived depth scale rather than the depth to a discrete geological interface. Larger values indicate coherent scattering over a greater vertical extent, whereas smaller values reflect stronger attenuation or greater vertical heterogeneity. Consequently, d_{eff} represents an indicator of penetration potential rather than a direct estimate of paleochannel burial depth.

In the implemented workflow, the volume-corrected vertical wavenumber was used for all reported depth estimates as it accounts approximately for wave propagation and refraction within the retrieved dielectric medium.

As a reference case, a Gaussian decorrelation model was also evaluated. This formulation assumes that decorrelation originates from a vertically distributed scattering volume and is expressed as

$$d_{\mathrm{eff,Gauss}} = \frac{\sqrt{|\gamma|^{-2} - 1}}{|k_{z,\mathrm{vol}}|}. \tag{3.31}$$

The Gaussian model is commonly used in volume-scattering applications such as vegetation and distributed media (Cloude & Papathanassiou, 2003; Treuhaft & Siqueira, 2000). In contrast, the exponential formulation was adopted as the nominal retrieval because it provides a more conservative depth estimate and is more consistent with an attenuation-based interpretation of coherence loss in arid subsurface environments.

Accordingly, the retrieved quantity d_{eff} should be interpreted as a coherence-derived depth scale or effective attenuation depth rather than a sharply defined physical boundary. It represents the characteristic depth over which coherent subsurface scattering contributes to the measured interferometric signal and therefore provides an indirect indication of the vertical extent of potentially detectable paleochannel structures.

3.4.9. Regional-scale depth inversion

To evaluate the retrieval framework at regional scale, the depth inversion was applied to all available BIOMASS Level-1C Stack products covering the Kufrah Basin and Namib Desert study areas. Each stack contains seven co-registered acquisitions, allowing multiple interferometric pairs to be formed. Perpendicular baselines were extracted from the Level-1C metadata and used to characterise the interferometric geometry of each pair. For the regional-scale retrievals, the interferometric pair with the largest available perpendicular baseline was selected. The rationale for this choice is evaluated in the baseline-sensitivity analysis presented in Section 5.3.3.

3.5. Forward model and validation framework

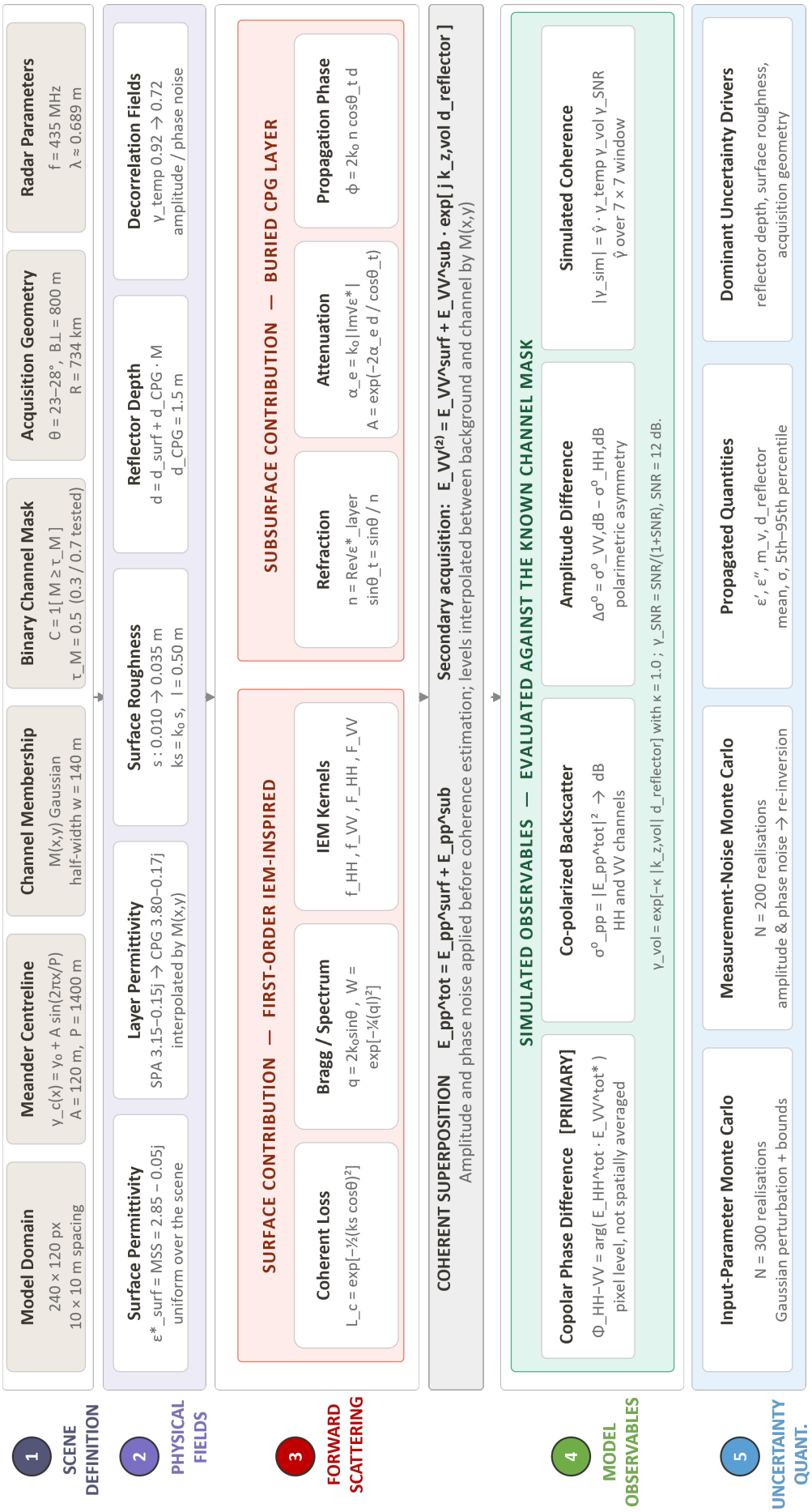

Figure 3.3: Workflow of the synthetic forward-model and validation framework.

3.5.1. Model objective and role in the methodology

The effective-depth retrieval described in Section 3.4.8 estimates subsurface structure from interferometric coherence and radar backscatter observations. However, the inversion is inherently non-unique, as similar observable signatures can arise from different combinations of dielectric contrast, surface roughness, temporal decorrelation, signal-to-noise ratio, and reflector depth. To better understand the behaviour of the retrieval, a physically guided forward model was developed. The model provides a controlled environment in which the sensitivity of the observables to individual physical parameters can be isolated and systematically evaluated. Although the baseline configuration is derived from the Bir Safsaf paleochannel system, the framework is intended as a generic representation of buried paleochannel detection and is therefore applicable to other arid environments, including the Kufrah Basin and Paleo-Kuiseb study areas. The forward model can be adapted through modification of the dielectric, geometric, and environmental input parameters while retaining the same underlying retrieval framework. The overall validation workflow is summarised in Figure 3.3.

The forward model simulates the coherent radar response of an idealised buried paleochannel system under prescribed physical conditions. Because the channel geometry and dielectric structure are fully known, the model acts as a virtual laboratory in which synthetic observables can be directly related to their physical causes. Detection performance can therefore be evaluated without ambiguity in ground truth. The objective is not to reproduce the full electromagnetic complexity of natural desert environments, but to identify the physical conditions under which phase-, backscatter-, and coherence-based paleochannel detection is expected to succeed, fail, or become ambiguous. The results are subsequently used to support the interpretation of real BIOMASS observations.

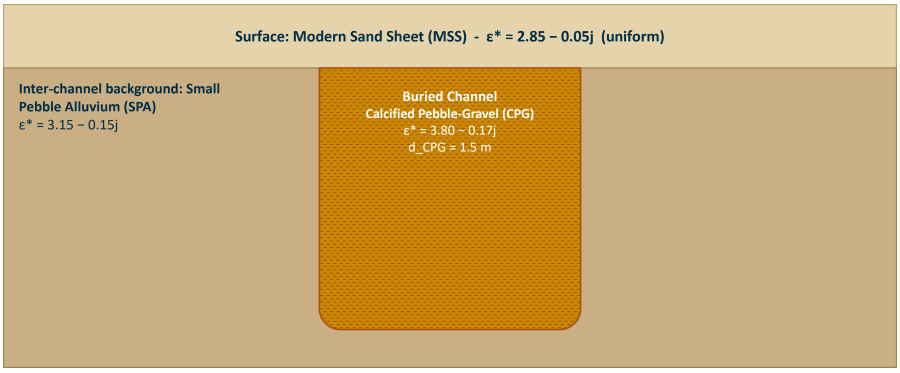

Figure 3.4: Conceptual geometry of the synthetic Bir Safsaf validation model. A buried calcified pebble-gravel paleochannel (CPG) is embedded within a small-pebble alluvium (SPA) background and covered by a uniform modern sand sheet (MSS). Complex dielectric permittivities assigned to each material are indicated. The channel burial depth d_{CPG} is 1.5 m. This simplified geometry was used to evaluate the sensitivity of the forward model to dielectric contrasts and subsurface channel structure.

The baseline configuration is grounded in the Bir Safsaf site in south-central Egypt, where low-frequency SAR and GPR observations have been used to characterise buried paleodrainage structures (Grandjean et al., 2001; Paillou et al., 2003). The dielectric properties and representative stratigraphic layer depths used in the forward model are anchored to the soil-sample measurements and subsurface interpretation reported by Paillou et al. (2003). This site is therefore used as a physically grounded reference case for testing the expected BIOMASS response over a confirmed Saharan paleochannel environment.

3.5.2. Baseline configuration and model assumptions

The forward model requires a representative set of environmental and acquisition parameters from which the sensitivity of the radar observables can be investigated. Rather than representing a specific BIOMASS acquisition, the baseline configuration defines a synthetic paleochannel embedded within a dry aeolian-sand environment, with dielectric and stratigraphic properties chosen to be broadly consistent with the Bir Safsaf paleochannel system.

In the baseline configuration, the near-surface is represented by a modern sand sheet (MSS) with a

constant complex permittivity of $\varepsilon^*_{\mathrm{MSS}} = 2.85 - 0.05j$. The buried paleochannel target is represented by a calcified pebble-gravel (CPG) layer with $\varepsilon^*_{\mathrm{CPG}} = 3.80 - 0.17j$, while the surrounding inter-channel subsurface is assigned the small pebble alluvium (SPA) value of $\varepsilon^*_{\mathrm{SPA}} = 3.15 - 0.15j$ (Paillou et al., 2003). The baseline simulation uses these measured Bir Safsaf dielectric constants directly rather than deriving them from a moisture-permittivity model. Moisture-based dielectric models such as Topp, CRIM, and Dobson are retained as alternative configurations for sensitivity experiments and Monte Carlo analysis, but are not used in the baseline scene. The buried CPG reflector is placed at a nominal depth of 1.5 m, corresponding to the midpoint of the stratigraphic range reported by Paillou et al. (2003).

The model is intentionally simplified and is intended to capture the first-order controls on the radar response rather than provide a rigorous electromagnetic simulation of subsurface scattering. Several assumptions are therefore adopted. First, the scene is represented using a 2.5D geometry in which each image pixel contains a local vertical scattering structure, while lateral electromagnetic interactions between neighbouring pixels are neglected. Second, the baseline configuration represents the subsurface response using a single dominant buried CPG layer, although alternative multilayer and bedrock configurations are available within the modelling framework. Third, surface scattering is described using a first-order IEM-inspired approximation that preserves the main relationships between dielectric properties, surface roughness, and co-polarized response without requiring a full numerical electromagnetic solution. Fourth, the simulated coherence field is used to evaluate the internal behaviour of the depth-retrieval framework under controlled conditions and is not interpreted as an independent validation of the physical coherence-depth relationship. Fifth, in the baseline Bir Safsaf configuration, dielectric properties are prescribed from published soil-sample measurements rather than derived from a moisture-permittivity model.

The principal parameters defining the baseline simulation are summarised in Table 3.3. These values should be interpreted as representative reference conditions rather than fixed environmental constants. A visual representation of the synthetic scene is displayed in Figure 3.5.

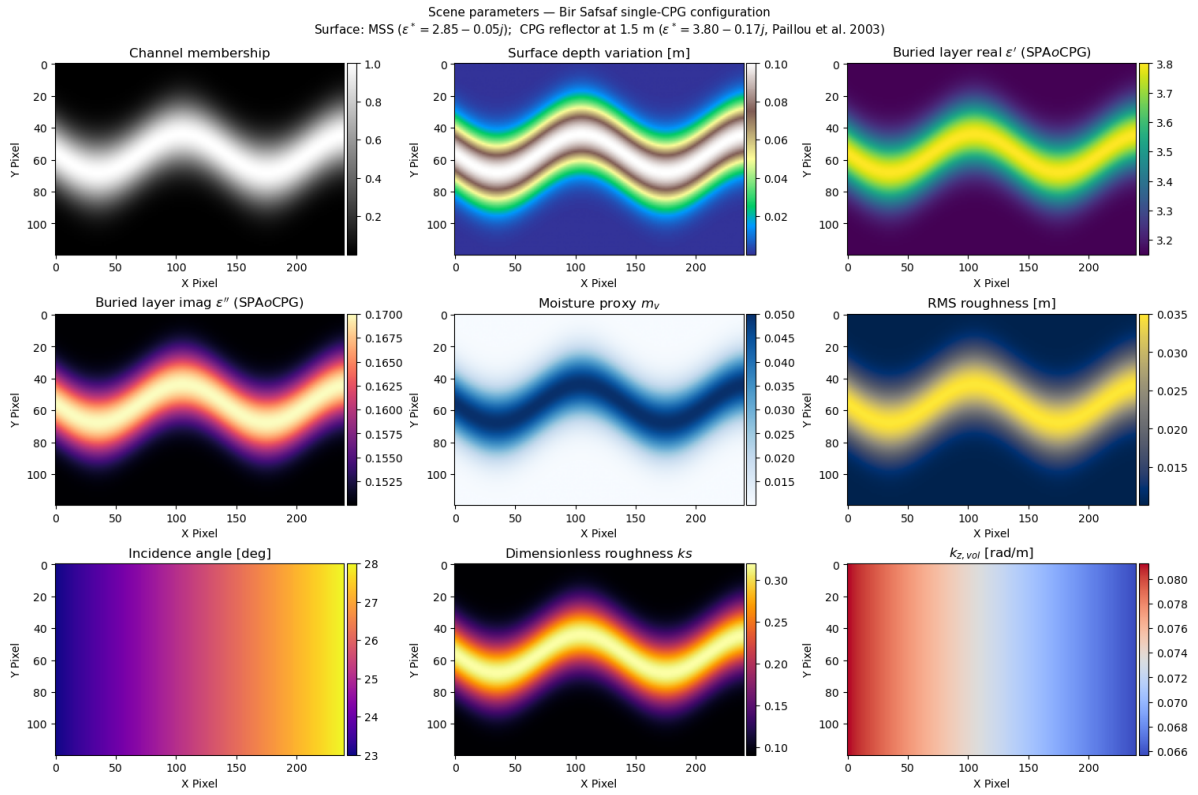

Figure 3.5: Synthetic paleochannel model used for validation. Shown are the prescribed channel membership, surface-depth variation, buried-layer dielectric properties, moisture content, roughness, incidence angle, dimensionless roughness (k_s), and vertical wavenumber ($k_{z,\mathrm{vol}}$).

Table 3.3: Nominal parameter values used in the baseline Bir Safsaf forward-model simulation.

Parameter	Value	Interpretation
Scene size	240×120 pixels	Synthetic spatial domain
Radar frequency	435 MHz	BIOMASS P-band centre frequency
Incidence angle range	$23°$-$28°$	BIOMASS-like observation geometry
Perpendicular baseline	800 m	Interferometric baseline
Slant range	734 km	Nominal BIOMASS-like slant range
Channel half-width	140 m	Characteristic channel width
Channel sinuosity amplitude	120 m	Meander amplitude
Channel sinuosity wavelength	1400 m	Meander wavelength
Buried layer depth	1.5 m	Depth of buried reflector
Channel depth amplitude	0.10 m	Near-surface corrugation component
Surface permittivity MSS	$\varepsilon^* = 2.85 - 0.05j$	Modern sand-sheet value (Paillou et al., 2003)
Background layer permittivity SPA	$\varepsilon^* = 3.15 - 0.15j$	Inter-channel buried layer (Paillou et al., 2003)
Channel layer permittivity CPG	$\varepsilon^* = 3.80 - 0.17j$	Channel-associated buried layer (Paillou et al., 2003)
Background RMS roughness	0.010 m	Smooth sand-sheet surface
Channel RMS roughness	0.035 m	Rougher channel-associated surface
Layer amplitude	0.28	Relative subsurface scattering strength
Temporal coherence background	0.92	Background coherence level
Temporal coherence channel	0.72	Channel coherence level
Signal-to-noise ratio	12 dB	Synthetic measurement quality

3.5.3. Scene representation and physical parameterisation

The model domain is represented on a two-dimensional spatial grid (x, y). Each pixel contains a locally one-dimensional vertical scattering structure, while lateral wave propagation and pixel-to-pixel coupling are neglected. This 2.5D approximation substantially reduces computational requirements while retaining the spatial variability needed to evaluate detection performance across channel boundaries.

The synthetic paleochannel is represented by a smooth meandering centreline. The centreline position varies sinusoidally along the scene:

$$y_c(x) = y_0 + A_{\sin} \sin\left(\frac{2\pi x}{P}\right), \tag{3.32}$$

where y_0 is the mean cross-scene channel position, $A_{\sin}$ is the meander amplitude, and P is the meander wavelength. The spatial membership of each pixel within the channel is then described using a Gaussian function:

$$M(x, y) = \exp\left[-\frac{1}{2}\left(\frac{y - y_c(x)}{w}\right)^2\right], \tag{3.33}$$

where w is the channel-width parameter. This formulation produces a smooth cross-channel transition rather than an abrupt binary boundary, which is more consistent with gradational sedimentary transitions and allows detection performance to be evaluated as a function of distance from the channel centreline. Since $M(x, y)$ approaches but does not exactly reach zero, a binary validation mask is obtained by thresholding the membership function:

$$\mathcal{C}(x, y) = \mathbf{1}\left[M(x, y) \geq \tau_M\right], \tag{3.34}$$

where τ_M is the prescribed membership threshold. For validation purposes, the default threshold is $\tau_M = 0.5$.

Spatially varying physical parameters are assigned by interpolating between background and channel values using the membership function. For a generic parameter p,

$$p(x, y) = p_{\mathrm{bg}} + M(x, y)\left(p_{\mathrm{ch}} - p_{\mathrm{bg}}\right), \tag{3.35}$$

where p_{bg} and p_{ch} denote the prescribed background and channel values, respectively. The same interpolation framework is used to define buried-layer permittivity, surface roughness, temporal coherence, and other spatially varying parameters within the synthetic scene.

In the Bir Safsaf baseline configuration, two spatially distinct dielectric fields are defined. The surface permittivity $\varepsilon'_{\mathrm{surf}}(x, y)$ is held uniform at the MSS value,

$$\varepsilon'_{\mathrm{surf}}(x, y) = \varepsilon^*_{\mathrm{MSS}} = 2.85 - 0.05j, \tag{3.36}$$

because the same fine-sand sheet is assumed to cover both channel and inter-channel areas at the surface. The buried-layer permittivity $\varepsilon^*_{\mathrm{layer}}(x, y)$ is interpolated between the background SPA value and the channel-associated CPG value:

$$\varepsilon^*_{\mathrm{layer}}(x, y) = \varepsilon^*_{\mathrm{SPA}} + M(x, y)\,(\varepsilon^*_{\mathrm{CPG}} - \varepsilon^*_{\mathrm{SPA}})\,, \tag{3.37}$$

with $\varepsilon^*_{\mathrm{SPA}} = 3.15 - 0.15j$ and $\varepsilon^*_{\mathrm{CPG}} = 3.80 - 0.17j$ (Paillou et al., 2003). This distinction is important because the surface scattering term is controlled by the MSS cover, while the subsurface scattering term is controlled by the buried paleochannel layer.

Surface roughness is represented through the dimensionless roughness parameter k_s, where $k_0 = 2\pi/\lambda$ is the free-space wavenumber and s is the RMS surface height:

$$k_s(x, y) = k_0 s(x, y). \tag{3.38}$$

The RMS roughness field $s(x, y)$ is interpolated between the smooth background sand value and the rougher channel-associated value using Equation 3.35.

A distinction is made between the shallow surface-depth perturbation and the physical reflector depth used in the subsurface and coherence calculations. The reflector depth is defined as

$$d_{\mathrm{reflector}}(x, y) = d_{\mathrm{surface}}(x, y) + d_{\mathrm{CPG}}\, M(x, y), \tag{3.39}$$

where $d_{\mathrm{CPG}} = 1.5$ m is the nominal burial depth of the CPG layer. This quantity corresponds to the depth variable used in the interferometric phase and coherence simulations.

3.5.4. Surface scattering contribution

The surface contribution is modelled using a first-order IEM-inspired complex field expression. For each co-polarized channel $pp \in \{HH, VV\}$, the surface field is written as

$$E^{\mathrm{surf}}_{pp}(x, y) = R_{pp} L_c(k_s, \theta) + \left(f_{pp} + \frac{F_{pp}}{8\pi^2}\right)(k_s)^2 W(q, l), \tag{3.40}$$

where R_{pp} is the Fresnel reflection coefficient evaluated using the surface permittivity $\varepsilon'_{\mathrm{surf}}$, L_c is the coherent-loss factor, f_{pp} and F_{pp} are the first-order IEM kernels, and $W(q, l)$ is the Gaussian roughness spectrum evaluated at the Bragg wavenumber. The coherent-loss factor is

$$L_c(k_s, \theta) = \exp\left[-\frac{1}{2}\left(k_s \cos\theta\right)^2\right], \tag{3.41}$$

which accounts for the reduction of the coherent specular component due to surface roughness (Fung et al., 1992). The Bragg wavenumber is

$$q = 2k_0 \sin\theta, \tag{3.42}$$

and the Gaussian roughness spectrum is

$$W(q,l) = \exp\left[-\frac{1}{4}(ql)^2\right], \tag{3.43}$$

where l is the surface correlation length.

The first-order IEM kernels used for the two co-polarized channels are

$$f_{HH} = -2R_{HH}\cos\theta, \tag{3.44}$$
$$f_{VV} = 2R_{VV}\cos\theta, \tag{3.45}$$

and

$$F_{HH} = -2\sin^2\theta\cos\theta\left[4R_{HH} - \left(1-\varepsilon_{\text{surf}}^{*-1}\right)\left(1+R_{HH}\right)^2\right], \tag{3.46}$$
$$F_{VV} = 2\sin^2\theta\cos\theta\left[\left(1-\varepsilon_{\text{surf}}^{*-1}\cos^2\theta+\sin^2\theta\right)\left(1-R_{VV}\right)^2 + \left(1-\varepsilon_{\text{surf}}^{*-1}\right)\left(1+R_{VV}\right)^2\right]. \tag{3.47}$$

This formulation differs from the empirical roughness activation used in the depth-inversion pipeline. In the forward model, the surface phase is not imposed through a separate phase term. Instead, it is generated implicitly by the complex Fresnel coefficients and the IEM-inspired surface-scattering terms. The HH and VV surface fields can therefore carry different phases even before the subsurface contribution is added.

3.5.5. Subsurface scattering contribution

The subsurface contribution originates from a buried CPG-associated scattering layer located at depth $d_{\text{reflector}}(x,y)$ beneath the surface. The buried response is not modelled using an explicit second dielectric interface beneath the CPG. Instead, the net reflectivity of the buried target is represented through a scalar amplitude parameter, which controls the strength of the subsurface return while avoiding the need to prescribe an additional dielectric layer beneath the reflector.

Under the low-loss approximation ($\varepsilon'' \ll \varepsilon'$), the refractive index is approximated using the real relative permittivity,

$$n(x,y) = \sqrt{\varepsilon'_{\text{layer}}(x,y)}, \tag{3.48}$$

so that

$$\sin\theta_t = \frac{\sin\theta}{n}, \qquad \cos\theta_t = \sqrt{1-\sin^2\theta_t}. \tag{3.49}$$

This approximation separates refraction from attenuation and is appropriate for low-loss media where $\varepsilon'' \ll \varepsilon'$ (Born & Wolf, 1999; Ulaby et al., 1986). For the Bir Safsaf CPG value $\varepsilon^* = 3.80 - 0.17j$, the loss tangent is small, so the imaginary part of the refractive index is treated through attenuation rather than through a complex transmitted angle.

The attenuation coefficient is computed from the imaginary part of the complex refractive index:

$$\alpha_e\left(\varepsilon^*_{\text{layer}}\right) = k_0\left|\text{Im}\left[\sqrt{\varepsilon^*_{\text{layer}}}\right]\right|, \tag{3.50}$$

where $k_0 = 2\pi/\lambda$. The two-way attenuation through a layer of depth $d_{\text{reflector}}$ is then

$$A_{\text{atten}}\left(d_{\text{reflector}}, \varepsilon^*_{\text{layer}}, \theta\right) = \exp\left(\frac{-2\alpha_e d_{\text{reflector}}}{\cos\theta_t}\right). \tag{3.51}$$

The corresponding two-way propagation phase is

$$\phi_{\mathrm{prop}}\left(d_{\mathrm{reflector}}, \varepsilon^{*}_{\mathrm{layer}}, \theta\right) = 2k_0 n \cos\theta_t d_{\mathrm{reflector}}. \tag{3.52}$$

The resulting subsurface field for polarization pp is

$$E^{\mathrm{sub}}_{pp}(x,y) = a_0 M(x,y) A_{\mathrm{atten}}\left(d_{\mathrm{reflector}}, \varepsilon^{*}_{\mathrm{layer}}, \theta\right) \exp\left[j\phi_{\mathrm{prop}}\left(d_{\mathrm{reflector}}, \varepsilon^{*}_{\mathrm{layer}}, \theta\right)\right] T_{pp}\left(\varepsilon'_{\mathrm{surf}}, \theta\right), \tag{3.53}$$

where $a_0 = 0.28$ is the dimensionless subsurface scattering amplitude, $M(x,y)$ spatially confines the subsurface contribution to the paleochannel, and T_{pp} is the Fresnel transmission coefficient at the air-surface interface. The factor $a_0 M(x,y)$ causes the subsurface response to be strongest near the channel centreline and to vanish toward the background, which allows the forward-model output to be evaluated against the known channel mask. Consistent with the low-loss approximation adopted for refraction, the Fresnel reflection and transmission coefficients are evaluated using the real relative permittivity only. The imaginary component is assumed to have a negligible influence on reflection and transmission and is accounted for separately through the attenuation term.

The transmission coefficients are

$$T_H\left(\varepsilon'_{\mathrm{surf}}, \theta\right) = \frac{2\cos\theta}{\cos\theta + \sqrt{\varepsilon'_{\mathrm{surf}} - \sin^2\theta}}, \tag{3.54}$$

$$T_V\left(\varepsilon'_{\mathrm{surf}}, \theta\right) = \frac{2\sqrt{\varepsilon'_{\mathrm{surf}}}\cos\theta}{\varepsilon'_{\mathrm{surf}}\cos\theta + \sqrt{\varepsilon'_{\mathrm{surf}} - \sin^2\theta}}. \tag{3.55}$$

3.5.6. Coherent superposition and copolar phase difference

The total radar return is modelled as the coherent sum of the surface and subsurface contributions. For each polarization channel, the total complex field is

$$E^{\mathrm{tot}}_{pp}(x,y) = E^{\mathrm{surf}}_{pp}(x,y) + E^{\mathrm{sub}}_{pp}(x,y), \tag{3.56}$$

where the surface and subsurface components are given by Equations 3.40 and 3.53, respectively.

The copolar phase difference (CPD) is computed at pixel level from the phase relationship between the HH and VV channels:

$$\Phi_{\mathrm{HH-VV}}(x,y) = \arg\left\{\exp\left[j\left(\arg E^{\mathrm{tot}}_{HH}(x,y) - \arg E^{\mathrm{tot}}_{VV}(x,y)\right)\right]\right\}. \tag{3.57}$$

Equivalently, this can be written as

$$\Phi_{\mathrm{HH-VV}}(x,y) = \arg\left(E^{\mathrm{tot}}_{HH}(x,y)\left[E^{\mathrm{tot}}_{VV}(x,y)\right]^{*}\right). \tag{3.58}$$

The CPD is evaluated at pixel level and is not spatially averaged within the forward-model calculations. Spatial averaging is applied only during coherence estimation.

For a homogeneous surface under small-perturbation assumptions, $\Phi_{\mathrm{HH-VV}}$ is expected to remain close to zero or vary only gradually with dielectric properties and surface roughness (Cloude & Papathanassiou, 1998; Lee & Pottier, 2009). In the forward model, a buried dielectric layer modifies the HH and VV fields through different surface reflection, transmission, and rough-surface scattering terms, while also introducing a depth-dependent propagation phase. Previous low-frequency radar studies have identified such co-polar phase behaviour as a useful indicator of subsurface structure in dry environments (Grandjean et al., 2001; Paillou et al., 2003).

3.5.7. Simulated interferometric coherence

The retrieval framework uses interferometric coherence magnitude $|\gamma|$ as one of its primary observables (Section 3.4.8). In the forward model, coherence is computed from two synthetic complex VV acquisitions rather than being prescribed directly as a standalone depth function.

A secondary acquisition is generated by applying a depth-dependent interferometric phase shift to the subsurface component:

$$E_{VV}^{(2)}(x,y) = E_{VV}^{\mathrm{surf}}(x,y) + E_{VV}^{\mathrm{sub}}(x,y)\exp\left[jk_{z,\mathrm{vol}}(x,y)d_{\mathrm{reflector}}(x,y)\right]. \tag{3.59}$$

Prior to coherence estimation, amplitude and phase noise are applied to the synthetic complex fields. Noise levels vary spatially between background and channel regions using the same membership-based interpolation framework adopted for the physical scene parameters.

The coherence magnitude $\hat{\gamma}(x,y)$ is then estimated from the master-secondary image pair using local spatial averaging over a $W \times W$ pixel window, with $W = 7$ in the baseline configuration:

$$\hat{\gamma}(x,y) = \frac{\left|\left\langle E_{VV}^{(1)}\left[E_{VV}^{(2)}\right]^{*}\right\rangle_{W}\right|}{\sqrt{\left\langle\left|E_{VV}^{(1)}\right|^{2}\right\rangle_{W}\left\langle\left|E_{VV}^{(2)}\right|^{2}\right\rangle_{W}}}. \tag{3.60}$$

This introduces the same type of local estimation behaviour as in the real interferometric coherence calculation.

An analytical coherence envelope is additionally computed as the product of volume, temporal, and signal-to-noise decorrelation terms (Bamler & Hartl, 1998; Zebker & Villasenor, 1992):

$$|\gamma_{\mathrm{model}}|(x,y) = \gamma_{\mathrm{temp}}(x,y)\,\gamma_{\mathrm{vol}}(x,y)\,\gamma_{\mathrm{SNR}}. \tag{3.61}$$

The volume decorrelation term is

$$\gamma_{\mathrm{vol}}(x,y) = \exp\left[-\kappa\,|k_{z,\mathrm{vol}}(x,y)|\,d_{\mathrm{reflector}}(x,y)\right], \tag{3.62}$$

where $\kappa = 1.0$ controls the strength of the exponential depth-dependent decorrelation. The temporal coherence term is interpolated between the background and channel values using the channel membership function:

$$\gamma_{\mathrm{temp}}(x,y) = \gamma_{\mathrm{temp,bg}} + M(x,y)\left(\gamma_{\mathrm{temp,ch}} - \gamma_{\mathrm{temp,bg}}\right), \tag{3.63}$$

with $\gamma_{\mathrm{temp,bg}} = 0.92$ and $\gamma_{\mathrm{temp,ch}} = 0.72$. The SNR decorrelation term is

$$\gamma_{\mathrm{SNR}} = \frac{\mathrm{SNR}}{1+\mathrm{SNR}}, \qquad \mathrm{SNR} = 10^{\mathrm{SNR_{dB}}/10}, \tag{3.64}$$

with $\mathrm{SNR_{dB}} = 12$ dB.

The final simulated coherence is obtained by applying the analytical decorrelation envelope to the locally estimated coherence:

$$|\gamma_{\mathrm{sim}}|(x,y) = \hat{\gamma}(x,y)|\gamma_{\mathrm{model}}|(x,y). \tag{3.65}$$

Here, $d_{\mathrm{reflector}}$ refers to the physical burial depth of the CPG reflector, not to the shallow near-surface topographic corrugation of the synthetic channel. This distinction is important because the coherence-depth relationship is intended to test sensitivity to the buried paleochannel reflector rather than to minor surface relief.

This forward coherence formulation is internally related to the exponential depth-inversion model of Equation 3.30, but it is not a perfectly independent validation of that relationship. In particular, the additional temporal and SNR decorrelation terms reduce the direct sensitivity of $|\gamma_{\mathrm{sim}}|$ to reflector depth. As a result, depth retrieval from the simulated coherence may underestimate the prescribed reflector depth when temporal or noise decorrelation is not explicitly separated.

3.5.8. Model outputs and detection observables

For each synthetic scene, the forward model produces four spatially distributed observables that can be analysed in relation to the known channel mask:

1. **Copolar phase difference** $\Phi_{\mathrm{HH-VV}}(x, y)$ (Equation 3.57), which serves as the primary paleochannel detection observable.
2. **Co-polarized backscatter** $\sigma^0_{HH}(x, y)$ and $\sigma^0_{VV}(x, y)$, computed from the total complex field as

$$\sigma^0_{pp,\mathrm{lin}}(x, y) = \left|E^{\mathrm{tot}}_{pp}(x, y)\right|^2 . \tag{3.66}$$

   The corresponding decibel-scaled backscatter is

$$\sigma^0_{pp,\mathrm{dB}}(x, y) = 10 \log_{10} \left[\sigma^0_{pp,\mathrm{lin}}(x, y)\right] . \tag{3.67}$$

3. **Amplitude difference**

$$\Delta\sigma^0(x, y) = \sigma^0_{VV,\mathrm{dB}}(x, y) - \sigma^0_{HH,\mathrm{dB}}(x, y), \tag{3.68}$$

   which measures the polarimetric amplitude asymmetry between the two co-polarized channels and corresponds to the quantity used in the validation experiments.
4. **Simulated interferometric coherence** $|\gamma_{\mathrm{sim}}|(x, y)$ (Equation 3.65), which is used to evaluate the behaviour of the effective-depth retrieval under controlled conditions.

Together, these observables provide a direct link between the known synthetic channel geometry, the prescribed Bir Safsaf-inspired physical parameters, and the quantities analysed in the real BIOMASS datasets. The forward model therefore supports interpretation by identifying which observable responses are expected from dielectric contrast, roughness, burial depth, and decorrelation under controlled conditions.

3.5.9. Monte Carlo uncertainty quantification

The forward model contains a range of uncertain environmental and acquisition parameters, including moisture content, surface roughness, burial depth, soil texture, acquisition geometry, and signal-to-noise ratio. To evaluate the sensitivity of the model outputs to these uncertainties, a Monte Carlo framework is employed. Two complementary Monte Carlo analyses are implemented. The first propagates uncertainty in the physical scene parameters through the forward model, while the second quantifies uncertainty in the inversion results arising from simulated measurement noise.

Input-parameter uncertainty propagation

The primary Monte Carlo analysis propagates uncertainty in the scene configuration through the forward model. Each uncertain parameter is assigned either a relative or absolute Gaussian perturbation together with physically realistic bounds. For the i-th Monte Carlo realisation,

$$p_k^{(i)} = \mathrm{clip}\left[p_k^{(0)} + \sigma_k\left(p_k^{(0)}\right)\xi_k^{(i)},\, p_k^{\min},\, p_k^{\max}\right], \qquad \xi_k^{(i)} \sim \mathcal{N}(0, 1), \tag{3.69}$$

where $p_k^{(0)}$ is the nominal value of parameter k, σ_k is either a relative uncertainty $\sigma_k = r_k|p_k^{(0)}|$ or an absolute uncertainty $\sigma_k = s_k$, and $[p_k^{\min}, p_k^{\max}]$ defines the physically admissible parameter range.

The uncertainty specification used in the Monte Carlo propagation is summarised in Table 3.4.

Table 3.4: Input-parameter uncertainty specification used in the Monte Carlo uncertainty propagation. Relative uncertainties are defined as fractions of the nominal parameter value, while absolute uncertainties are specified in native units.

Parameter	Symbol	Type	Value	Bounds
Background moisture	$m_{v,\mathrm{bg}}$	relative	$r = 0.30$	$[0, 0.5]$
Channel moisture	$m_{v,\mathrm{ch}}$	relative	$r = 0.30$	$[0, 0.5]$
Background depth offset	d_{bg}	absolute	$s = 0.05$ m	$[0, \infty)$
Channel depth amplitude	d_{ch}	relative	$r = 0.20$	$[0, \infty)$
CPG reflector depth	d_{layer}	relative	$r = 0.25$	$[0.5, 3.0]$ m
Background RMS roughness	s_{bg}	relative	$r = 0.30$	$[0.001, \infty)$ m
Channel RMS roughness	s_{ch}	relative	$r = 0.30$	$[0.001, \infty)$ m
Sand fraction	f_{sand}	absolute	$s = 5.0\%$	$[0, 100]\%$
Clay fraction	f_{clay}	absolute	$s = 3.0\%$	$[0, 100]\%$
Bulk density	ρ_b	absolute	$s = 0.10$ g cm^{-3}	$[0.8, 2.2]$ g cm^{-3}
Temperature	T	absolute	$s = 5°$C	-
Perpendicular baseline	$B_\perp$	relative	$r = 0.10$	-
Slant range	R	relative	$r = 0.01$	-
SNR	$\mathrm{SNR}_{\mathrm{dB}}$	absolute	$s = 2.0$ dB	-

The uncertainty assigned to the CPG reflector depth ($r = 0.25$, bounded between 0.5 and 3.0 m) reflects the variability in the thickness of the overlying sedimentary units reported for the Bir Safsaf paleochannel system (Paillou et al., 2003).

For each perturbed realisation, the complete forward model is re-evaluated. The default analysis uses $N_{\mathrm{MC}} = 300$ realisations. Rather than analysing the variance of the simulated CPD or coherence directly, the Monte Carlo framework stores the resulting distributions of physically interpretable scene properties, namely the surface real permittivity $\varepsilon'(x, y)$, the surface imaginary permittivity $\varepsilon''(x, y)$, volumetric moisture content $m_v(x, y)$, and physical reflector depth $d_{\mathrm{reflector}}(x, y)$.

From these ensembles, the mean, standard deviation, and 5th-95th percentile ranges are computed on a pixel-by-pixel basis. These statistics provide uncertainty bounds on the dielectric and depth quantities that are ultimately used in the retrieval framework.

It should be noted that the measured Bir Safsaf dielectric constants ($\varepsilon^*_{\mathrm{MSS}}$, $\varepsilon^*_{\mathrm{SPA}}$, and $\varepsilon^*_{\mathrm{CPG}}$) are treated as fixed values in the baseline constant-dielectric mode. Consequently, uncertainty in the buried-layer permittivity itself is not propagated. Instead, uncertainty in dielectric properties is introduced through perturbations of moisture content and soil-texture parameters when the Topp, CRIM, or Dobson dielectric models are activated. In the baseline constant-dielectric configuration, the dominant contributors to output uncertainty are therefore reflector depth, surface roughness, and acquisition geometry.

Measurement-noise Monte Carlo analysis

A second Monte Carlo analysis is used to quantify uncertainty arising from simulated SAR measurement noise. In this case, random amplitude and phase perturbations are applied to the synthetic observations before the inversion procedure is repeated.

Two retrieval pathways are considered. The first evaluates the uncertainty in dielectric-property retrievals derived from co-polarized amplitude and phase observations. The second evaluates uncertainty in depth retrievals derived from interferometric coherence. The default number of realisations is $N_{\mathrm{MC}} = 200$ for the dielectric-retrieval analysis, while the coherence-based depth analysis uses a configurable number of noise realisations depending on the experiment.

This measurement-noise Monte Carlo differs conceptually from the input-parameter uncertainty propagation described above. The former quantifies the uncertainty of the retrieved dielectric and depth estimates given noisy observations, whereas the latter quantifies the sensitivity of the underlying scene properties to uncertainty in the physical model inputs.

Together, the two Monte Carlo frameworks provide complementary information on uncertainty. The input-parameter Monte Carlo identifies which environmental and acquisition parameters exert the strongest control on the simulated scene properties, while the measurement-noise Monte Carlo evaluates the robustness of the corresponding retrievals under realistic SAR observation errors.

3.5.10. Geomorphological validation using D8 topographic modelling

A DEM-based D8 flow-routing analysis was performed to provide an independent geomorphological reference for the interpretation of radar-derived paleochannel signatures. After depression filling, flow directions and flow-accumulation fields were computed using the D8 algorithm (Jenson & Domingue, 1988; O'Callaghan & Mark, 1984) described in Appendix E. Stream networks were extracted using multiple accumulation thresholds and compared with the spatial distribution of coherence, CPD, and depth anomalies. The resulting drainage patterns were further evaluated against the HydroRIVERS hydrographic database (Lehner & Grill, 2013) to assess the consistency of the DEM-derived drainage network with an independent regional-scale drainage dataset. The resulting drainage patterns were used only as geomorphological validation layers and were not interpreted as evidence of present-day hydrological activity.

3.5.11. Optical corroboration of SAR-derived paleochannel candidates

To provide independent evidence for paleochannel candidates identified from BIOMASS P-band observations, contemporaneous Sentinel-2 Level-2A imagery was co-registered to each BIOMASS acquisition (Drusch et al., 2012; Le Toan et al., 2011). Although optical data cannot directly detect buried channels, it can reveal surface characteristics associated with paleochannel systems, including variations in moisture retention, mineralogy, soil exposure, and geomorphic texture. The use of long-wavelength radar for detecting buried drainage systems is supported by earlier Shuttle Imaging Radar studies in the eastern Sahara, which demonstrated radar penetration through dry sediments and the mapping of previously unknown paleochannels (McCauley et al., 1982; Schaber et al., 1986).

Sentinel-2 scenes were selected within ± 15 days of each BIOMASS acquisition and filtered to less than 25% cloud cover. RGB, NIR, SWIR1 (Band 11, 1610 nm) and SWIR2 (Band 12, 2190 nm) bands were resampled to the BIOMASS geometry and masked to remove scene edges and invalid pixels.

Five optical indicators were derived:

1. Inverted NDVI, representing low vegetation likelihood (Tucker, 1979);
2. Relative NDWI, computed as the deviation from the scene median to highlight local moisture anomalies (Gao, 1996);
3. A clay-mineral index,
$$\mathrm{CMI} = \frac{\mathrm{SWIR1} + R}{\mathrm{SWIR2} + G}, \tag{3.70}$$
adapted from geological band-ratio approaches for mineral mapping in arid environments (Sultan et al., 1986);
4. Bare Soil Index (BSI) (W. Chen et al., 2004);
5. Optical brightness texture, computed as local reflectance variance.

These optical indicators were combined with SAR-derived coherence anomaly, coherence texture, and HH-VV phase difference. All features were independently normalised to the range $[0, 1]$ using robust 2nd-98th percentile scaling:

$$X_{\mathrm{norm}} = \frac{X - P_2}{P_{98} - P_2}. \tag{3.71}$$

A weighted composite score was then calculated as

$$S = \sum_{i=1}^{N} w_i X_i, \tag{3.72}$$

where X_i is the normalised feature and w_i its assigned weight. The weighting scheme was selected heuristically based on the expected physical relevance of each indicator, with greater emphasis placed on BIOMASS-derived metrics because they provide the primary evidence for subsurface structure.

Table 3.5: Weights assigned to the indicators used in the composite paleochannel score.

Indicator	Weight
Coherence anomaly	0.25
HH-VV phase difference	0.15
Radar texture	0.10
Relative moisture anomaly	0.15
Clay-mineral index	0.15
Bare-soil index	0.05
Low vegetation likelihood	0.05
Low slope likelihood	0.05
Optical texture	0.05
Total	1.00

The composite score was smoothed using a Gaussian filter ($\sigma = 2$ pixels) and thresholded at the 95th percentile. Connected-component analysis and morphological filtering were then applied to retain elongated channel-like features (minimum area 300 pixels, aspect ratio ≥ 1.5, eccentricity ≥ 0.75). Agreement between the SAR-only coherence anomaly and the fused SAR-optical score was used as a qualitative measure of optical support for radar-derived detections.

4

Results

The results chapter first presents the preprocessing and analysis of a representative BIOMASS scene in the Sahara, including amplitude, phase, polarimetric, coherence, inversion, and effective-depth retrieval products. Unless stated otherwise, the BIOMASS Sahara Level-1C Stack scene from Sub-swath 1, Track 040, Frame 176 is used throughout this chapter as a reference example to illustrate the developed workflow and the behaviour of the derived observables. The performance and physical interpretation of the developed workflow are then assessed using multiple validation approaches, including synthetic forward modelling, drainage-network analysis, and comparison with independent Sentinel-2 observations. Subsequently, the retrieval framework is applied to larger-scale datasets in the Kufrah Basin and Namib Desert study areas. These regional analyses are used to evaluate the spatial consistency of the retrieved products, investigate their behaviour across full BIOMASS swaths, and assess the broader applicability of the proposed methodology.

4.1. Preprocessing

To reduce speckle noise and improve the reliability of subsequent analyses, the BIOMASS acquisitions were combined through multi-temporal stacking. Figure 4.1 compares a representative single acquisition with the resulting stacked image. The stacked image exhibits reduced speckle and improved radiometric consistency, resulting in a smoother and more spatially coherent representation of the study area. The benefits of stacking are particularly evident at local scale. Small-scale intensity fluctuations present in the reference image are substantially reduced, allowing linear and channel-like features to appear more continuous and spatially coherent. Boundaries between adjacent surface units are also better defined, improving the distinction between geomorphological features and the surrounding terrain. Importantly, the stacking procedure does not introduce new large-scale structures; rather, it enhances the visibility of features already present in the individual acquisitions by increasing the signal-to-noise ratio. Elongated dark features interpreted as potential paleochannel expressions can be traced more clearly in the stacked image, providing an improved basis for the subsequent amplitude, coherence, phase, and texture analyses.

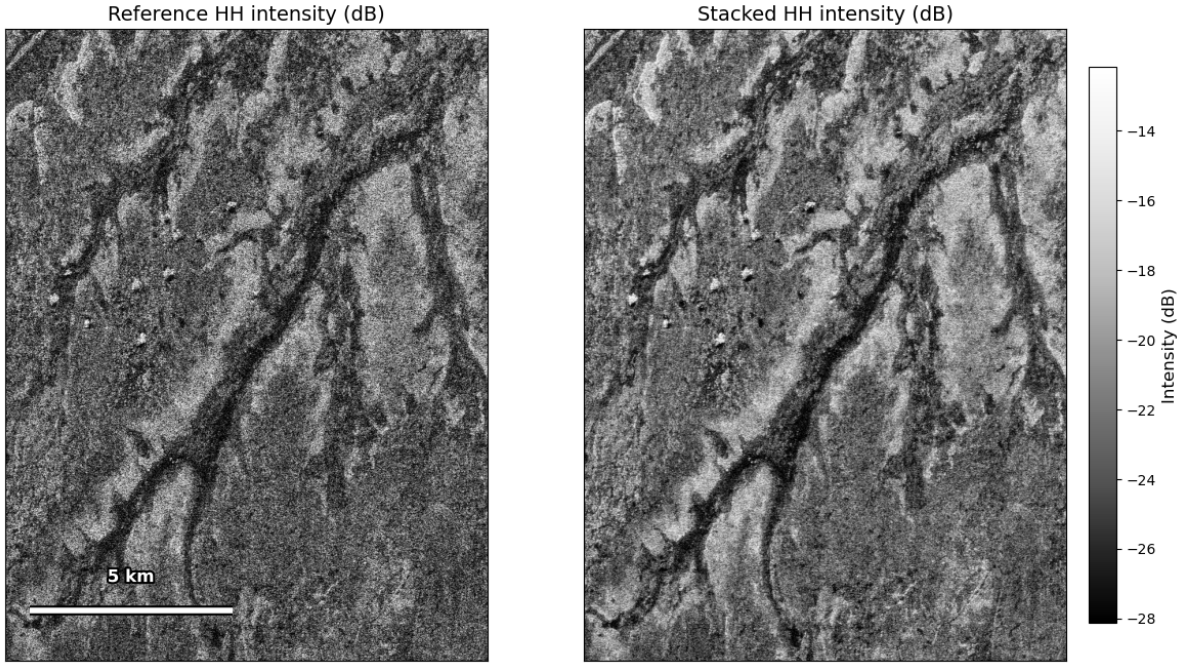

Figure 4.1: Comparison between a single HH intensity acquisition acquired on 1 May 2026 and a temporally stacked HH intensity image generated from acquisitions between 28 April and 13 May 2026.

4.2. Phase and amplitude analysis

Figure 4.2 presents the stacked polarimetric amplitude images for the Sahara study area. The HH and VV channels exhibit similar large-scale spatial patterns, with prominent linear and dendritic geomorphic features clearly visible across the scene. Areas of high backscatter are associated with rougher surface conditions and topographic boundaries, whereas smoother sedimentary surfaces appear darker. The HV channel generally exhibits lower backscatter levels and enhanced contrast between major geomorphic units, reducing the influence of strong surface returns observed in the co-polarized channels.

The HH and VV amplitude images exhibit similar spatial patterns and feature contrast throughout much of the scene. Nevertheless, subtle differences in feature contrast can be observed, particularly along elongated drainage-like structures and topographic transitions. The cross-polarized HV and VH images exhibit broad brightness increases near the scene boundaries that are not associated with discernible geomorphic features. Because these variations are aligned with the acquisition geometry and occur consistently across large portions of the swath, they are interpreted as radiometric artefacts rather than geomorphological features.

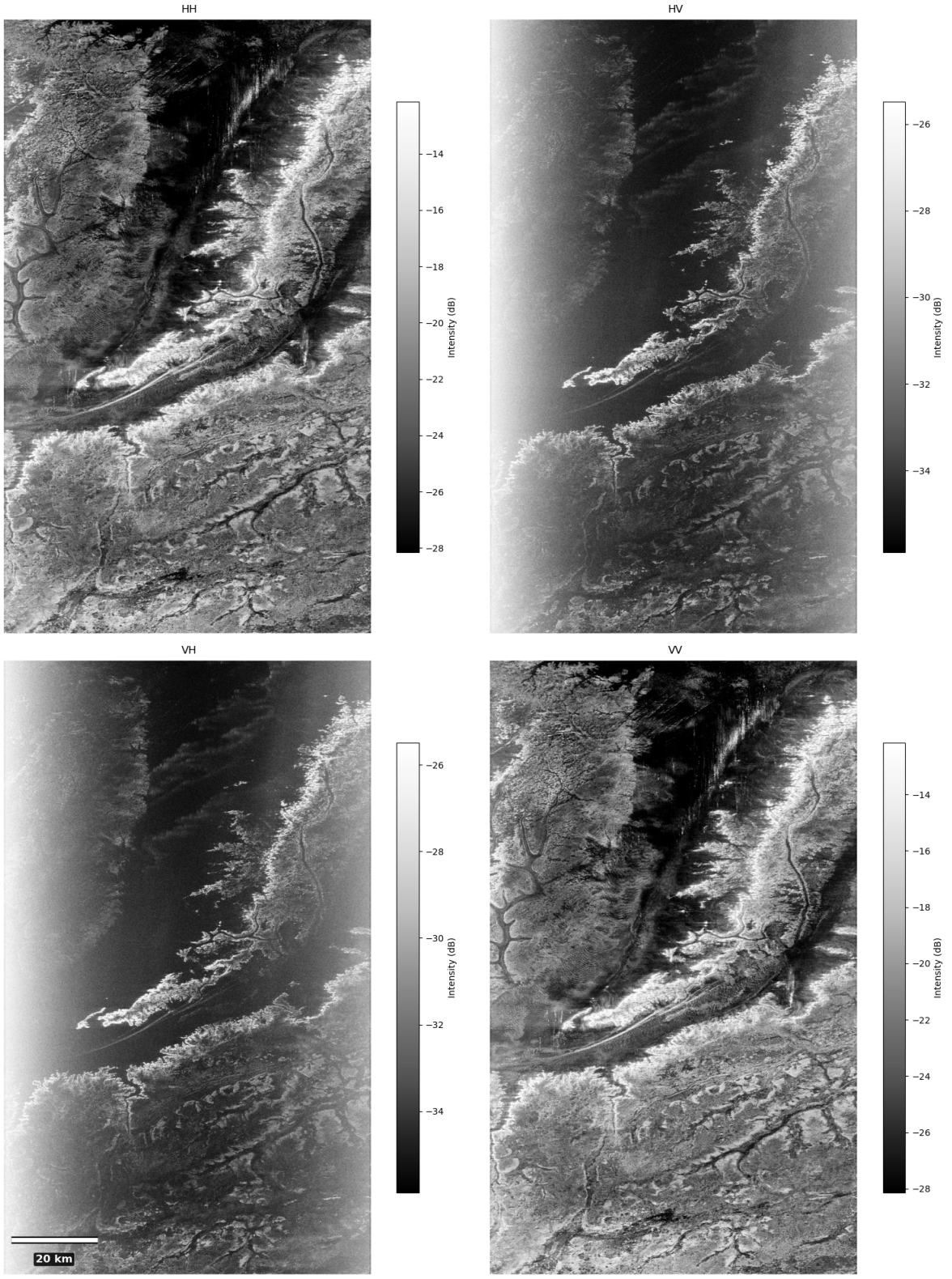

Figure 4.2: Stacked HH, HV, VH, and VV backscatter images for the reference scene located in the Sahara acquired in May 2026. For visualisation purposes, the cross-polarized channels (HV and VH) are displayed using a different intensity scale than the co-polarized channels (HH and VV) because of their substantially lower backscatter levels.

Figure 4.3 shows the stacked HH phase, VV phase, and the corresponding HH-VV phase difference. The HH and VV phase images represent the wrapped phase of the complex SAR signal, displayed

within the interval $[-\pi, \pi]$. Individually, these phase measurements appear completely random and do not reveal readily interpretable spatial patterns because the absolute phase is dominated by geometric and scattering-related contributions that vary at the pixel scale. In contrast, the HH-VV phase-difference product suppresses phase components common to both channels and reveals coherent spatial structures that correspond to geomorphic features visible in the amplitude imagery. Several drainage-like and topographic features become distinguishable in the phase-difference image, indicating spatial variations in the relative scattering response of the two co-polarized channels.

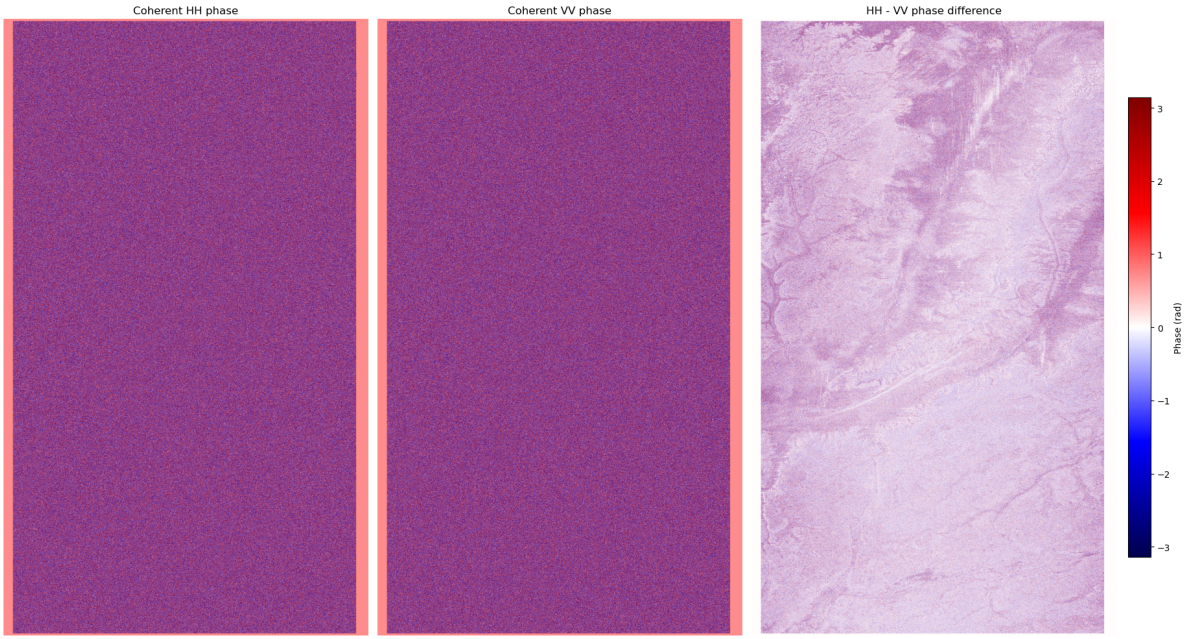

Figure 4.3: Wrapped HH phase, wrapped VV phase, and the corresponding HH-VV phase difference for the Sahara study area. Phase values are displayed in the range $[-\pi, \pi]$ rad.

An analogous analysis was performed for the HV-VV phase difference. The resulting phase-difference image reveals coherent spatial patterns associated with several geomorphic features, although it exhibits greater local variability than the HH-VV product owing to the lower signal-to-noise ratio of the cross-polarized HV channel. Because the subsequent analyses focus on co-polarized observables and coherence-based retrievals, the HV-VV phase-difference results are presented in Appendix C.1.1.

Cross-sections through the Sahara and Namibia study areas were extracted in both range and azimuth directions, and average phase values within the paleochannel were compared with adjacent background regions. While both the HH-VV and HV-VV phase-difference products exhibit spatial variability that reflects regional geomorphological structure, no consistent phase anomaly associated specifically with the mapped paleochannels was observed. Mean phase values within the paleochannels were generally comparable to those of the surrounding terrain, and channel-background contrasts remained small relative to the observed spatial variability. Examples of the raw and averaged cross-sectional analysis are provided in Appendix C.1.

To assess whether the observed phase patterns persist beyond the reference scene, the HH-VV phase-difference product was examined across the full BIOMASS swath coverage (Figure 4.4). The reference scene analysed in this chapter is outlined by the red polygon. Coherent drainage-like and dendritic patterns remain visible over much larger spatial extents, indicating that the phase-difference imagery contains organised regional-scale structure rather than isolated local anomalies.

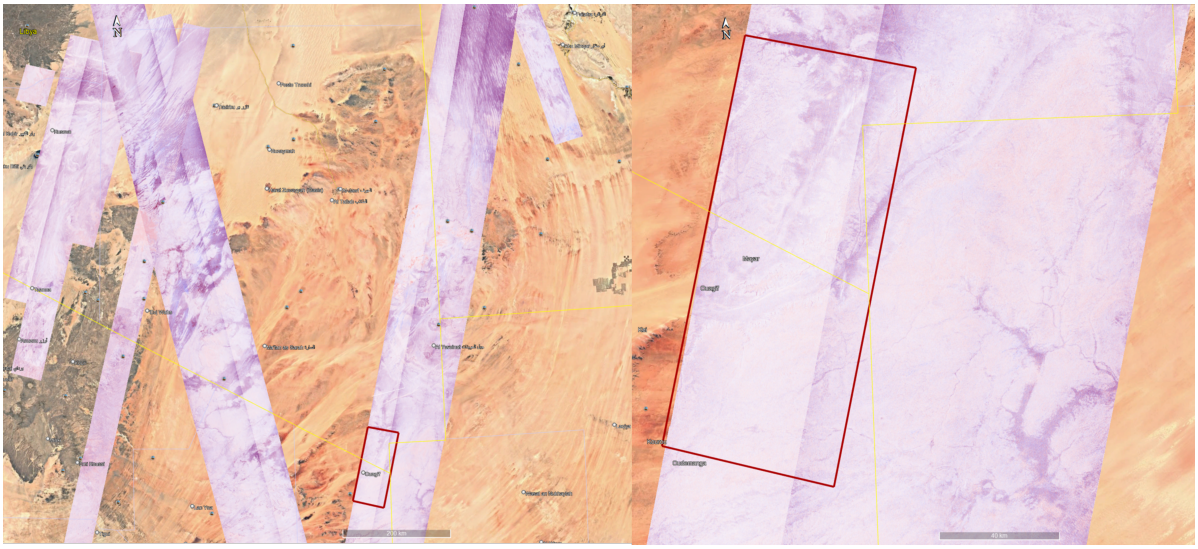

Figure 4.4: HH-VV phase-difference imagery displayed over the full BIOMASS swath coverage. The red polygon indicates the reference scene analysed in this study. Right: enlarged view of the highlighted area showing coherent drainage-like and dendritic phase patterns visible within the phase-difference product.

4.2.1. Difference between L-band and P-band

Figure 4.5 compares the same region in BIOMASS P-band imagery, the JAXA ALOS PALSAR-2 annual L-band mosaic (Japan Aerospace Exploration Agency (JAXA) Earth Observation Research Center, 2025), and optical imagery. The optical image was obtained from Google Earth and is included as a high-resolution visual reference. Because Google Earth imagery may originate from different sensors and acquisition dates, it should be interpreted as contextual information rather than as a temporally coincident observation. The highlighted regions illustrate how different geomorphological features are expressed across the three datasets.

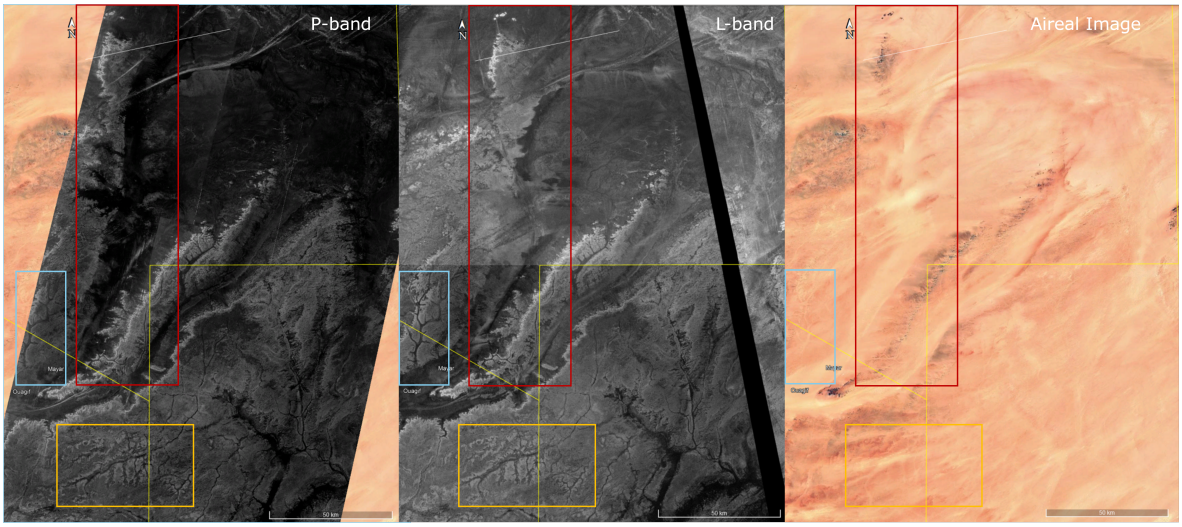

Figure 4.5: Comparison of the study area in BIOMASS P-band imagery, the JAXA ALOS PALSAR-2 annual L-band mosaic, and optical imagery displayed in Google Earth. The red, blue, and yellow boxes highlight representative features discussed in the text.

The red box encloses a broad linear to curvilinear feature that is visible in all three images. However, its appearance differs substantially between wavelengths. In the L-band image, the feature exhibits strong contrast and appears as a prominent surface-related structure, whereas in the P-band image its boundaries are more diffuse and the surrounding terrain contributes more strongly to the observed radar

response. This behaviour is consistent with the expected increased penetration capability of P-band radar, for which the measured signal may contain a greater contribution from subsurface scattering in addition to the surface expression visible at L-band.

The blue box highlights a smaller channel-like feature that can be identified in both radar datasets. The feature remains recognisable in the optical imagery, indicating that at least part of the observed response is associated with a surface geomorphological expression.

Finally, the yellow box highlights a dendritic drainage-shaped network. The network is clearly expressed in the BIOMASS P-band image as a spatially coherent system of branching channels, whereas its expression is weaker and less continuous in the L-band image. In the optical imagery, only subtle tonal variations are visible and the network is considerably more difficult to trace as a coherent geomorphological feature. The enhanced visibility of this drainage pattern at P-band is consistent with an increased sensitivity to variations in surface and near-subsurface dielectric properties, roughness, or buried geomorphological structure. Although these observations alone do not prove a subsurface origin, they demonstrate that P-band imagery can provide additional information beyond that available from optical and shorter-wavelength radar observations.

Overall, the comparison shows that BIOMASS P-band observations preserve the major geomorphological patterns visible in the L-band and optical imagery. Several drainage-related features appear with clear spatial continuity in the P-band image and remain identifiable across the highlighted regions.

4.2.2. Decompositions

To investigate the dominant scattering mechanisms within the study area, a Pauli decomposition was generated using the ESA `PolSARpro` toolbox (Pottier, 2012). The decomposition expresses the polarimetric radar response in terms of three physically interpretable scattering components: odd-bounce scattering, even-bounce scattering, and volume scattering.

Figure 4.6 shows the Pauli RGB decomposition together with the individual decomposition components and an optical reference image. The analysis focuses on the same paleochannel feature highlighted in Figure 4.1 and the feature outlined by the yellow box in Figure 4.5, allowing the scattering behaviour of these representative features to be examined in the decomposition products. In the Pauli RGB image, blue represents odd-bounce scattering ($|S_{HH} + S_{VV}|^2$), green represents volume scattering ($2|S_{HV}|^2$), and red represents even-bounce scattering ($|S_{HH} - S_{VV}|^2$). Odd-bounce scattering is commonly associated with surface-dominated reflections, whereas even-bounce scattering is typically produced by dihedral scattering geometries. Volume scattering represents depolarizing scattering processes within structurally heterogeneous media.

The Pauli RGB image is dominated by blue and green tones, indicating that odd-bounce and volume scattering contribute most strongly to the observed P-band backscatter. Several paleochannel features visible in the optical imagery correspond to distinct colour variations within the Pauli image, suggesting changes in the relative contribution of the different scattering mechanisms across the channel system. In contrast, red tones associated with even-bounce scattering are largely absent throughout the scene.

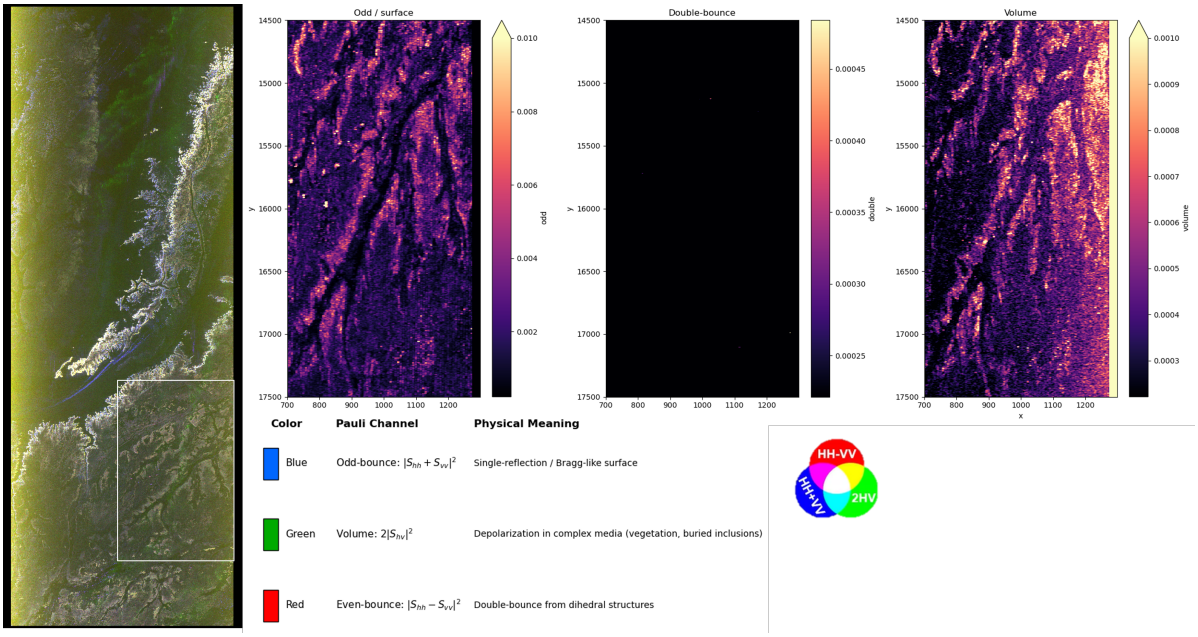

Figure 4.6: Pauli RGB decomposition and corresponding decomposition components for the Sahara study area. In the Pauli RGB image, blue represents odd-bounce scattering, green represents volume scattering, and red represents even-bounce scattering. The optical image is included for visual comparison, while the three panels on the right show the individual odd-bounce, even-bounce, and volume scattering components.

To further investigate the observed patterns, the individual decomposition components were examined separately. The odd-bounce component exhibits numerous linear and channel-like features that closely follow the geomorphology visible in the optical image. Several branches and margins of the paleochannel network appear brighter than the surrounding terrain, indicating an enhanced odd-bounce scattering contribution.

The even-bounce component displays very low power across almost the entire scene and contains only a small number of isolated bright pixels. No coherent large-scale spatial structures are visible, indicating that even-bounce scattering contributes only minimally to the overall radar response of the study area.

The volume scattering component exhibits spatially extensive variability across the study area and highlights several of the same linear and channel-like features visible in the odd-bounce component. Many of the paleochannel-related structures identified in the optical imagery and Pauli RGB decomposition remain visible in both components, although their relative contrast varies across the scene. In contrast, the double-bounce component displays very low power throughout most of the study area and contains only a small number of isolated bright pixels.

Overall, the decomposition results indicate that the radar response is dominated by a combination of odd-bounce and volume scattering, while even-bounce scattering is negligible. Paleochannel features are expressed in both the odd-bounce and volume scattering components, although their visibility is generally strongest in the volume scattering image. This suggests that variations in both surface scattering and depolarizing scattering processes contribute to the observed radar signatures of the paleochannel system.

4.3. Effective penetration depth inversion

4.3.1. Comparison of Fresnel and I2EM retrieval results

Figure 4.7 presents the input datasets used for the depth-inversion workflow, including calibrated HH and VV backscatter, interferometric coherence magnitude, and local incidence angle. The co-polarized backscatter channels exhibit similar spatial patterns, with elevated backscatter associated with major geomorphological features and reduced backscatter over smoother terrain. Interferometric coherence

is generally high throughout the scene, while incidence angle increases systematically from approximately 23° in near range to 28° in far range.

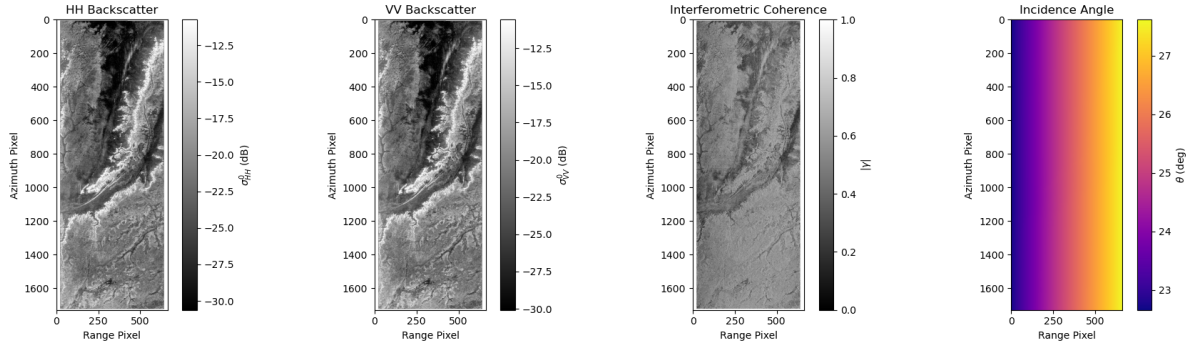

Figure 4.7: Input datasets used for the depth inversion workflow, including HH backscatter (σ^0_{HH}), VV backscatter (σ^0_{VV}), interferometric coherence ($|\gamma|$), and incidence angle (θ).

Using these inputs, dielectric constant (ε'), normalised roughness (k_s), and effective penetration depth (d_{eff}) were retrieved using both the simplified Fresnel LUT (Model 1) and the physically based I2EM LUT (Model 2). Figure 4.8 compares the resulting retrieval products.

Both retrieval approaches reproduce similar large-scale spatial patterns. The dominant curvilinear features visible throughout the study area are evident in both models, demonstrating that the inversion identifies consistent geomorphological structures regardless of the forward-scattering formulation. However, substantial differences are observed in the retrieved dielectric constant and roughness values. The Fresnel inversion generally retrieves higher dielectric constants and lower roughness values, whereas the I2EM inversion attributes a larger fraction of the observed backscatter to rough-surface scattering and therefore retrieves systematically higher roughness. Additional regional roughness retrievals are provided in Appendix Figure C.9. This behaviour is particularly evident in the roughness-difference map, which shows a predominantly negative bias for $\Delta k_s = k_{s,\text{Fresnel}} - k_{s,\text{I2EM}}$ across much of the scene.

The dielectric retrievals also exhibit substantial model dependence. Although both methods recover extensive regions of low dielectric constant consistent with dry surface conditions, the corresponding difference map reveals widespread local variability. A pronounced accumulation of solutions occurs near the lower dielectric boundary.

In contrast, the effective penetration depth estimates exhibit much stronger consistency. Regions of relatively shallow and deep penetration are reproduced by both retrieval frameworks, and the depth-difference map reveals only moderate local deviations. Compared with the intermediate dielectric and roughness products, the depth retrievals retain substantially more agreement in both magnitude and spatial organization.

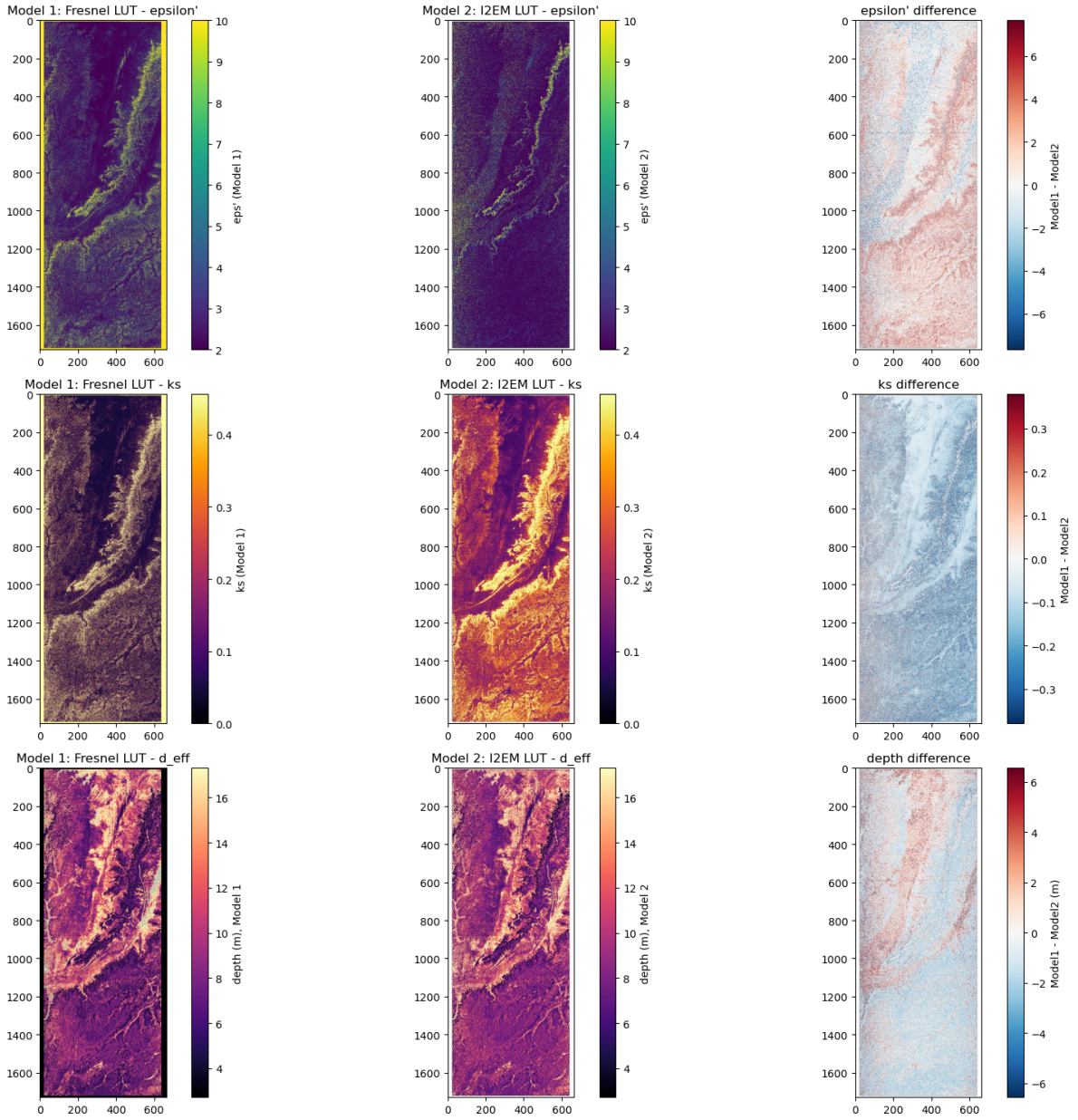

Figure 4.8: Comparison of retrieval results obtained using the Fresnel LUT (left column) and I2EM LUT (centre column). The right column shows the corresponding difference maps ($\mathrm{Fresnel} - \mathrm{I2EM}$) for dielectric constant, normalised roughness, and effective penetration depth.

The differences between retrieval products are further illustrated by pixel-wise model comparisons (Figure 4.9). The dielectric retrievals exhibit the weakest agreement and show pronounced clustering at LUT boundaries, particularly near the lower dielectric limit. The roughness retrievals display moderate agreement but retain substantial scatter, reflecting the trade-off between dielectric constant and surface roughness in the inversion. In contrast, the depth retrieval exhibits a clear positive relationship and remains closer to the one-to-one line than either intermediate parameter. The effective penetration depth comparison yields a correlation coefficient of 0.924, a bias of 0.067 m, and an RMSE of 1.61 m.

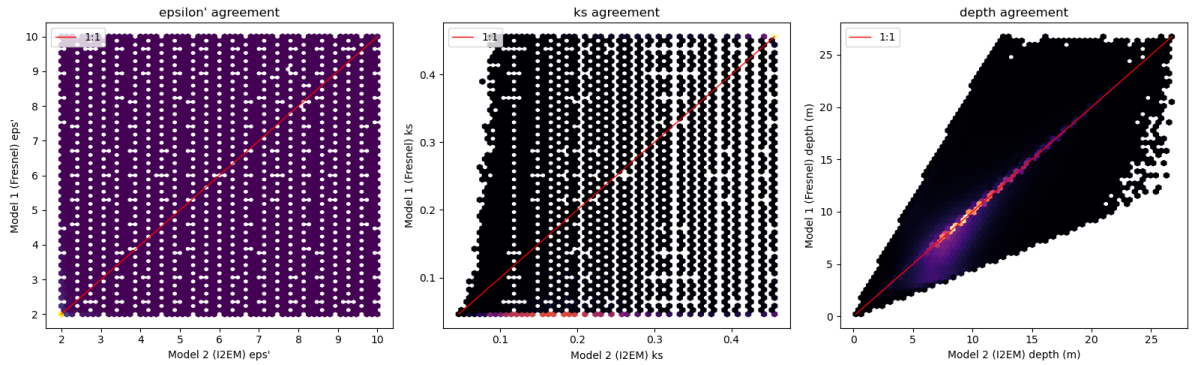

Figure 4.9: Pixel-wise comparison of Fresnel and I2EM retrievals for dielectric constant, normalised roughness, and effective penetration depth. The red line denotes the one-to-one relationship.

Additional inversion-conditioning and residual-cost diagnostics are provided in Appendix C.2 (Figure C.8). The Fresnel LUT generally exhibits larger cost-gap values, suggesting stronger separation between competing solutions, whereas the I2EM LUT frequently produces smaller cost gaps, indicating greater inversion non-uniqueness. Both retrieval frameworks achieve low residual costs across most of the study area, although elevated residuals occur locally along several geomorphological structures.

To further visualise the effective depth products, Figure 4.10 presents three-dimensional renderings of the retrieved effective penetration depth. They provide a visual representation of the estimated subsurface scattering volume from which coherent P-band backscatter may originate. Larger retrieved values indicate a greater vertical extent of coherent scattering contributions, whereas smaller values suggest a more confined scattering volume. Both models reproduce nearly identical large-scale penetration patterns, with local differences largely confined to regions exhibiting stronger dielectric and roughness contrasts. Consistent with the pixel-wise comparison, the depth retrieval shows substantially greater robustness than the intermediate dielectric and roughness estimates.

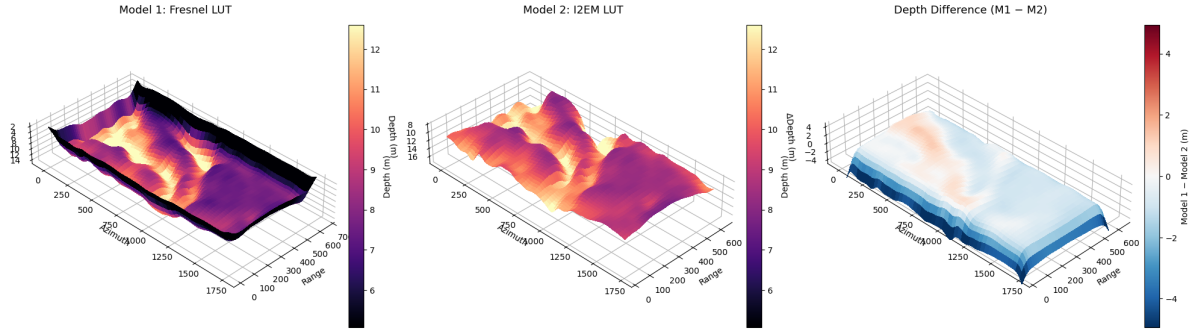

Figure 4.10: Three-dimensional visualisation of the effective penetration depth derived from the Fresnel LUT (Model 1), the I2EM LUT (Model 2), and the resulting difference ($d_{\mathrm{eff,M1}} - d_{\mathrm{eff,M2}}$). The retrieved values represent the estimated subsurface volume from which detectable radar backscatter could potentially originate rather than the depth to a discrete buried reflector.

Additional retrieval diagnostics, including parameter-distribution comparisons, retrieval-difference histograms, LUT-response analyses, and derived vertical-wavenumber products, are provided in Appendix C.2.

4.3.2. Volumetric moisture inversion

Dielectric-equivalent moisture estimates were derived from the retrieved dielectric constants using the Topp, Dobson, and CRIM dielectric mixing models for both the Fresnel- and I2EM-based inversion results (Figure 4.11).

For each inversion framework, all three mixing models produce highly similar spatial patterns and consistently delineate the same major geomorphological features. The principal differences are ob-

served in the retrieved moisture magnitudes. The Topp model generally yields slightly higher moisture-equivalent values, whereas the Dobson and CRIM models produce very similar results. The differences between the Fresnel- and I2EM-based moisture products are larger than those introduced by the choice of dielectric mixing model. Nevertheless, the principal channel-like structures and regional trends remain visible across all retrievals, indicating that the spatial distribution of moisture anomalies is robust to both the selected dielectric mixing model and inversion framework.

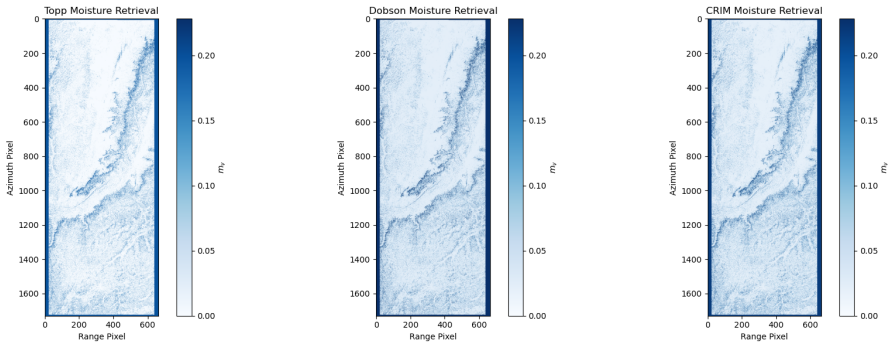

(a) Dielectric-equivalent moisture retrievals derived from the Fresnel inversion framework.

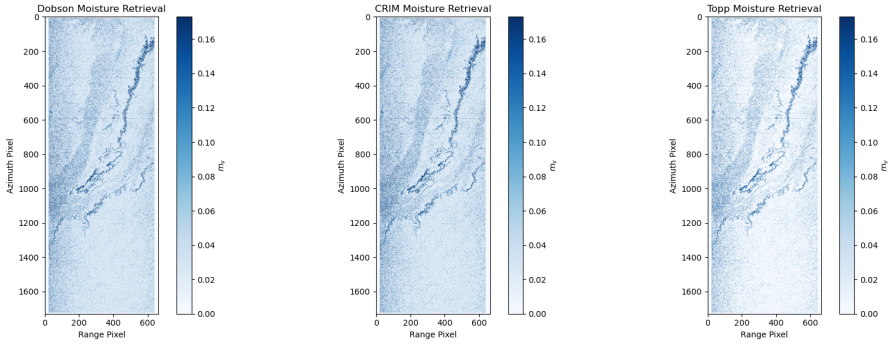

(b) Dielectric-equivalent moisture retrievals derived from the I2EM inversion framework.

Figure 4.11: Comparison of dielectric-equivalent moisture retrievals obtained using the Topp, Dobson, and CRIM dielectric mixing models. The upper row shows moisture estimates derived from the Fresnel inversion framework, whereas the lower row shows moisture estimates derived from the I2EM inversion framework.

4.3.3. Regional-scale effective penetration depth inversion results

To assess the spatial behaviour of the retrieval framework at regional scale, the inversion was applied to all available BIOMASS acquisitions covering the Kufrah Basin and Namib Desert study areas. Each Level-1C stack comprises seven acquisitions, and all acquisitions contained within the available stacks were included in the analysis. Figure 4.12 shows the retrieved dielectric constant, and effective penetration depth products for the Kufrah Basin, while Figure 4.14 presents the corresponding results for the Namib Desert.

The regional products were generated using the interferometric pair with a perpendicular baseline as close as possible to 2500 m within each stack, which generally corresponded to the largest available baseline. The influence of baseline selection on the retrieval is examined separately in Section 5.3.3.

Kufrah Basin and Southern Transition Zone

Regional-scale retrievals were generated for the full BIOMASS coverage of the Kufrah Basin and the adjacent transition zone extending southward toward the Sahel (Figures 4.12 and 4.13). The resulting dielectric constant, dielectric-equivalent moisture content, and effective penetration depth products exhibit spatially coherent patterns across multiple adjacent BIOMASS frames and capture pronounced environmental gradients across northern Africa.

Within the Kufrah Basin, the retrieved dielectric constant is characterised by a predominantly low-background response, with most areas exhibiting values of approximately $\varepsilon' \approx 2 - 3$. Superimposed

on this background are numerous spatially coherent linear, branching, and dendritic anomalies that remain continuous across multiple BIOMASS frames. Several isolated high-dielectric anomalies are also visible as compact circular to irregular features, locally reaching $\varepsilon' > 8$.

The effective penetration depth product exhibits broad spatial coherence across multiple adjacent BIOMASS frames and preserves several large-scale regional patterns. Most of the basin is characterised by relatively homogeneous effective penetration depths, with values typically ranging from approximately 4 to 8 m. Localised variations and geomorphological structures remain visible throughout the mosaic, although the depth product displays substantially lower spatial contrast than the corresponding dielectric-constant retrieval. In a few isolated areas, retrieved depths approach the upper end of the retrieval range; however, these values should be interpreted with caution because they are associated with low coherence conditions.

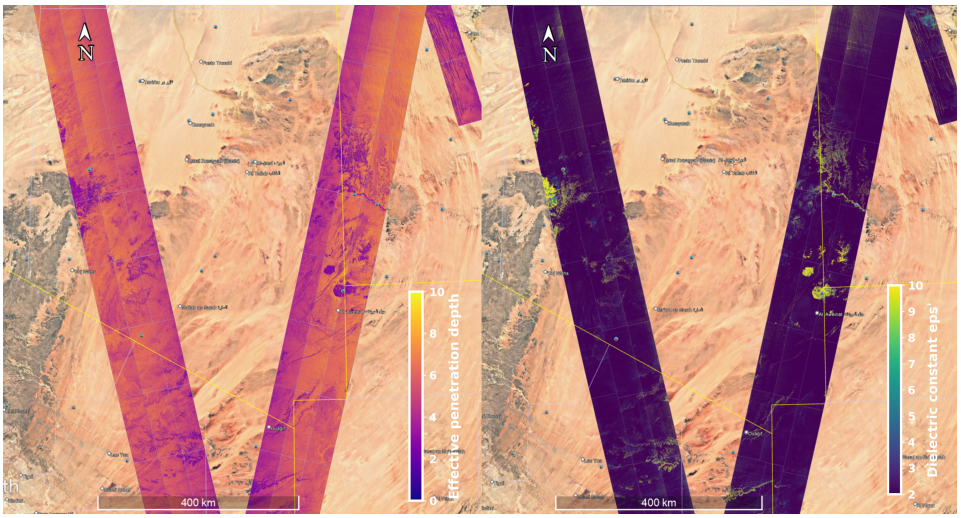

Figure 4.12: Regional retrieval results for the Kufrah Basin derived from BIOMASS Level-1C observations. The retrieved dielectric constant (ε') and effective penetration depth (d_{eff}) products exhibit spatially coherent patterns across multiple adjacent BIOMASS frames. Several linear and dendritic anomalies remain continuous over large distances and are visible across frame boundaries, demonstrating the preservation of regional-scale geomorphological structure within the inversion products.

South of the Kufrah Basin (4.13), a marked transition is observed from hyper-arid desert conditions into a more vegetated and climatically variable environment. This transition is associated with a substantial increase in both retrieved dielectric constant and dielectric-equivalent moisture content. Whereas the northern desert regions remain dominated by low dielectric values and sparse anomalies, the southern scenes display widespread elevated dielectric and moisture-equivalent responses, forming extensive interconnected networks and broad spatially continuous zones. Concurrently, the effective penetration depth decreases across large portions of the southern mosaic, producing a clear regional contrast relative to the more arid northern environments.

The observed transition is spatially coherent across multiple BIOMASS frames and is evident in all three retrieved products. The systematic increase in dielectric and moisture-equivalent values, accompanied by reduced effective penetration depths, is consistent with the expected shift from extremely dry desert conditions toward environments with increased vegetation cover, soil moisture, and surface complexity. The continuity of these patterns across frame boundaries further demonstrates the capability of the inversion framework to preserve large-scale regional structure over continental-scale BIOMASS mosaics.

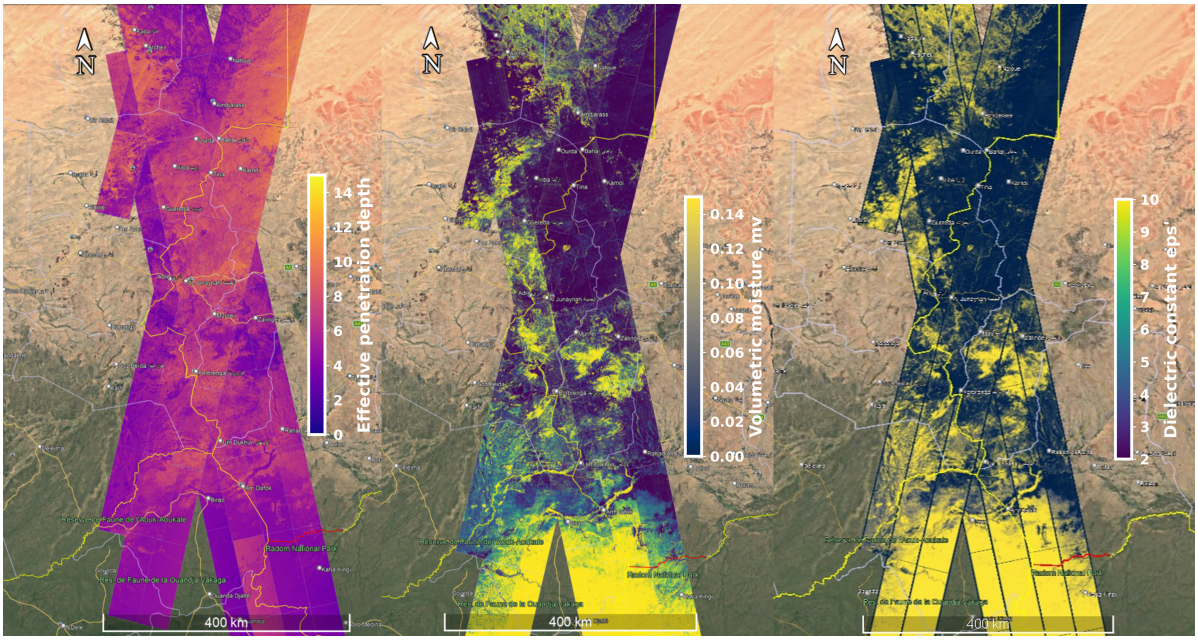

Figure 4.13: Regional retrieval results for the southern transition zone between the Sahara and the Sahel. From left to right: effective penetration depth (d_{eff}), dielectric-equivalent volumetric moisture content (m_v), and dielectric constant (ε'). The retrievals show a pronounced regional transition from hyper-arid desert conditions in the north to increasingly elevated dielectric and moisture-equivalent responses toward the south, accompanied by reduced effective penetration depths.

Namib Desert

The retrieval framework was also applied to the Namib Desert study area (Figure 4.14). Figure 4.14 presents the regional effective penetration depth retrievals derived from both descending and ascending acquisitions, together with the corresponding dielectric constant and moisture-equivalent products.

The regional products exhibit pronounced spatial variability across the BIOMASS coverage. In both the ascending and descending retrievals, large-scale geomorphological structures remain visible throughout the mosaic. The Namib Sand Sea appears as a continuous north-south corridor characterised by relatively homogeneous retrieval values and clearly expressed linear dune morphology. In contrast, the terrain east of the dune field exhibits greater spatial variability, with numerous linear, branching, and irregular patterns visible across multiple BIOMASS frames.

The dielectric constant and moisture-equivalent products show a strong contrast between the dune field and the eastern part of the study area. The Namib Sand Sea is characterised by comparatively low dielectric constants, generally ranging between approximately $\varepsilon' \approx 2-4$, and corresponding moisture-equivalent values of roughly $m_v \approx 0.00-0.04$. In contrast, the more heterogeneous terrain east of the dune field exhibits substantially higher dielectric constants, commonly reaching $\varepsilon' \approx 5-8$ and locally exceeding $\varepsilon' \approx 9$, with moisture-equivalent values frequently above $m_v \approx 0.06$ and locally approaching 0.15.

The effective penetration depth products display lower spatial contrast than the dielectric and moisture-equivalent maps but preserve several large-scale geomorphological patterns. Most of the study area is characterised by effective penetration depths of approximately 3-6 m, while localized regions exceed 6 m and occasionally approach 8-10 m. The linear dune systems remain clearly visible in both retrievals, and major geomorphological boundaries can be traced across multiple adjacent frames despite localized scene-to-scene variations.

Several drainage-related and topographically controlled linear features can also be identified within the eastern portion of the study area. However, no distinct signatures attributable to the narrow interdune paleochannels reported by Paillou et al. (2020) were identified in the regional BIOMASS products.

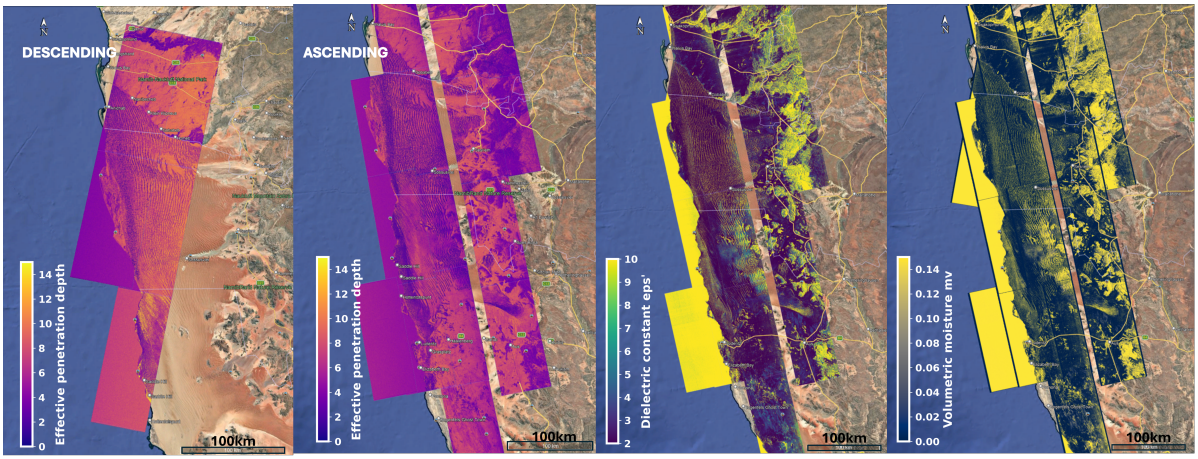

Figure 4.14: Regional retrieval results for the Namib Desert study area derived from BIOMASS Level-1C observations. From left to right: effective penetration depth retrieved from the descending acquisition, effective penetration depth retrieved from the ascending acquisition, retrieved dielectric constant (ε'), and dielectric-equivalent volumetric moisture content (m_v).

4.3.4. Ascending versus descending acquisitions

To assess the sensitivity of the retrieval framework to acquisition geometry, retrieval products derived from ascending and descending BIOMASS acquisitions were compared over their common area of overlap. The comparison is not intended as a direct validation because the two acquisitions correspond to different BIOMASS sub-swaths, viewing geometries, acquisition dates, and coherence conditions. Instead, the analysis investigates whether major spatial patterns remain identifiable across independent observations of the same region.

Figure C.10 in Appendix C.3 shows the spatial overlap between the ascending and descending scenes. Although the footprints are not identical, a substantial central region is covered by both acquisitions and was used for subsequent comparisons.

The retrieved dielectric constant, volumetric moisture content, and effective penetration depth are shown for both acquisitions in Figure 4.15. Despite the different acquisition geometries, several elongated linear structures and broad spatial trends are visible in both products. In particular, the principal geomorphological patterns observed in the effective penetration depth retrieval are preserved across both viewing geometries. However, the difference maps reveal substantial local variability and coherent acquisition-dependent patterns, indicating that the absolute parameter values remain sensitive to viewing geometry, incidence angle, and retrieval uncertainty.

The effective penetration depth retrievals exhibit the strongest qualitative agreement between acquisitions. Both scenes recover several common depth anomalies and reproduce many of the same large-scale geomorphological structures. However, the pixel-wise correspondence is substantially weaker than the visual similarity of the maps might suggest, indicating that the retrieval is more robust in terms of identifying relative spatial patterns than providing directly comparable absolute depth estimates. Local differences are observed throughout the overlap region, particularly along narrow linear features and near scene boundaries.

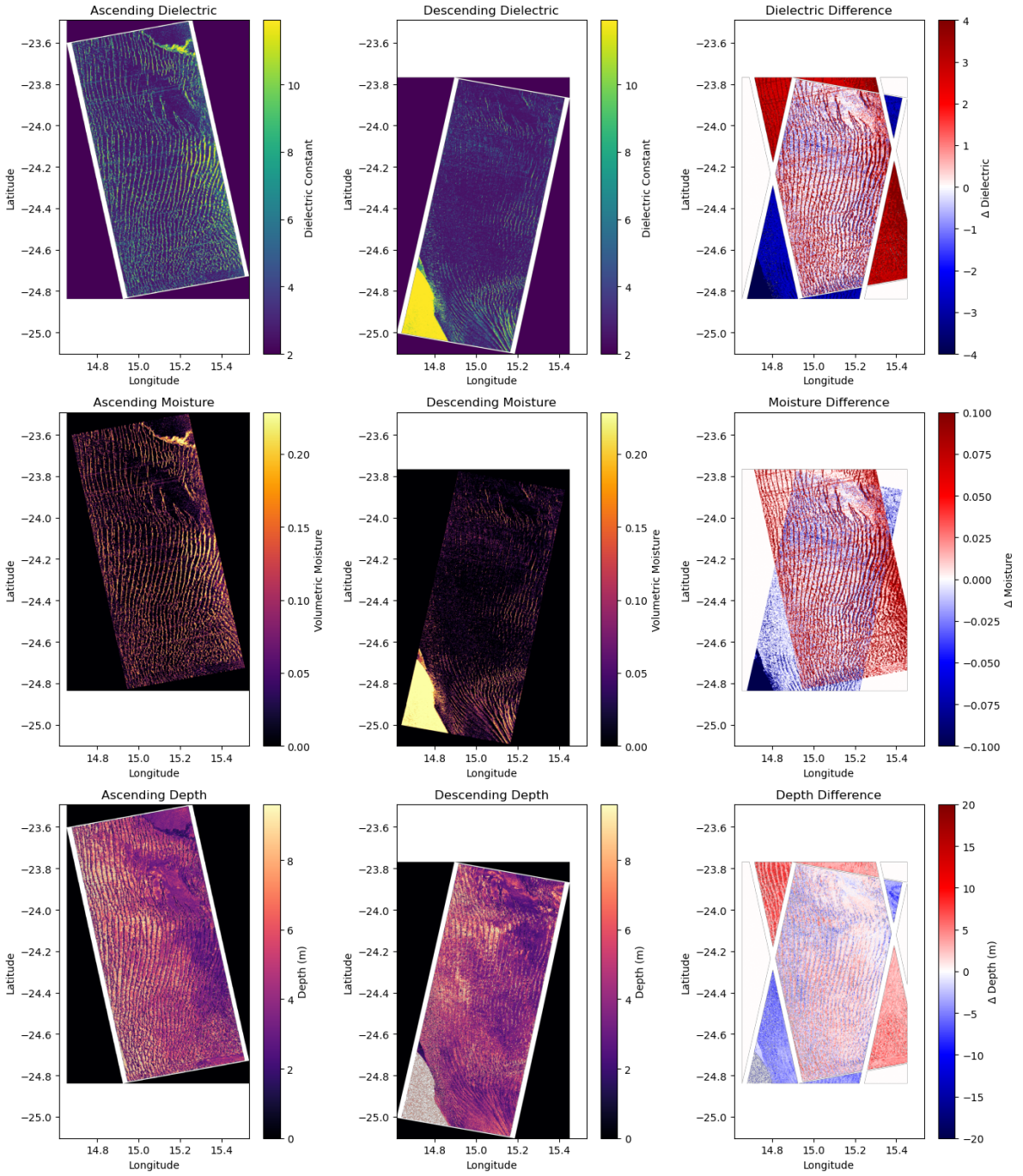

Figure 4.15: Comparison of ascending and descending retrieval products. Rows show dielectric constant, volumetric moisture content, and effective penetration depth. Difference maps are computed as ascending minus descending.

A quantitative comparison of the depth retrievals is shown in Figure 4.16. The scatter-density plot demonstrates substantial dispersion and departs noticeably from the one-to-one relationship at moderate and larger depths. Although a positive relationship exists between the two acquisitions, the binned-median trend deviates from the one-to-one line and becomes relatively stable at depths of approximately 4-5 m. This behaviour indicates that effective penetration depth estimates derived from different acquisition geometries are not directly interchangeable, particularly for deeper retrievals.

The Bland-Altman analysis yields a mean bias of 0.29 m, with the ascending retrieval producing slightly larger depth estimates than the descending retrieval. However, the limits of agreement are wide, with ± 1.96 standard deviations corresponding to approximately 7.1 m. Furthermore, the spread of differ-

ences increases with increasing depth, suggesting that retrieval uncertainty becomes progressively larger for deeper penetration estimates.

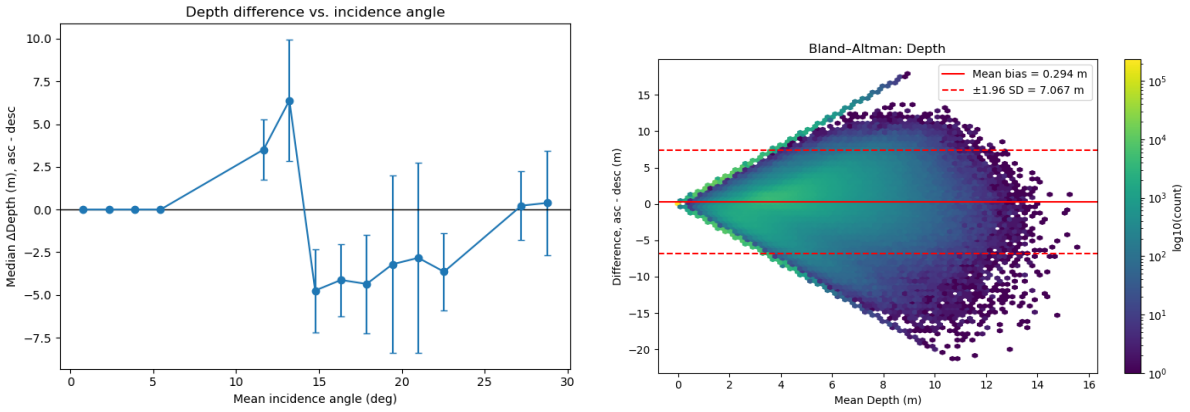

(a) Pixel-wise comparison

(b) Bland-Altman analysis

Figure 4.16: Comparison of effective penetration depth retrieved from ascending and descending acquisitions.

The empirical cumulative distribution function of the absolute depth differences further illustrates the level of agreement between acquisitions. Approximately 50% of overlapping pixels differ by less than 1.9 m, while 80% and 90% of pixels differ by less than 4.4 m and 6.1 m, respectively. These statistics indicate that the retrieval is reasonably consistent for broad-scale spatial characterisation, while substantial local differences remain present throughout the overlap region.

The dielectric retrieval exhibits substantially larger discrepancies than the depth product and demonstrates only weak pixel-wise consistency between acquisitions. Figure C.12 in the Appendix shows that dielectric estimates are poorly correlated at the pixel level and display strong clustering near the lower LUT boundary. The binned-median relationship departs markedly from the one-to-one line and varies only weakly across the retrieval range, indicating that the dielectric solutions are strongly influenced by inversion non-uniqueness and LUT constraints.

The Bland-Altman analysis indicates a positive mean bias of approximately 0.88 dielectric units, demonstrating that the ascending retrieval generally produces larger dielectric estimates than the descending retrieval. The spread of differences is also considerable, with limits of agreement approaching ± 6.6 dielectric units. Together with the observed boundary clustering, this suggests that dielectric retrievals remain strongly affected by acquisition geometry, lookup-table design, and the inherent ambiguity between dielectric constant and surface roughness within the inversion process.

Additional ascending-descending comparison diagnostics, including incidence-angle sensitivity, cumulative distribution functions of retrieval differences, coherence maps, and overlap visualisations, are presented in Appendix C.3. These analyses indicate that part of the observed variability is associated with changes in viewing geometry and incidence angle, although the magnitude of the differences suggests that inversion non-uniqueness also plays an important role.

Overall, the ascending and descending acquisitions reproduce several common large-scale geomorphological patterns despite differences in viewing geometry, incidence angle, coherence, and acquisition date. However, the comparison demonstrates that agreement in the retrieved physical parameters is considerably weaker at the pixel scale. The strongest consistency is observed in the persistence of broad spatial structures and depth anomalies rather than in exact numerical agreement. Effective penetration depth shows moderate robustness across acquisitions, whereas dielectric constant remains strongly affected by retrieval ambiguity and lookup-table boundary effects.

4.4. Validation methods

The workflow was evaluated using a combination of synthetic modelling, geomorphological validation, and comparison with independent remote-sensing datasets. The following sections present re-

sults from a synthetic paleochannel model, regional drainage-network analyses, and comparisons with Sentinel-2-derived indicators.

4.4.1. Validation model results

A synthetic paleochannel model was constructed to evaluate the proposed retrieval workflow under controlled conditions. The model consists of a meandering buried calcified pebble-gravel (CPG) reflector embedded within a homogeneous modern sand-sheet (MSS) background at a depth of 1.5 m. Figure 3.5 presents the prescribed model parameters, including dielectric properties, moisture content, surface roughness, and reflector geometry.

The simulated BIOMASS observables are shown in Figure 4.17. The buried channel produces coherent anomalies in HH and VV backscatter, co-polarized backscatter difference, HH-VV phase difference, and interferometric coherence. The resulting phase and coherence signatures closely follow the prescribed channel geometry and are spatially coincident with the subsurface reflector.

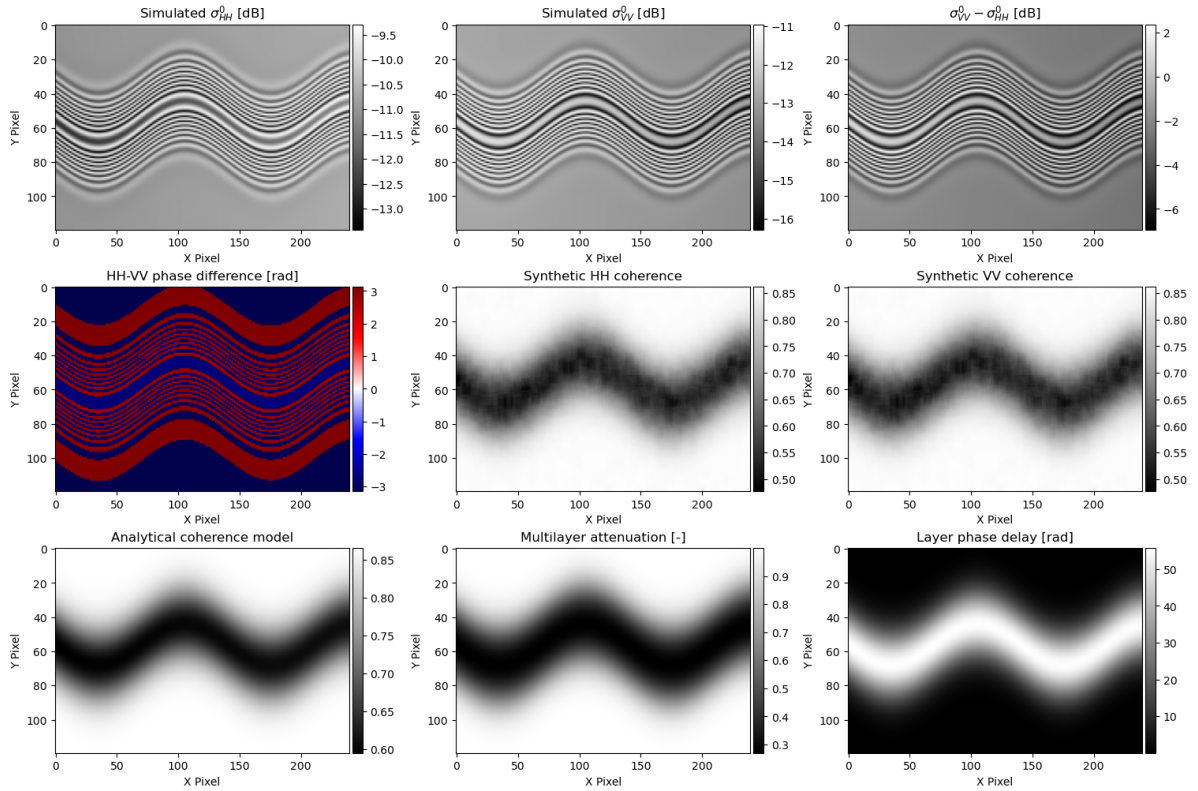

Figure 4.17: Simulated BIOMASS observables derived from the synthetic paleochannel model. Panels show HH and VV backscatter, co-polarized backscatter differences, HH-VV phase difference, HH and VV coherence, analytical coherence, attenuation, and layer-induced phase delay.

Monte Carlo uncertainty propagation was performed by perturbing acquisition geometry, noise characteristics, coherence, and dielectric properties. The resulting mean retrievals preserve the imposed channel geometry and remain close to the nominal solution, while uncertainty increases within the channel where dielectric and depth contrasts are strongest.

The coherence-based depth retrieval successfully reproduces the location of the buried reflector and the overall channel geometry. Additional validation diagnostics, including phase profiles, Monte Carlo statistics, and depth-retrieval uncertainty analysis, are presented in Appendix C.4.2.

4.4.2. Regional drainage network context

Figure 4.18 shows the HydroRIVERS drainage network overlaid on the BIOMASS acquisition swaths. The HydroRIVERS dataset represents a regional river network derived from the HydroSHEDS hydro-

logical database (Lehner & Grill, 2013). Within the study region, the mapped channels form a dense dendritic drainage pattern composed of numerous tributaries connected to larger drainage pathways.

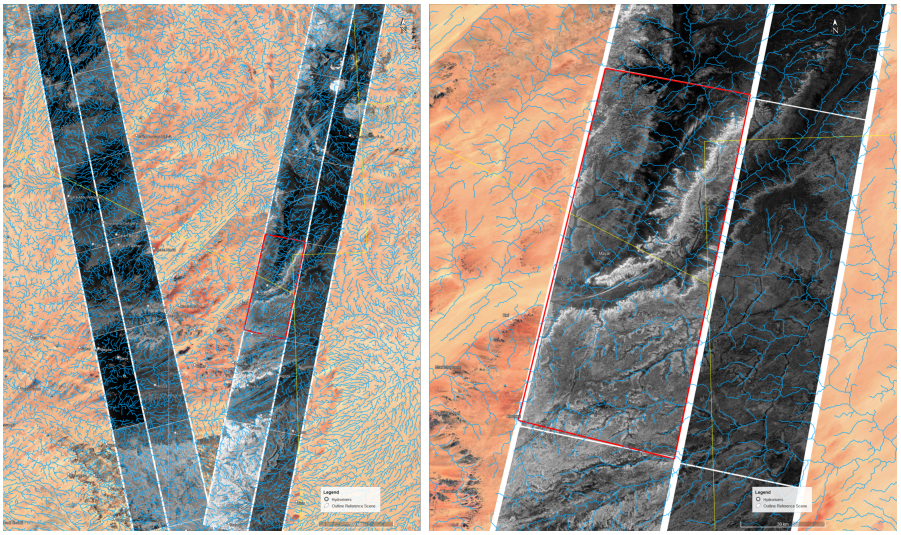

Figure 4.18: HydroRIVERS drainage network overlaid on the BIOMASS acquisition swaths. (a) Regional overview of the drainage network across the full acquisition area. Blue lines represent HydroRIVERS channels and grayscale imagery corresponds to the BIOMASS scenes. (b) Detailed view of the analysis region, outlined by the red polygon, showing the density and spatial organization of drainage pathways within the study area. HydroRIVERS data are derived from the HydroSHEDS hydrographic database (Lehner & Grill, 2013).

The detailed view of the analysis area (Figure 4.18b) shows that the selected BIOMASS scene intersects several mapped drainage channels and tributary systems. Multiple drainage pathways cross the study area and are distributed throughout the swath, indicating that the region contains a well-developed drainage network at the regional scale. To provide an independent assessment of the regional drainage configuration, a drainage network was additionally derived from the digital elevation model using a D8 flow-routing algorithm (Figure 4.19). The workflow included sink filling, flow-direction estimation, flow-accumulation calculation, and stream-network extraction using multiple accumulation thresholds. The resulting flow-accumulation map reveals a dense dendritic drainage pattern throughout the study area. Stream masks generated from accumulation thresholds of 100 and 500 pixels successfully delineate the principal drainage corridors while progressively suppressing minor tributaries.

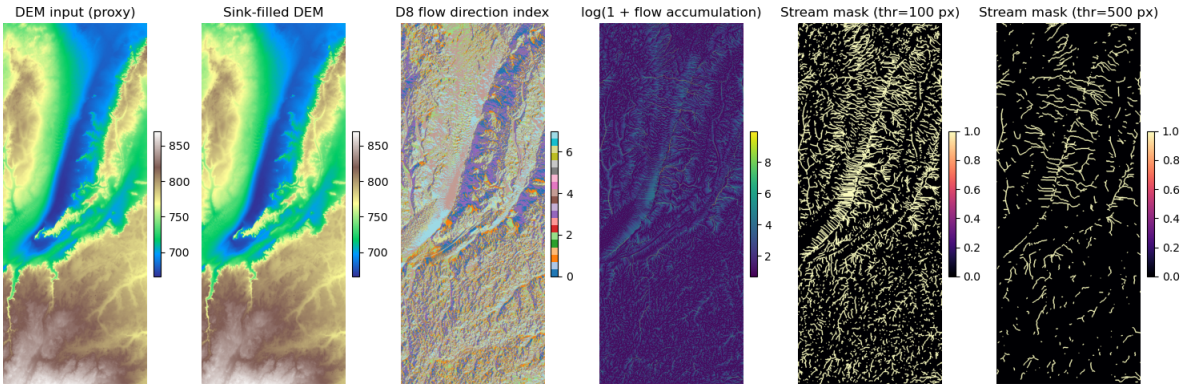

Figure 4.19: Drainage-network extraction derived from the digital elevation model using a D8 flow-routing algorithm. Panels show the DEM input, sink-filled DEM, D8 flow-direction index, logarithmically scaled flow accumulation, and stream masks derived using flow-accumulation thresholds of 100 and 500 pixels.

The drainage patterns obtained from the D8 analysis are in good agreement with the HydroRIVERS dataset. The principal drainage corridors, tributary orientations, and overall dendritic organisation

are consistently reproduced by both datasets. In particular, the main northeast-southwest trending drainage pathways identified in HydroRIVERS correspond closely with zones of elevated flow accumulation and the extracted stream network derived from the DEM. The agreement demonstrates that the principal drainage pathways identified in HydroRIVERS are also reproduced by the DEM-derived drainage network. Together, the HydroRIVERS and D8-derived drainage networks demonstrate that the study area contains extensive fluvial landform organisation at multiple spatial scales, providing an important geomorphological reference for the interpretation of candidate paleochannel features identified in the BIOMASS observations.

Sentinel-2 comparison

To provide additional spatial context for the BIOMASS-derived paleochannel detections, the coherence and phase anomalies were compared with Sentinel-2 optical imagery and several spectral indices (Figure 4.20). The Sentinel-2 RGB composite reveals a series of linear to curvilinear surface features expressed as tonal and textural variations across the scene. Similar spatial patterns are visible in the BIOMASS coherence anomaly map and the derived phase anomaly product.

Several of the prominent BIOMASS anomalies coincide with elongated features visible in the optical imagery and with regions exhibiting elevated clay-mineral index values and distinct bare-soil patterns. The coherence anomaly image highlights a network of linear features extending across the scene, many of which correspond spatially with features identified in the Sentinel-2-derived products. The phase anomaly map exhibits the same general orientations and feature continuity, although with greater spatial variability.

The combined paleochannel score integrates BIOMASS-derived coherence and phase information with Sentinel-2 indicators and topographic drainage metrics. The resulting score map enhances a series of continuous channel-like structures that are visible across multiple independent datasets. The highest scores occur along elongated curvilinear features that are also detectable in the optical imagery, clay-mineral index, and flow-accumulation products.

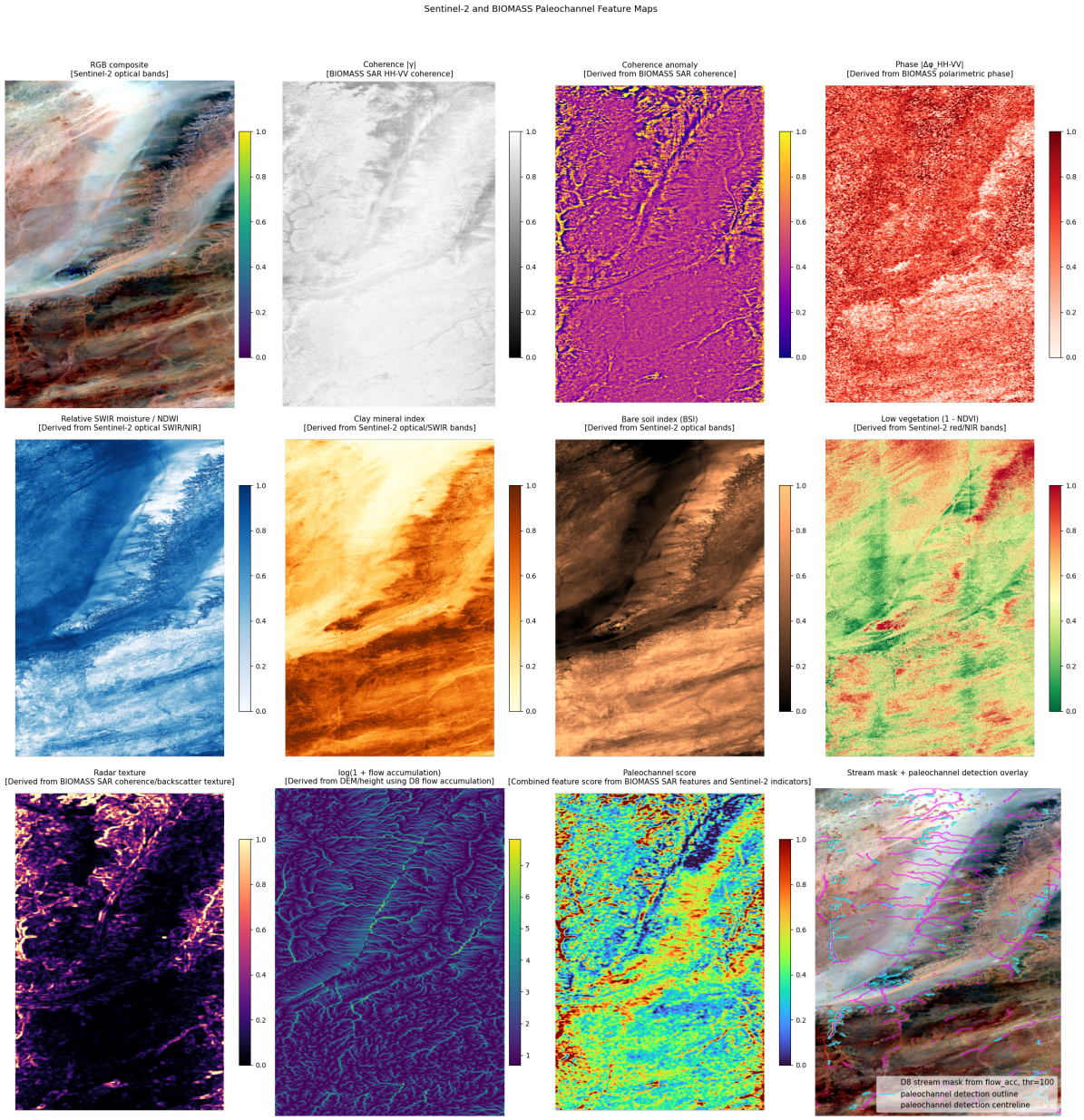

Figure 4.20: Comparison of BIOMASS-derived paleochannel indicators with Sentinel-2 optical imagery and ancillary datasets. Shown are the Sentinel-2 RGB composite, BIOMASS coherence, coherence anomaly, phase anomaly, NDWI-derived moisture indicator, clay mineral index, bare soil index, vegetation index, radar texture, flow accumulation, combined paleochannel score, and the final paleochannel detection overlay.

The final detection overlay (Figure 4.20) shows the extracted paleochannel network together with the DEM-derived stream mask. The detected features form interconnected channel-like patterns distributed throughout the study area and frequently follow the same orientations as features visible in both the Sentinel-2 imagery and the BIOMASS-derived observables.

5

Discussion

This thesis investigated the potential of spaceborne P-band SAR for detecting and characterising buried paleochannel systems in arid environments using fully polarimetric BIOMASS observations. The results demonstrate that P-band backscatter, phase difference, interferometric coherence, and derived effective-depth estimates contain spatially coherent information related to geomorphological structure. In the Sahara test scene, several elongated and dendritic features are expressed consistently across amplitude, phase-difference, polarimetric decomposition, coherence anomaly, moisture, and optical-radar fusion products. These patterns indicate that BIOMASS P-band observations are sensitive not only to surface morphology, but also to subsurface dielectric and scattering variations that may be associated with buried paleochannel systems.

5.1. Interpretation of P-band amplitude and phase signatures

The stacked BIOMASS amplitude images show that major linear and channel-like structures are visible in all polarimetric channels, with the strongest and most stable responses observed in the co-polarized HH and VV channels. Multi-temporal stacking substantially reduces speckle and improves the continuity of geomorphic features, making subtle drainage-like structures easier to interpret. This confirms that stacking is an important preprocessing step for paleochannel analysis, because many relevant features are low-contrast and can be obscured by granular noise in individual acquisitions.

The comparison between P-band, L-band, and optical imagery provides important support for the interpretation of several features as potentially subsurface-related. Some structures are visible in both L-band and P-band imagery, suggesting a surface or shallow-subsurface contribution. However, other features are more clearly expressed at P-band and are absent or only weakly visible in L-band and optical imagery. This behaviour is consistent with the longer wavelength and greater penetration capability of P-band in dry, low-loss desert sediments. Nevertheless, these observations alone do not prove that the features are buried paleochannels. Surface roughness, lithological contrasts, dune morphology, and topographic effects may also contribute to the observed backscatter patterns. Therefore, P-band amplitude anomalies should be interpreted as indicators of potentially favourable subsurface conditions rather than direct evidence of buried channels.

The HH-VV co-polarized phase difference provides complementary information to amplitude imagery. While individual wrapped phase images are difficult to interpret directly, the phase-difference product reveals spatial patterns that correspond to several geomorphological structures. This supports the use of CPD as a potentially useful observable for detecting dielectric contrasts and subsurface scattering heterogeneity. However, the profile analyses did not reveal a consistent paleochannel-specific phase signature, indicating that CPD is more effective for highlighting broader geomorphological variability than for serving as a standalone paleochannel indicator. Elevated phase differences are not unique to paleochannels and may also arise from anisotropic sedimentary structures, saline deposits, surface crusts, residual calibration effects, or local variations in scattering mechanism. The phase-difference results are therefore most robust when interpreted together with amplitude, coherence, decomposition

products, and geomorphological context.

5.2. Scattering-mechanism interpretation

The polarimetric decomposition results indicate that the radar response in the Sahara test scene is dominated mainly by surface and volume scattering, while double-bounce scattering is negligible. This result is physically reasonable for an arid, sparsely vegetated desert environment, where strong vertical structures capable of producing double-bounce interactions are largely absent. The visibility of channel-like structures in the volume-scattering component is particularly relevant, because it suggests that part of the P-band response may originate from rough, heterogeneous, or volumetrically distributed material rather than from a purely smooth surface interface.

This interpretation is consistent with the expected behaviour of buried fluvial deposits, which may contain coarse gravels, calcified pebble layers, lithological contrasts, or moisture-retaining sediments. Such materials can increase volume scattering and dielectric heterogeneity relative to surrounding aeolian sand. At the same time, the surface-scattering component also highlights several paleochannel-like features, indicating that some observed patterns may still be influenced by near-surface morphology or roughness contrasts. The decomposition results therefore support a mixed surface-subsurface interpretation rather than a purely subsurface one.

5.3. Dielectric, roughness, and effective depth retrieval

The comparison between the reduced Fresnel LUT and the I2EM LUT shows that both retrieval approaches reproduce similar large-scale spatial patterns in dielectric constant, roughness, and effective penetration depth. However, the retrieved dielectric constant and roughness values differ substantially between the two models. The Fresnel LUT generally estimates higher dielectric constants and lower roughness values, whereas the I2EM LUT retrieves higher effective roughness and lower dielectric constants. This result reflects the inherent non-uniqueness of radar backscatter inversion. Both increasing dielectric contrast and increasing surface roughness can enhance co-polarized backscatter, producing similar radiometric responses. Consequently, the individual contributions of these parameters cannot be uniquely separated without additional information, such as independent roughness measurements.

The I2EM retrieval provides a more physically based representation of rough-surface scattering than the simplified Fresnel model, because it explicitly accounts for roughness geometry, incidence angle, dielectric properties, and polarization. However, it also introduces additional assumptions, particularly the fixed correlation-length-to-RMS-height ratio. Since no field roughness measurements were available, the retrieved roughness should be interpreted as an effective roughness parameter rather than a direct estimate of physical RMS surface height. Similarly, the retrieved dielectric constant should be regarded as an effective dielectric parameter that combines the influence of moisture, lithology, salinity, porosity, and unresolved subsurface structure.

5.3.1. Consistency between observed backscatter and LUT Response

To investigate the origin of the observed LUT-boundary clustering, the distribution of the measured HH and VV backscatter was compared with the range of scattering responses represented within the I2EM lookup table at the median scene incidence angle of 25.2° (Figure 5.1). This comparison provides a useful diagnostic of whether the observed scattering behaviour is adequately represented within the retrieval parameter space.

The observed median HH and VV backscatter values are −18.96 dB and −18.61 dB, respectively, compared with simulated LUT medians of −20.36 dB and −18.70 dB. The corresponding offsets are −1.4 dB for HH and −0.1 dB for VV.

A more substantial discrepancy is observed in the co-polarized difference ($VV - HH$). The median observed polarization difference is only 0.22 dB, whereas the LUT produces a median value of 1.71 dB. Consequently, the observed distribution is systematically shifted towards lower $VV - HH$ values than predicted by the forward model. As shown in Figure 5.1, a significant fraction of the observations occupies the lower tail of the modelled polarization-ratio space, with many pixels approaching the minimum values achievable within the LUT.

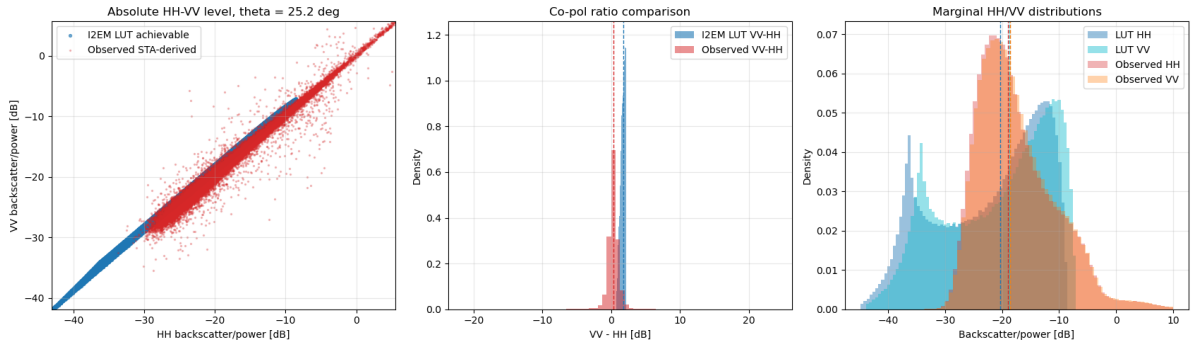

Figure 5.1: Comparison between observed STA-derived backscatter distributions and the scattering responses represented within the I2EM lookup table at the median scene incidence angle ($25.2°$). Left: HH-VV backscatter space showing observed measurements and achievable LUT responses. Centre: distribution of the co-polarization difference ($VV - HH$). Right: marginal HH and VV distributions. While the absolute HH and VV backscatter levels are reproduced reasonably well, the observed polarization difference is systematically shifted towards lower values than predicted by the LUT.

The influence of this mismatch on the inversion is illustrated in Figure 5.2.

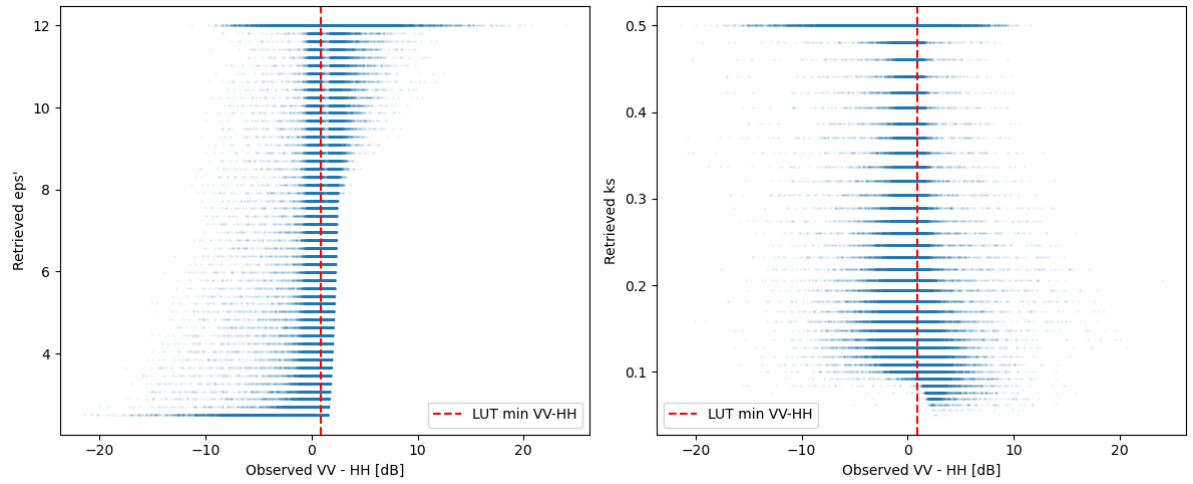

Figure 5.2: Retrieved dielectric constant (ε') and normalised roughness (k_s) as a function of the observed co-polarization difference ($VV - HH$). The red dashed line denotes the minimum polarization difference represented within the lookup table. Retrievals associated with low observed $VV - HH$ values increasingly accumulate at LUT boundaries, indicating that observations near the edge of the modelled parameter space force solutions towards the limits of the inversion domain.

Retrievals associated with low observed $VV - HH$ values exhibit clear accumulation at the dielectric and roughness boundaries of the lookup table. As the observed polarization ratio approaches the edge of the modelled parameter space, the inversion has limited freedom to further reduce the misfit and therefore selects solutions located near the LUT limits. This behaviour indicates that the boundary accumulation observed in the retrieved ε' and k_s distributions is not solely a consequence of inversion non-uniqueness, but is also linked to a mismatch between the observed polarization response and the scattering behaviour represented by the forward model.

Several factors may contribute to this discrepancy. Residual relative calibration offsets between the HH and VV channels on the order of approximately 1 dB would directly affect the polarization ratio while having only a limited impact on the absolute backscatter level. Similarly, uncertainties in the roughness parameterization, limitations in the applicability of I2EM for the study area's surface conditions, or the presence of scattering mechanisms not represented by the single-scale rough-surface model may alter the predicted polarization contrast. Because the absolute HH and VV levels agree substantially better than the $VV - HH$ difference, the retrieval appears to be more strongly limited by polarization-ratio mismatch than by insufficient backscatter magnitude coverage.

These results explain the pronounced clustering of solutions near LUT boundaries and indicate that the retrieved dielectric constant and roughness are only partially constrained by the available dual-polarized observations within the current inversion framework. This interpretation is supported by the inversion diagnostics: the Fresnel LUT generally exhibits larger cost-gap values between the best-fitting and second-best-fitting solutions, whereas the I2EM LUT frequently produces much smaller cost gaps. Consequently, a good model fit does not necessarily correspond to a unique parameter solution.

Despite the substantial differences between the dielectric-constant and roughness retrievals, the effective penetration depth estimates derived from the two forward models show strong agreement, with a very small bias and low RMSE. This indicates that the attenuation-based depth product is considerably more stable than either ε' or k_s individually. However, this agreement should not be interpreted as independent validation of the two forward models. Because both inversion frameworks use the same coherence field and d_{eff} is derived directly from coherence (Equation 3.30), the strong correlation between the depth products primarily reflects their shared coherence input. Within a scene, spatial variations in d_{eff} are therefore dominated by $-\ln|\gamma|$, while the dielectric correction contributes a comparatively smaller effect.

The retrieved effective penetration depths should not be interpreted as the physical burial depth of a discrete paleochannel reflector. Instead, they represent a coherence-derived depth scale that reflects the vertical extent over which coherent P-band scattering contributes to the interferometric response. Because coherence is influenced by additional factors including temporal decorrelation, thermal noise, surface roughness, and spatial heterogeneity, the retrieved depths are best interpreted as relative indicators of penetration potential rather than direct measurements of subsurface depth.

5.3.2. Full swath effective depth inversion

The full-swath depth inversion further demonstrates that the retrieval framework can be applied beyond individual test scenes to regional-scale BIOMASS coverage. In the Kufrah Basin, the dielectric constant, dielectric-equivalent moisture, and effective penetration depth products show coherent spatial patterns across multiple adjacent frames. Large parts of the desert background are characterised by low dielectric constants, low moisture-equivalent values, and effective penetration depths of several metres, whereas linear and branching paleodrainage features generally correspond to elevated dielectric and moisture-equivalent values and reduced effective penetration depth. This pattern is physically consistent with the expected reduction in electromagnetic penetration in materials with higher dielectric losses or moisture content, but it should still be interpreted cautiously because lithology, salinity, compaction, and roughness may produce similar dielectric contrasts. The observed reduction in effective penetration depth over many paleodrainage features likely reflects a combination of increased dielectric contrast, enhanced scattering heterogeneity, and stronger volumetric decorrelation relative to the surrounding aeolian sands. Paleochannel fills may contain mixtures of coarse alluvium, compacted sediments, moisture-retaining materials, evaporitic deposits, or buried lithological interfaces, all of which can modify the vertical distribution of coherent scattering. In this interpretation, reduced effective depth does not necessarily imply shallower burial of the channel itself. Rather, it indicates a reduction in the vertical extent over which coherent scattering contributes to the interferometric response, resulting in smaller coherence-derived depth estimates.

The regional Namib Desert retrieval provides an important comparison because the observed patterns differ from those in the Kufrah Basin. Instead of being dominated by dendritic paleodrainage networks, the Namib full-swath product shows strong spatial variability associated with dune fields, interdune corridors, drainage systems, and exposed bedrock terrain. The larger effective penetration depths occur mainly over broad, dry, relatively homogeneous sandy surfaces, whereas reduced depths are more common in geomorphologically complex areas. This contrast between the Kufrah and Namib results suggests that the effective-depth product is sensitive not only to potential buried fluvial structures, but also to broader surface and near-surface geomorphological controls.

An additional factor that may contribute to the weaker expression of paleochannel features in the Namib dielectric retrievals is the difference in spatial resolution between the BIOMASS and ALOS-2 observations. Using high-resolution ALOS-2 PALSAR-2 imagery with a ground resolution of approximately 3 m, Paillou et al. (2020) successfully mapped individual paleochannels preserved within interdune valleys south of the present-day Kuiseb River. In contrast, the BIOMASS Level-1C STA products used in this

study have a native pixel spacing of approximately 19.8 m in slant range and 6.7 m in azimuth, corresponding to a ground-range spacing of roughly 35–50 m across-track and 6–7 m along-track depending on incidence angle, with a spatial resolution of approximately 23 m $\times$ 8 m. Consequently, many of the narrow interdune paleochannels identified by Paillou et al. (2020) are unlikely to be fully resolved in the BIOMASS observations and may occupy only a limited number of resolution cells. Their radar response is therefore mixed with that of the surrounding dune sediments, reducing the dielectric and scattering contrast available for detection. This resolution mismatch likely contributes to the reduced visibility of some Namib paleochannel features in the regional BIOMASS dielectric retrievals compared with the higher-resolution ALOS-2 results.

These regional results strengthen the interpretation of the effective-depth product as a map of penetration potential and scattering-volume complexity rather than as a direct burial-depth product. The consistency of large-scale structures across multiple BIOMASS frames is encouraging, because it indicates that the retrieval is able to preserve regional geomorphological organization. However, the presence of discontinuities at scene boundaries and differences between neighbouring acquisitions also shows that the products remain affected by acquisition geometry, radiometric variability, coherence quality, and mosaicking artefacts. Therefore, full-swath depth maps are most useful for identifying spatially coherent candidate zones for further analysis, rather than for assigning absolute subsurface depths.

5.3.3. Influence of perpendicular baseline on effective penetration depth retrieval

An additional source of variability in the effective penetration depth retrieval arises from the selection of interferometric baseline pairs. To assess this effect, all available baseline combinations within multiple BIOMASS Level-1C stacks were processed independently while keeping the radiometric observations unchanged. Differences between retrievals therefore primarily reflect the influence of interferometric geometry rather than variations in surface properties.

Figure 5.3a shows the relationship between the absolute perpendicular baseline magnitude and the median retrieved effective penetration depth for all analysed scene pairs. Retrievals derived from the smallest available baselines consistently produce substantially larger effective penetration depth estimates than retrievals obtained from intermediate and large baselines. In contrast, retrievals associated with baselines larger than approximately 1500 m tend to converge towards similar depth values, suggesting reduced sensitivity to further increases in baseline magnitude. This behaviour indicates that the effective penetration depth retrieval is sensitive to baseline selection and that depth estimates derived from different baseline configurations are not strictly interchangeable.

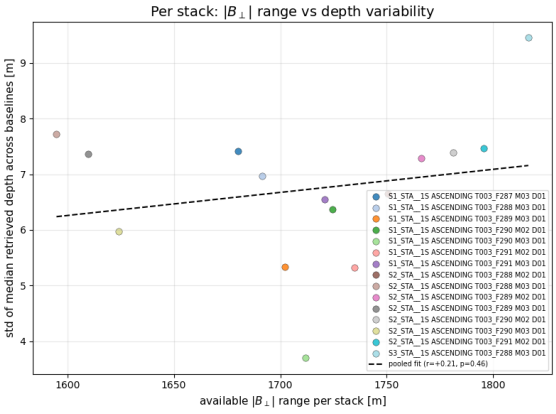

(a) Relationship between absolute perpendicular baseline magnitude and median retrieved effective penetration depth for all analysed scene pairs.

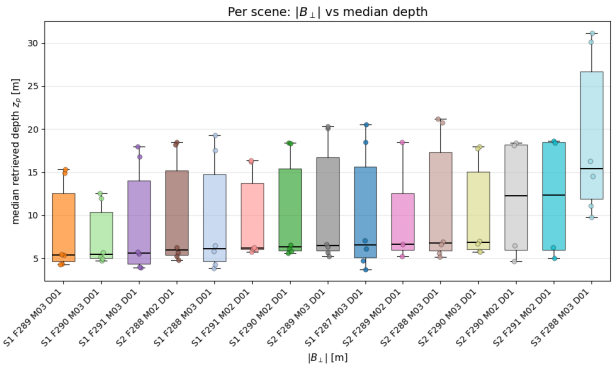

(b) Distribution of median effective penetration depths obtained from all available baseline pairings within each BIOMASS stack.

Figure 5.3: Influence of perpendicular baseline selection on retrieved effective penetration depth. (a) Relationship between absolute perpendicular baseline magnitude and median retrieved effective penetration depth for all analysed scene pairs. Colours indicate different BIOMASS stacks and the dashed line shows the pooled linear regression. (b) Distribution of median retrieved effective penetration depths obtained from all available baseline pairings within each BIOMASS stack. Boxes indicate the interquartile range, horizontal lines indicate the median, and individual points correspond to retrievals derived from different baseline pairs.

The influence of baseline selection is also apparent when the retrieval variability is analysed on a stack-by-stack basis. Figure 5.3b shows the distribution of median effective penetration depth estimates obtained from all available baseline combinations within each stack. Some stacks exhibit relatively limited variation between baselines, whereas others show a substantially larger spread. Across most stacks, retrievals derived from baseline pairs of approximately ± 1500–2500 m show a high degree of mutual agreement, whereas retrievals derived from the ± 700–800 m baseline pairs systematically deviate towards larger depth values. The magnitude of the baseline effect therefore differs between swaths and acquisition geometries, but the largest deviations are consistently associated with the smallest baselines.

A representative example is shown in Figure 5.4. Within a single acquisition stack, the retrieved median effective penetration depth varies systematically as different baseline pairs are used. The magnitude of the variation is comparable to or larger than the differences observed between some stacks, demonstrating that baseline selection itself can represent a significant source of retrieval variability.

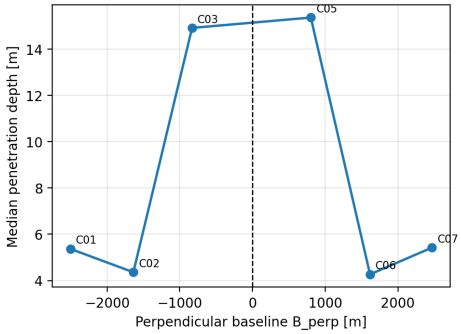

Figure 5.4: Example of baseline-dependent effective penetration depth retrievals for a single BIOMASS stack. Different baseline pairs produce systematically different median effective penetration depth estimates despite originating from the same acquisition stack.

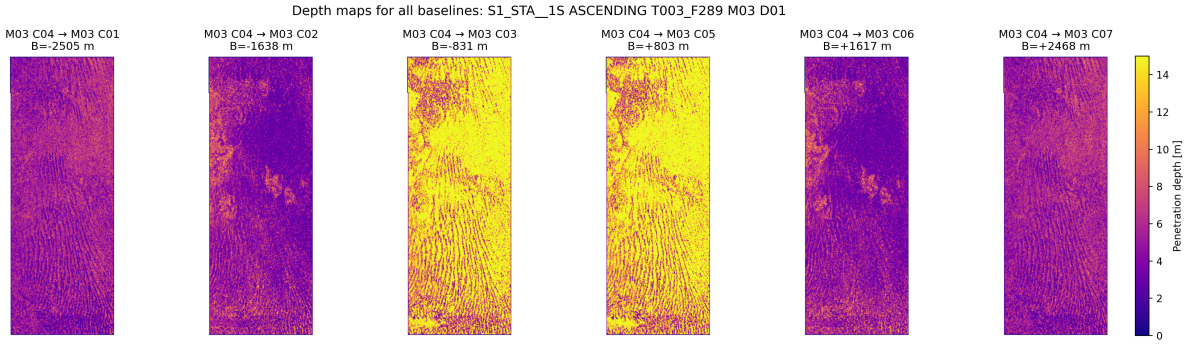

Figure 5.5: Retrieved effective penetration depth maps for all available baseline pairs within the representative BIOMASS stack shown in Figure 5.4. The spatial distribution of the effective penetration depth anomalies remains largely consistent, whereas the absolute depth magnitude varies with baseline selection.

The depth-map comparison further shows that baseline selection primarily affects the magnitude of the retrieved effective penetration depth rather than the spatial distribution of the anomalies. As illustrated in Figure 5.5, the principal paleochannel-related features remain identifiable across the full range of evaluated baselines, while the absolute depth values vary substantially between baseline pairs. This persistence of the main anomaly patterns suggests that the depth product is most robust when interpreted in terms of relative spatial variations in penetration potential and subsurface heterogeneity rather than absolute depth values.

Several mechanisms may contribute to the observed behaviour. For very small perpendicular baselines, the interferometric sensitivity to vertical structure is reduced. Consequently, uncertainties in the

coherence-derived observables can produce relatively large changes in the inferred effective penetration depth. As the perpendicular baseline increases, the retrieval appears to become better conditioned, resulting in more stable depth estimates. This interpretation is supported by the observed convergence of the intermediate- and large-baseline retrievals, which yield similar effective penetration depth distributions despite substantial differences in baseline magnitude. Nevertheless, larger baselines may also be affected by increased spatial decorrelation, meaning that both effects are likely contributing to the observed behaviour. Because the retrieval framework relies on coherence-derived observables, variations in coherence may reflect both subsurface scattering processes and baseline-dependent decorrelation effects, which cannot be fully separated within the current framework.

The baseline-sensitivity analysis informed the baseline-selection strategy adopted throughout this study. For the detailed single-scene retrievals, the interferometric pair with the highest mean coherence was selected to maximise retrieval quality. In contrast, the regional-scale inversions were performed using the pair whose perpendicular baseline was closest to 2500 m. Intermediate- and large-baseline solutions exhibited similar effective penetration depth distributions and spatial patterns, supporting their use for regional-scale mapping.

5.3.4. Influence of acquisition geometry

The comparison between ascending and descending BIOMASS acquisitions provides insight into the robustness of the retrieval framework under different observation conditions. However, the two acquisitions should not be interpreted as direct repeat observations of the same scene. The datasets originate from different BIOMASS sub-swaths (S1 and S3), different tracks and frames, and are separated by approximately two months. Furthermore, the mean incidence angle differs by approximately 6.4° (25.3° versus 31.7°), producing an approximately 23% difference in the surface vertical wavenumber before any dielectric correction is applied.

Despite these differences, several large-scale structures remain visible in both retrievals. Elongated depth anomalies, dielectric features, and moisture-related patterns occur in broadly similar locations within the region of overlap. The persistence of these structures across independent acquisitions suggests that part of the observed signal is controlled by stable surface or subsurface characteristics rather than acquisition-specific artefacts.

At the same time, substantial pixel-scale differences are observed between the two retrievals. The dielectric and moisture products show considerably greater variability than the effective penetration depth estimates, indicating that intermediate inversion products remain sensitive to viewing geometry and inversion non-uniqueness. Differences are expected because both the dielectric retrieval and the coherence- based depth inversion depend explicitly on incidence angle, coherence, backscatter magnitude, and vertical wavenumber.

The coherence characteristics also differ between the acquisitions, with mean coherence increasing from 0.551 in the ascending acquisition to 0.670 in the descending acquisition. Since coherence enters directly into the depth inversion, differences in coherence quality propagate into the retrieved effective penetration depths. Consequently, exact numerical agreement between the two acquisitions should not be expected.

Taken together, the ascending-descending comparison suggests that the retrieval framework is more reliable for identifying relative spatial anomalies than for estimating absolute physical parameter values. While pixel-scale agreement is limited by differences in viewing geometry, coherence magnitude, incidence angle, and inversion conditioning, many of the broad geomorphological structures remain persistent across independent acquisitions. The strongest consistency therefore lies in the spatial organisation of the retrieved anomalies rather than in their exact numerical values.

5.3.5. Moisture interpretation

The dielectric-to-moisture conversion provides a useful way to express retrieved dielectric variations in a more intuitive physical form. Both retrieval models indicate generally low volumetric moisture contents, consistent with the hyperarid character of the study area. Elevated moisture-equivalent values occur preferentially along channel-like features and drainage corridors. This spatial pattern is consistent with the possibility that paleochannel fills or associated fine-grained sediments retain slightly higher moisture

or possess dielectric properties that resemble wetter material.

However, the moisture maps should not be interpreted as direct measurements of soil moisture. The conversion from dielectric constant to volumetric moisture assumes that dielectric variability is primarily controlled by water content, whereas in arid environments dielectric contrasts may also arise from salinity, mineralogy, compaction, grain-size differences, calcified deposits, or buried lithological interfaces. The similarity between the Dobson, CRIM, and Topp moisture patterns indicates that the spatial distribution is mainly controlled by the retrieved dielectric field rather than by the choice of dielectric mixing model. Consequently, the moisture products are most appropriately described as dielectric-equivalent moisture estimates.

5.4. Forward-model validation and uncertainty

The synthetic paleochannel model provides an important controlled test of the proposed interpretation framework. Because the buried channel geometry, dielectric contrast, roughness, and reflector depth are prescribed, the forward model allows the expected BIOMASS observables to be evaluated under known conditions. The synthetic results show that a buried calcified pebble-gravel channel can generate coherent anomalies in HH and VV backscatter, co-polarized backscatter difference, HH-VV phase difference, and interferometric coherence. The strongest correspondence with the prescribed channel geometry is observed in the phase-difference and coherence-related observables, supporting their use as complementary indicators of buried structure.

The Monte Carlo analysis shows that the imposed channel geometry remains recoverable under realistic perturbations of acquisition and environmental parameters. The retrieved mean fields preserve the meandering channel shape, while uncertainty increases within the channel where dielectric and depth contrasts are strongest. This behaviour is expected, because the same contrasts that make the channel detectable also increase sensitivity to assumptions about dielectric properties, roughness, and acquisition geometry. The coherence-derived depth retrieval reproduces the location of the prescribed buried reflector in the synthetic case, but the uncertainty envelope broadens with increasing depth. This confirms that deeper or more weakly coherent reflectors are more difficult to retrieve reliably.

It should be noted that the synthetic paleochannel is prescribed both a buried dielectric contrast and reduced temporal coherence ($\gamma_{\mathrm{temp,ch}} = 0.72$ compared with $\gamma_{\mathrm{temp,bg}} = 0.92$). Because d_{eff} is a monotonic function of coherence magnitude, part of the observed depth anomaly is therefore inherent to the model configuration. Consequently, the synthetic experiments should be interpreted primarily as tests of the internal consistency and sensitivity of the retrieval framework rather than as independent validation of the coherence-depth relationship.

The synthetic coherence formulation is internally related to the inversion framework, and the simulated scene is deliberately simplified relative to natural desert environments. The model therefore evaluates physical plausibility and sensitivity to key parameters rather than providing an independent assessment of retrieval accuracy.

5.5. External validation and geomorphological consistency

The integration of Sentinel-2 indicators, D8 flow accumulation, HydroRIVERS drainage data, and BIOMASS-derived features provides useful geomorphological context for interpreting candidate paleochannel detections. The D8 analysis identifies a dense drainage network and a dominant northeast-southwest oriented drainage corridor, while the fused optical-radar paleochannel score highlights several broader linear anomalies. Some detections overlap with or occur adjacent to topographically inferred drainage pathways, supporting their interpretation as fluvial or paleofluvial features.

However, the agreement between SAR-derived detections and drainage datasets is only partial. This is not necessarily a weakness. Buried paleochannels may be decoupled from present-day topography due to aeolian burial, erosion, dune migration, or landscape reorganisation. Conversely, modern drainage pathways may not correspond to older buried systems. Optical data also cannot directly observe buried channels, but only surface expressions such as moisture anomalies, mineralogical contrasts, bare soil exposure, or geomorphic texture. Therefore, the external validation datasets should be treated as supporting evidence rather than definitive ground truth.

The lack of direct subsurface validation remains one of the main limitations of this thesis. Without GPR profiles, borehole data, field sediment observations, or independent geophysical surveys over the same BIOMASS scenes, it is not possible to conclusively confirm the depth, composition, or continuity of the detected paleochannel candidates. The current validation is therefore based on internal consistency between radar observables, synthetic modelling, and geomorphological plausibility.

5.6. Limitations of the methodology

Several limitations affect the interpretation of the results. First, the backscatter inversion is underconstrained because dielectric constant and surface roughness have partially overlapping effects on co-polarized backscatter. The use of HH and VV together reduces this ambiguity but does not eliminate it. Independent roughness information would be required to retrieve dielectric properties more robustly.

Second, the coherence-derived depth inversion relies on a simplified exponential decorrelation model. This model provides a physically interpretable effective-depth scale, but it does not explicitly separate volume decorrelation from temporal decorrelation, thermal noise, surface scattering, or geometric effects. As a result, the retrieved depth may overestimate or underestimate the true depth of subsurface scattering depending on the dominant decorrelation mechanism. The full-swath retrievals introduce an additional limitation related to regional mosaicking. Because the products combine multiple BIOMASS frames and acquisitions, differences in incidence angle, coherence quality, baseline, radiometric calibration, and acquisition conditions can produce discontinuities at frame boundaries. These artefacts are visible in the regional maps and may locally affect the retrieved dielectric, moisture-equivalent, and depth values. Consequently, interpretation should focus primarily on spatially coherent patterns that persist over large areas, rather than on abrupt pixel-scale or scene-edge variations.

Third, the dielectric correction of the vertical wavenumber assumes low-loss propagation and uses the real part of the retrieved permittivity. This is appropriate as a first-order approximation for dry, low-loss media, but may become less valid in areas with elevated moisture, salinity, or conductive sediments. In such cases, attenuation and complex propagation effects may significantly influence both coherence and phase behaviour.

Fourth, the I2EM inversion requires an assumed relationship between RMS height and correlation length. Although the sensitivity analysis shows that the adopted ratio provides a stable compromise within the tested parameter space, it remains an assumption rather than an independently validated terrain property. The resulting roughness and dielectric estimates should therefore be interpreted as model-dependent effective parameters.

Finally, the study is limited by the absence of direct ground truth. The detected features are plausible paleochannel candidates, but their interpretation remains probabilistic. The strongest results are therefore those based on convergence between multiple independent indicators, including P-band visibility, coherence behaviour, decomposition response, moisture-equivalent dielectric anomalies, drainage alignment, and optical-radar fusion. CPD provides supporting geomorphological context but did not exhibit a unique or reproducible paleochannel signature in the analysed BIOMASS observations.

5.7. Implications for BIOMASS paleochannel studies

Despite these limitations, the results demonstrate that BIOMASS P-band SAR has considerable potential for subsurface geomorphological investigations in arid environments. The ability of P-band observations to reveal features that are weakly expressed or absent in optical and L-band imagery suggests that the mission can provide complementary information on buried drainage systems and other subsurface features.

The full-swath applications over the Kufrah Basin and Namib Desert show that the proposed workflow can be scaled from local scene-based analysis to regional mapping. The persistence of several drainage-related patterns across multiple BIOMASS frames indicates that P-band observations can support the identification of large-scale paleodrainage networks extending beyond a single acquisition frame.

At the same time, the regional products highlight the need for careful interpretation. Effective penetration depth is influenced by coherence, dielectric properties, acquisition geometry, and surface hetero-

geneity, and should therefore not be interpreted as a direct measurement of burial depth. Instead, the greatest value of the proposed framework lies in the identification of spatially coherent anomalies and candidate zones where subsurface scattering is physically plausible.

Overall, the results suggest that BIOMASS is particularly well suited as a regional screening and interpretation tool. The integration of amplitude, coherence, polarimetric decomposition, dielectric retrievals, and geomorphological context provides a more robust basis for paleochannel detection than any individual observable alone.

5.8. Future research directions

The results of this study demonstrate the potential of BIOMASS P-band SAR for identifying subsurface features consistent with buried paleochannel systems. However, several opportunities exist to further improve the physical interpretation, validation, and retrieval capability of the proposed methodology.

The most important priority is the acquisition of independent validation data. The current analysis relies primarily on internal consistency between radar observables, synthetic modelling, and geomorphological evidence. Future studies should integrate ground-penetrating radar surveys, borehole observations, trenching, or other geophysical datasets acquired within BIOMASS study areas. Such measurements would provide direct constraints on buried channel geometry, sediment properties, and burial depth, allowing the retrieval framework to be quantitatively validated rather than assessed through indirect evidence alone.

A second area for improvement is the characterisation of surface roughness. The present workflow relies on a roughness proxy and an assumed correlation-length parameterization, both of which contribute to uncertainty in the dielectric retrieval. Field measurements of RMS roughness and correlation length would reduce the dielectric-roughness ambiguity and provide a more rigorous basis for calibration of both the simplified LUT inversion and the I2EM retrieval framework.

Future developments could also make greater use of the fully polarimetric capabilities of BIOMASS. The decomposition results indicate that several candidate paleochannel features are associated with enhanced volume-scattering signatures. Polarimetric-interferometric approaches may therefore provide additional constraints on the relative contributions of surface, volume, and subsurface scattering mechanisms. Such techniques could help reduce retrieval non-uniqueness and improve discrimination between paleochannel-related signatures and other geomorphological features.

Another promising direction is the use of multi-baseline observations and tomographic processing. The present study estimates effective penetration depth indirectly from interferometric coherence. Future tomographic or polarimetric-interferometric analyses could investigate the vertical distribution of scattering more directly, potentially allowing shallow surface scattering, distributed subsurface scattering, and discrete buried reflectors to be separated. Such approaches would provide a stronger physical basis for subsurface characterisation than single-baseline coherence analysis alone.

Further refinement of the electromagnetic modelling framework may also improve retrieval performance. Multi-layer dielectric models, spatially variable attenuation, salinity-dependent dielectric behaviour, and Bayesian uncertainty propagation could provide a more realistic representation of natural desert environments. Incorporating these processes may help better quantify uncertainty and improve the physical interpretation of retrieved parameters.

Several alternative retrieval frameworks were investigated during the development of this thesis but were ultimately not adopted in the final workflow owing to limited calibration data, insufficient physical constraints, or uncertainty in model parameterization. These included empirical moisture-retrieval approaches, physically based dielectric inversion frameworks, and decomposition-constrained coherence inversions. Although excluded from the operational methodology, they remain promising directions for future research and are documented in Appendix D.

Finally, future studies should evaluate the transferability of the proposed methodology across different arid environments. The present work focused primarily on a representative Sahara test scene. Application to additional BIOMASS acquisitions over the Sahara, Namib Desert, Arabian Peninsula, and other hyperarid regions would allow the robustness of the workflow to be assessed under varying ge-

ological, geomorphological, and climatic conditions. Such analyses would help determine whether the observed relationships between coherence, phase difference, dielectric properties, and paleochannel occurrence remain consistent across a broader range of desert settings.

Overall, the methodology developed in this thesis provides a foundation for future BIOMASS-based paleochannel investigations. Continued integration of field observations, advanced polarimetric and interferometric techniques, improved electromagnetic models, and independent validation datasets will be essential for transforming the current penetration-potential framework into a quantitatively validated subsurface retrieval methodology.

6

Conclusion

This thesis assessed the capability of BIOMASS P-band SAR for detecting and characterising buried paleochannel systems in arid environments. A semi-physical workflow was developed that combines polarimetric amplitude and phase analysis, co-polarized dielectric-roughness inversion, dielectric-equivalent moisture estimation, interferometric coherence, and effective penetration depth retrieval. The method was evaluated using BIOMASS observations over arid paleochannel study areas, supported by synthetic forward modelling, Monte Carlo uncertainty analysis, Sentinel-2 optical indicators, and DEM-based drainage modelling.

The first research question asked how dielectric contrast, reflection depth, and surface roughness influence the sensitivity of copolarized phase difference (CPD) and interferometric coherence to buried paleochannel structure. The results show that CPD and coherence are sensitive to buried dielectric and scattering contrasts under favourable dry, low-loss conditions. Synthetic modelling further demonstrated that this sensitivity is greatest for strong dielectric contrasts and relatively homogeneous surface conditions, whereas increased surface roughness, attenuation, and decorrelation progressively reduce the detectability of buried structures. In the synthetic Bir Safsaf-inspired model, a buried calcified pebble-gravel channel generates coherent anomalies in HH-VV phase difference, backscatter, and coherence, and the imposed channel geometry remains visible under Monte Carlo perturbations. In the BIOMASS observations, several channel-like structures are expressed consistently in amplitude, CPD, coherence anomaly, polarimetric decomposition, and optical-radar fusion products. However, these observables are not uniquely diagnostic of paleochannels and must be interpreted together with geomorphological context and ancillary datasets.

The second research question asked whether physically interpretable estimates of effective penetration depth can be derived from spaceborne P-band SAR observations in the absence of direct subsurface validation data. The framework developed to address this combines Fresnel- and I2EM-based backscatter modelling, dielectric mixing relationships, and a coherence-derived vertical wavenumber. The developed workflow provides spatially coherent dielectric, roughness, moisture-equivalent, and effective-depth products. The Fresnel and I2EM LUTs produce different dielectric and roughness estimates, reflecting the inherent non-uniqueness of backscatter inversion. A comparison between partially overlapping ascending and descending BIOMASS acquisitions further showed that broad spatial effective penetration depth patterns remain identifiable under different acquisition geometries, although absolute parameter values are sensitive to viewing geometry, incidence angle, and coherence variations. The effective penetration depth estimates nevertheless agree substantially more closely between models than the intermediate dielectric and roughness retrievals, exhibiting negligible bias and a strong pixel-wise correlation ($r = 0.924$). However, the RMSE of 1.61 m remains a significant fraction of the retrieved depth range, indicating that the two models reproduce similar spatial patterns rather than identical pixel-wise depth values. The retrieved depths should be interpreted as effective coherence-derived depth scales that describe the vertical extent of coherent scattering contributions rather than the physical burial depth of a reflector. Application to full-swath BIOMASS coverage over both the Kufrah Basin and the Namib Desert showed that these products preserve coherent regional-scale geomorpho-

logical patterns over hundreds of kilometres. In the Kufrah Basin, reduced effective penetration depths occur mainly along dielectric and moisture-equivalent anomalies associated with paleodrainage-like networks, while larger effective penetration depths are retrieved over broad, dry, homogeneous desert surfaces. In the Namib Desert, the effective penetration depth product captures strong contrasts between dune fields, drainage systems, and more heterogeneous bedrock-influenced terrain.

The third research question addressed the sensitivity of CPD, coherence, and effective-depth estimates to uncertainty in soil moisture and surface roughness. The results show that uncertainty is largest where dielectric contrasts and depth variations are strongest. Surface roughness and correlation-length assumptions influence the dielectric-roughness inversion, while coherence-derived depth is sensitive to decorrelation processes that are not exclusively related to subsurface scattering. Moisture-equivalent retrievals remain useful for identifying relative dielectric anomalies, but cannot be treated as direct soil-moisture measurements because salinity, lithology, compaction, and mineralogy may produce similar dielectric effects.

Overall, the thesis demonstrates that BIOMASS P-band SAR provides a promising new capability for paleochannel studies in arid environments. This study constitutes the first application of fully polarimetric spaceborne BIOMASS observations to paleochannel detection and characterisation, including the development of a coherence-derived effective depth retrieval framework. P-band imagery reveals geomorphological features that are partly absent in L-band and optical observations, while the combination of amplitude, phase difference, polarimetric decomposition, coherence, and effective-depth indicators provides a physically meaningful basis for identifying candidate buried channels.

The principal limitation remains the absence of direct subsurface validation. Without coincident GPR, borehole, or field measurements, the detected features cannot be conclusively confirmed as buried paleochannels, nor can the retrieved effective depths be converted into true geological layer depths. Consequently, the results should be interpreted as physically plausible indicators of subsurface structure rather than definitive subsurface maps.

The main contribution of this thesis is therefore not the retrieval of true paleochannel burial depth, but the development of an integrated interpretation framework that combines amplitude, coherence, dielectric, polarimetric, and geomorphological information to identify and prioritise candidate paleochannel systems at regional scale. Despite the non-uniqueness of the dielectric and roughness retrievals, the persistence of the principal paleodrainage patterns across forward models, acquisition geometries, and baseline configurations suggests that the observed anomalies reflect genuine spatial variations in bulk electromagnetic properties rather than retrieval artefacts.

The results demonstrate that BIOMASS P-band SAR contains measurable information related to subsurface geomorphological structure at regional scale. The observation that major paleodrainage systems remain detectable as coherent dielectric and effective penetration depth anomalies across hundreds of kilometres suggests that BIOMASS may provide a unique capability for reconstructing paleohydrological systems in hyperarid environments, extending previous studies based primarily on airborne radar and L-band observations.

Future work should focus on validation and refinement of the retrieval framework. Priority should be given to acquiring independent roughness measurements, field dielectric data, GPR profiles, or other geophysical observations over BIOMASS-covered paleochannel systems. Multi-baseline or tomographic BIOMASS analyses could further improve the separation of surface and subsurface scattering contributions. In addition, future polarimetric-interferometric approaches could use decomposition products to constrain the relative contributions of surface, volume, and subsurface scattering. With such developments, BIOMASS P-band SAR may become a powerful tool for mapping buried drainage systems, reconstructing paleohydrological networks, and improving understanding of landscape evolution in arid and hyperarid regions.

References

Abdelkareem, M., Gaber, A., Abdalla, F., & El-Din, G. K. (2020). Use of optical and radar remote sensing satellites for identifying and monitoring active/inactive landforms in the driest desert in saudi arabia. *Geomorphology*, *362*, 107197. https://doi.org/10.1016/j.geomorph.2020.107197

Alemohammad, S. H., Konings, A. G., Jagdhuber, T., Moghaddam, M., & Entekhabi, D. (2018). Characterization of vegetation and soil scattering mechanisms across different biomes using p-band sar polarimetry [Research conducted under the NASA AirMOSS mission; data collected 2013-2015]. *Remote Sensing of Environment*, *209*, 107–117. https://doi.org/10.1016/j.rse.2018.02.032

Aresys]. (2025). *BPS L1 STACK ATBD - algorithms theoretical baseline document* (Algorithm Theoretical Baseline Document No. BIO-BPS-L1-STACK-ATBD-ARE-010166) (Issue 1.3.1). Aresys S.r.l. / ESA.

Baghdadi, N., Holah, N., & Zribi, M. (2006). Calibration of the integral equation model for sar data in c-band and hh and vv polarizations. *International Journal of Remote Sensing*, *27*(4), 805–816. https://doi.org/10.1080/01431160500212278

Bamler, R., & Hartl, P. (1998). Synthetic aperture radar interferometry. *Inverse Problems*, *14*(4), R1–R54. https://doi.org/10.1088/0266-5611/14/4/001

Bekaert, D., Gebert, N., Lin, C.-C., Hélière, F., Dall, J., Kusk, A., & Kristensen, S. S. (2014). Multichannel surface clutter suppression: East antarctica p-band sar ice sounding in the presence of grating lobes [POLARIS instrument campaign analysis]. *Annals of Glaciology*, *55*(67), 9–21. https://doi.org/10.3189/2014AoG67A100

Born, M., & Wolf, E. (1999). *Principles of optics: Electromagnetic theory of propagation, interference and diffraction of light* (7th). Cambridge University Press.

Campbell, B. A., & Shepard, M. K. (1996). Lava flow surface roughness and depolarized radar scattering. *Journal of Geophysical Research*, *101*(E8), 18941–18951. https://doi.org/10.1029/95JE01804

Chen, K.-S., Wu, T.-D., Tsay, M.-K., & Fung, A. K. (2000). A note on the multiple scattering in an IEM model. *IEEE Transactions on Geoscience and Remote Sensing*, *38*(1), 249–256. https://doi.org/10.1109/36.823917

Chen, W., Liu, L., Zhang, C., & Wang, J. (2004). Monitoring the seasonal bare soil areas in beijing using multitemporal tm images. *Proceedings of the IEEE International Geoscience and Remote Sensing Symposium*, 3379–3382. https://doi.org/10.1109/IGARSS.2004.1370429

Choker, M., Baghdadi, N., Zribi, M., El Hajj, M., Paloscia, S., Verhoest, N. E. C., Lievens, H., & Mattia, F. (2017). Evaluation of the Oh, Dubois and IEM backscatter models using a large dataset of SAR data and experimental soil measurements. *Water*, *9*(1), 38. https://doi.org/10.3390/w9010038

Cloude, S. R., & Papathanassiou, K. P. (1998). Polarimetric SAR interferometry. *IEEE Transactions on Geoscience and Remote Sensing*, *36*(5), 1551–1565. https://doi.org/10.1109/36.718859

Cloude, S. R., & Papathanassiou, K. P. (2003). Three-stage inversion process for polarimetric SAR interferometry. *IEE Proceedings - Radar, Sonar and Navigation*, *150*(3), 125–134. https://doi.org/10.1049/ip-rsn:20030449

Cloude, S. R., & Pottier, E. (1997). An entropy-based classification scheme for land applications of polarimetric SAR. *IEEE Transactions on Geoscience and Remote Sensing*, *35*(1), 68–78. https://doi.org/10.1109/36.551935

Daniels, J., Blumberg, D. G., Vulfson, L. D., Kotlyar, A. L., Freiliker, V., Ronen, G., & Ben-Asher, J. (2003). Microwave remote sensing of physically buried objects in the negev desert: Implications for environmental research. *Remote Sensing of Environment*, *86*(2), 243–256. https://doi.org/10.1016/S0034-4257(03)00111-1

Dobson, M. C., Ulaby, F. T., Hallikainen, M. T., & El-Rayes, M. A. (1985). Microwave dielectric behavior of wet soil-part II: Dielectric mixing models. *IEEE Transactions on Geoscience and Remote Sensing*, *GE-23*(1), 35–46. https://doi.org/10.1109/TGRS.1985.289498

Drusch, M., Del Bello, U., Carlier, S., Colin, O., Fernandez, V., Gascon, F., Hoersch, B., Isola, C., Laberinti, P., Martimort, P., Meygret, A., Spoto, F., Sy, O., Marchese, F., & Bargellini, P. (2012). Sentinel-2: Esa's optical high-resolution mission for gmes operational services. *Remote Sensing of Environment*, *120*, 25–36. https://doi.org/10.1016/j.rse.2011.11.026

Elsherbini, A., & Sarabandi, K. (2010). Mapping of sand layer thickness in deserts using SAR interferometry. *IEEE Transactions on Geoscience and Remote Sensing*, *48*(9), 3550–3559. https://doi.org/10.1109/TGRS.2010.2047110

European Space Agency (ESA). (2025). *BioPAL Data Readers* [GitHub repository containing BIOMASS data readers and quick-look processing utilities, accessed July 2026]. https://github.com/BioPAL/data_readers

Freeman, A., & Durden, S. L. (1998). A three-component scattering model for polarimetric SAR data. *IEEE Transactions on Geoscience and Remote Sensing*, *36*(3), 963–973. https://doi.org/10.1109/36.673687

Freeman, A., & Farr, T. (2007). Modeling surface and subsurface scattering from saline soils. *Proceedings of the Progress in Electromagnetics Research Symposium*.

Fung, A. K. (1994). *Microwave scattering and emission models and their applications*. Artech House.

Fung, A. K., Li, Z., & Chen, K.-S. (1992). Backscattering from a randomly rough dielectric surface. *IEEE Transactions on Geoscience and Remote Sensing*, *30*(2), 356–369. https://doi.org/10.1109/36.134085

Fung, A. K., Liu, W.-Y., Chen, K.-S., & Tsay, M.-K. (2002). An improved model for bistatic scattering from rough surfaces. *Journal of Electromagnetic Waves and Applications*, *16*(5), 689–702. https://doi.org/10.1163/156939302X01119

Gaber, A., Koch, M., Griesh, M. H., & Sato, M. (2011). SAR remote sensing of buried faults: Implications for groundwater exploration in the western desert of egypt. *Sensing and Imaging*, *12*(3), 133–151. https://doi.org/10.1007/s11220-011-0066-1

Gaber, A., Soliman, F., Koch, M., & El-Baz, F. (2015). Using full-polarimetric SAR data to characterize the surface sediments in desert areas: A case study in El-Gallaba plain, Egypt. *Remote Sensing of Environment*, *162*, 11–28. https://doi.org/10.1016/j.rse.2015.01.024

Gao, B.-C. (1996). Ndwi-a normalized difference water index for remote sensing of vegetation liquid water from space. *Remote Sensing of Environment*, *58*(3), 257–266. https://doi.org/10.1016/S0034-4257(96)00067-3

Ghoneim, E., & El-Baz, F. (2007). The application of radar topographic data to mapping buried paleodrainage in the eastern sahara. *Journal of Arid Environments*, *69*(4), 658–675. https://doi.org/10.1016/j.jaridenv.2006.11.015

Grandjean, G., Paillou, P., Dubois-Fernandez, P., August-Bernex, T., Baghdadi, N. N., & Achache, J. (2001). Subsurface structures detection by combining L-band polarimetric SAR and GPR data: Example of the pyla dune (france). *IEEE Transactions on Geoscience and Remote Sensing*, *39*(6), 1245–1258. https://doi.org/10.1109/36.927447

Hajnsek, I., & Desnos, Y.-L. (Eds.). (2021). *Principles and application of polarimetric synthetic aperture radar* (Vol. 25). Springer Nature. https://doi.org/10.1007/978-3-030-56504-6

Hallikainen, M. T., Ulaby, F. T., Dobson, M. C., El-Rayes, M. A., & Wu, L. K. (1985). Microwave dielectric behavior of wet soil-part I: Empirical models and experimental observations. *IEEE Transactions on Geoscience and Remote Sensing*, *GE-23*(1), 25–34. https://doi.org/10.1109/TGRS.1985.289497

Heggy, E., Paillou, P., Ruffié, G., Malézieux, J.-M., Costard, F., & Grandjean, G. (2001). On water detection in the martian subsurface using sounding radar. *Icarus*, *154*(2), 244–257. https://doi.org/10.1006/icar.2001.6717

Howard, A. D. (1994). A detachment-limited model of drainage basin evolution. *Water Resources Research*, *30*(7), 2261–2285. https://doi.org/10.1029/94WR00757

Hsieh, C.-Y., Fung, A. K., Nesti, G., Sieber, A. J., & Coppo, P. (1997). A further study of the iem surface scattering model. *IEEE Transactions on Geoscience and Remote Sensing*, *35*(4), 901–909. https://doi.org/10.1109/36.602532

Japan Aerospace Exploration Agency (JAXA) Earth Observation Research Center. (2025). Global 25 m resolution palsar-2/palsar mosaic dataset description [Accessed July 2026]. https://www.eorc.jaxa.jp/ALOS/en/dataset/pdf/DatasetDescription_PALSAR2_Mosaic_ver260a.pdf

Jenson, S. K., & Domingue, J. O. (1988). Extracting topographic structure from digital elevation data for geographic information system analysis. *Photogrammetric Engineering and Remote Sensing*, *54*(11), 1593–1600.

Kellndorfer, J., Walker, W., LaPoint, E., Bishop, J., et al. (2010). Statistical fusion of lidar, InSAR, and optical remote sensing data for forest structure and biomass mapping. *Remote Sensing of Environment*, *114*(11), 2627–2640. https://doi.org/10.1016/j.rse.2010.06.022

Kim, J. (2023). Tracing archaeological places via the context of paleo geomorphic footprints using SAR/InSAR data fusion: A case on southern mesopotamia. *Remote Sensing*, *15*(6), 1636. https://doi.org/10.3390/rs15061636

Lasne, Y., Paillou, P., Freeman, A., Farr, T., McDonald, K. C., Ruffié, G., Malézieux, J.-M., Chapman, B., & Demontoux, F. (2008). Effect of salinity on the dielectric properties of geological materials: Implication for soil moisture detection by means of radar remote sensing. *IEEE Transactions on Geoscience and Remote Sensing*, *46*(6), 1674–1688. https://doi.org/10.1109/TGRS.2008.916220

Le Toan, T., Quegan, S., Davidson, M. W. J., Balzter, H., Paillou, P., Papathanassiou, K., Plummer, S., Rocca, F., Saatchi, S., Shugart, H., & Ulander, L. (2011). The BIOMASS mission: Mapping global forest biomass to better understand the terrestrial carbon cycle. *Remote Sensing of Environment*, *115*(11), 2850–2860. https://doi.org/10.1016/j.rse.2011.03.020

Lee, J.-S., & Pottier, E. (2009). *Polarimetric radar imaging: From basics to applications*. CRC Press. https://doi.org/10.1201/9781420054989

Lehner, B., & Grill, G. (2013). Global river hydrography and network routing: Baseline data and new approaches to study the world's large river systems. *Hydrological Processes*, *27*(15), 2171–2186. https://doi.org/10.1002/hyp.9740

Liu, G., Fu, H., Zhu, J., Wang, C., & Xie, Q. (2021). Penetration depth inversion in hyperarid desert from L-band InSAR data based on a coherence scattering model. *IEEE Geoscience and Remote Sensing Letters*, *18*(11), 1981–1985. https://doi.org/10.1109/LGRS.2020.3011706

Mallett, R. (2024). Iiem: Python implementation of the improved integral equation model [GitHub repository, accessed 17 July 2026].

Mätzler, C. (1998). Microwave permittivity of dry sand. *IEEE Transactions on Geoscience and Remote Sensing*, *36*(1), 317–319. https://doi.org/10.1109/36.655342

McCauley, J. F., Schaber, G. G., Breed, C. S., Grolier, M. J., Haynes, C. V., Issawi, B., Elachi, C., & Blom, R. (1982). Subsurface valleys and geoarcheology of the eastern sahara revealed by shuttle radar. *Science*, *218*(4576), 1004–1020. https://doi.org/10.1126/science.218.4576.1004

Mironov, V. L., Dobson, M. C., Kaupp, V. H., Komarov, S. A., & Kleshchenko, V. N. (2004). Generalized refractive mixing dielectric model for moist soils. *IEEE Transactions on Geoscience and Remote Sensing*, *42*(4), 773–785. https://doi.org/10.1109/TGRS.2003.823288

Mironov, V. L., Kosolapova, L. G., & Fomin, S. V. (2009). Physically and mineralogically based spectroscopic dielectric model for moist soils. *IEEE Transactions on Geoscience and Remote Sensing*, *47*(7), 2059–2070. https://doi.org/10.1109/TGRS.2008.2011631

Monika, Govil, H., & Thakur, M. (2022). Contribution of L-band SAR data for identification of buried/-paleochannels in jaisalmer region of rajasthan, india. *Advances in Space Research*, *70*(12), 3870–3877. https://doi.org/10.1016/j.asr.2022.03.036

Montgomery, D. R., & Foufoula-Georgiou, E. (1994). Channel network source representation using digital elevation models. *Water Resources Research*, *29*(12), 3925–3934. https://doi.org/10.1029/93WR02463

Nurmemet, I., Aili, Y., Xiang, Y., Aihaiti, A., Qin, Y., & Aizezi, B. (2025). A three-dimensional feature space model for soil salinity inversion in arid oases: Polarimetric SAR and multispectral data synergy. *Agronomy*, *15*(7), 1590. https://doi.org/10.3390/agronomy15071590

O'Callaghan, J. F., & Mark, D. M. (1984). The extraction of drainage networks from digital elevation data. *Computer Vision, Graphics, and Image Processing*, *28*(3), 323–344. https://doi.org/10.1016/S0734-189X(84)80011-0

Oh, Y., Sarabandi, K., & Ulaby, F. T. (1992). An empirical model and an inversion technique for radar scattering from bare soil surfaces. *IEEE Transactions on Geoscience and Remote Sensing*, *30*(2), 370–381. https://doi.org/10.1109/36.134086

Oré, G., Yepes, J., Góes, J. A., Oliveira, L. P., Teruel, B., & Hernandez-Figueroa, H. E. (2023). Soil moisture estimation of bare and vegetation-covered areas using a p/l/c-band sar [Date of current version May 2, 2023]. *arXiv*, *arXiv:2412.11874*. https://doi.org/10.48550/arXiv.2412.11874

Paillou, P., Grandjean, G., Malézieux, J.-M., Ruffié, G., Heggy, E., Piponnier, D., Dubois, P., & Achache, J. (2001). Performances of ground-penetrating radars in arid volcanic regions: Consequences for mars subsurface exploration. *Geophysical Research Letters*, *28*(5), 911–914. https://doi.org/10.1029/2000GL011746

Paillou, P. (2017). Mapping palaeohydrography in deserts: Contribution from space-borne imaging radar. *Water*, *9*(3), 194. https://doi.org/10.3390/w9030194

Paillou, P., Dall, J., Dubois-Fernandez, P., Hajnsek, I., Lucas, R., & Scipal, K. (2011). *BIOMASS secondary objectives assessment study* (ESA Study Report No. ITT AO 1-6543/10/NL/CT). ESA.

Paillou, P., Grandjean, G., Baghdadi, N., Heggy, E., August-Bernex, T., & Achache, J. (2003). Subsurface imaging in south-central egypt using low-frequency radar: Bir safsaf revisited. *IEEE Transactions on Geoscience and Remote Sensing*, *41*(7), 1672–1684. https://doi.org/10.1109/TGRS.2003.813275

Paillou, P., Lasne, Y., Heggy, E., Malézieux, J.-M., & Ruffié, G. (2006). A study of p□band synthetic aperture radar applicability and performance for mars exploration: Imaging subsurface geology and detecting shallow moisture. *Journal of Geophysical Research: Planets*, *111*(E06S11). https://doi.org/10.1029/2005JE002528

Paillou, P., Lopez, S., Marais, E., & Scipal, K. (2020). Mapping paleohydrology of the ephemeral kuiseb river, namibia, from radar remote sensing. *Water*, *12*(5), 1441. https://doi.org/10.3390/w12051441

Paillou, P., Schuster, M., Tooth, S., Farr, T., Rosenqvist, A., Lopez, S., & Malézieux, J.-M. (2009). Mapping of a major paleodrainage system in eastern Libya using orbital imaging radar: The Kufrah River. *Earth and Planetary Science Letters*, *277*(3-4), 327–333. https://doi.org/10.1016/j.epsl.2008.10.029

Paillou, P., Tooth, S., & Lopez, S. (2012). The kufrah paleodrainage system in libya: A past connection to the mediterranean sea? *C. R. Geoscience*, *344*, 406–414. https://doi.org/10.1016/j.crte.2012.07.002

Papathanassiou, K. P., & Cloude, S. R. (2001). Single-baseline polarimetric SAR interferometry. *IEEE Transactions on Geoscience and Remote Sensing*, *39*(11), 2352–2363. https://doi.org/10.1109/36.964971

Perna, S., et al. (2019). The ASI P-band helicopter-borne integrated sounder-SAR system: Preliminary results of the 2018 morocco desert campaign. *Proceedings of the IEEE International Geoscience and Remote Sensing Symposium (IGARSS)*, 8550–8553. https://doi.org/10.1109/IGARSS.2019.8898502

Piantanida, R. (2025). *BPS L1 SAR ATBD - algorithms theoretical baseline document* (Algorithm Theoretical Baseline Document No. BIO-BPS-L1-SAR-ATBD-ARE-010165) (Issue 1.2.3). Aresys / ESA.

Piantanida, R., & Boniardi, F. (2025). *BIOMASS L1a/b/c products format specification* (Product Format Document No. BIO-BPS-L1PFD-ARE-010076) (Issue 1.5.0). Aresys S.r.l. / ESA.

Planchon, O., & Darboux, F. (2001). A fast, simple and versatile algorithm to fill the depressions of digital elevation models. *Catena*, *46*(2-3), 159–176. https://doi.org/10.1016/S0341-8162(01)00164-3

Pottier, E. (2012). Polsarpro v5.0: An esa educational toolbox used for self-education in the field of polsar and pol-insar data analysis. *Proceedings of the IEEE International Geoscience and Remote Sensing Symposium (IGARSS)*, 7377–7380.

Rosen, P. A., Hensley, S., Joughin, I., et al. (2000). Synthetic aperture radar interferometry. *Proceedings of the IEEE*, *88*(3), 333–382. https://doi.org/10.1109/5.838084

Schaber, G. G., & Breed, C. S. (1999). The importance of sar wavelength in penetrating blow sand in northern arizona. *Remote Sensing of Environment*, *69*(2), 87–104. https://doi.org/10.1016/S0034-4257(99)00013-9

Schaber, G. G., McCauley, J. F., Breed, C. S., & Olhoeft, G. R. (1986). Shuttle imaging radar: Physical controls on signal penetration and subsurface scattering in the eastern sahara. *IEEE Transactions on Geoscience and Remote Sensing*, *GE-24*(4), 603–623. https://doi.org/10.1109/TGRS.1986.289677

Sedehi, M., Carbone, A., Imbembo, E., Hélière, F., Rommen, B., Fehringer, M., Scipal, K., Leanza, A., Simon, T., & Willemsen, P. (2021). Biomass-a fully polarimetric p-band sar esa mission [No DOI assigned (EUSAR/VDE conference paper)]. *Proceedings of EUSAR 2021: 13th European Conference on Synthetic Aperture Radar*, 238–241. https://ieeexplore.ieee.org/document/9472541

Shahidi, M., Hasted, J. B., & Jonscher, A. K. (1975). Electrical properties of dry and humid sand. *Nature*, *258*, 595–597. https://doi.org/10.1038/258595a0

Smith, B. G. (1967). Geometrical shadowing of a random rough surface. *IEEE Transactions on Antennas and Propagation*, *15*(5), 668–671. https://doi.org/10.1109/TAP.1967.1138999

Sultan, M., Arvidson, R. E., Sturchio, N. C., & Guinness, E. A. (1986). Lithologic mapping in arid regions with landsat thematic mapper data: Meatiq dome, egypt. *Geological Society of America Bulletin*, *97*(6), 748–762. https://doi.org/10.1130/0016-7606(1986)97<748:LMIARW>2.0.CO;2

Tarboton, D. G. (1997). A new method for the determination of flow directions and upslope areas in grid digital elevation models. *Water Resources Research*, *33*(2), 309–319. https://doi.org/10.1029/96WR03137

Topp, G. C., Davis, J. L., & Annan, A. P. (1980). Electromagnetic determination of soil water content: Measurements in coaxial transmission lines. *Water Resources Research*, *16*(3), 574–582. https://doi.org/10.1029/WR016i003p00574

Treuhaft, R. N., Madsen, S. N., Moghaddam, M., & van Zyl, J. J. (1996). Vegetation characteristics and underlying topography from interferometric radar. *Radio Science*, *31*(6), 1449–1485. https://doi.org/10.1029/96RS01763

Treuhaft, R. N., & Siqueira, P. R. (2000). Vertical structure of vegetated land surfaces from interferometric and polarimetric radar. *Radio Science*, *35*(1), 141–177. https://doi.org/10.1029/1999RS900108

Tsokas, A., Rysz, M., Pardalos, P. M., & Dipple, K. (2022). Sar data applications in earth observation: An overview. *Expert Systems with Applications*, *205*(117342). https://doi.org/10.1016/j.eswa.2022.117342

Tucker, C. J. (1979). Red and photographic infrared linear combinations for monitoring vegetation. *Remote Sensing of Environment*, *8*(2), 127–150. https://doi.org/10.1016/0034-4257(79)90013-0

Ul Islam, Z., Iqbal, J., Khan, J. A., & Qazi, W. A. (2016). Paleochannel delineation using landsat 8 oli and envisat asar image fusion techniques in cholistan desert, pakistan. *Journal of Applied Remote Sensing*, *10*(4), 046001. https://doi.org/10.1117/1.JRS.10.046001

Ulaby, F. T., & Long, D. G. (2014). *Microwave radar and radiometric remote sensing*. University of Michigan Press.

Ulaby, F. T., Moore, R. K., & Fung, A. K. (1986). *Microwave remote sensing: Active and passive, Vol. III: From theory to applications*. Artech House.

Wang, K., Wu, Y., Qiu, X., Zhu, J., Zheng, D., Shangguan, S., Pan, J., Liu, Y., Jiang, L., & Li, X. (2025). A novel airborne tomosar 3-d focusing method for accurate ice thickness and glacier volume estimation. *ISPRS Journal of Photogrammetry and Remote Sensing*, *220*, 593–607. https://doi.org/10.1016/j.isprsjprs.2025.01.011

Xiong, S., Muller, J.-P., & Li, G. (2017). The application of ALOS/PALSAR InSAR to measure subsurface penetration depths in deserts. *Remote Sensing*, *9*(6), 638. https://doi.org/10.3390/rs9060638

Xu, Y., Lu, Z., Bürgmann, R., Hensley, S., Fielding, E., & Kim, J. (2023). P-band sar for ground deformation surveying: Advantages and challenges. *Remote Sensing of Environment*, *287*, 113474. https://doi.org/10.1016/j.rse.2023.113474

Yamaguchi, Y., Moriyama, T., Ishido, M., & Yamada, H. (2005). Four-component scattering model for polarimetric SAR image decomposition. *IEEE Transactions on Geoscience and Remote Sensing*, *43*(8), 1699–1706. https://doi.org/10.1109/TGRS.2005.852084

Yu, L., Zhang, Y., Zhang, Q., Ji, Y., & Dong, Z. (2019). Performance analysis of ionospheric scintillation effect on p-band sliding spotlight sar system. *Sensors*, *19*(9), 2161. https://doi.org/10.3390/s19092161

Zebker, H. A., & Villasenor, J. (1992). Decorrelation in interferometric radar echoes. *IEEE Transactions on Geoscience and Remote Sensing*, *30*(5), 950–959. https://doi.org/10.1109/36.175330

Zhu, J., Liu, G., Zhao, R., Ding, X., & Fu, H. (2023). ML-based approach for inverting penetration depth of SAR signals over large desert areas. *Remote Sensing of Environment*, *295*, 113643. https://doi.org/10.1016/j.rse.2023.113643

A

Relevant sections Research Module

A.1. Principles of P-band SAR

P-band Synthetic Aperture Radar (SAR) operates within the microwave region of the electromagnetic spectrum. P-band is broadly classified within approximately 0.3-2 GHz (wavelengths 30-100 cm) (Tsokas et al., 2022). However, BIOMASS operates between 432-438 MHz, which corresponds to wavelengths of approximately 0.5-0.7 m (Sedehi et al., 2021). Compared to higher-frequency bands (X-, C-, and L-band), P-band signals exhibit enhanced penetration through dense vegetation, dry sand, and glacial ice. These long wavelengths experience reduced attenuation and lower volume decorrelation, meaning that signal coherence is better preserved despite the vertical distribution of scatterers.(Bamler & Hartl, 1998) As a result, stable backscattering contributions can be obtained from subsurface layers (Xu et al., 2023). Potential applications of P-band SAR include forest biomass estimation, subsurface imaging in ice and dry sand, soil moisture and permafrost monitoring, ground deformation mapping, and three-dimensional structural retrieval using polarimetric and tomographic techniques.

Despite these advantages, P-band SAR faces several technical challenges. Its low carrier frequency inherently limits spatial resolution, and signals are highly susceptible to ionospheric scintillation and radio-frequency interference (RFI) (Paillou et al., 2006). Ionospheric scintillation arises from small-scale plasma irregularities in the ionosphere, commonly occurring after sunset in equatorial and polar regions. These irregularities induce random phase and amplitude fluctuations, causing signal decorrelation during SAR integration. In focused imagery, this results in azimuth defocusing and peak power loss, degrading resolution and reducing image contrast (Yu et al., 2019). Therefore, successful deployment requires advanced phase calibration and signal processing techniques to mitigate the limited resolution, ionospheric disturbances, and reduced sensitivity (Wang et al., 2025).

The data used in this report were acquired primarily for vegetation and biomass mapping. BIOMASS employs fully polarimetric P-band SAR to generate global estimates of forest carbon storage. P-band SAR is particularly suited to this application because it penetrates the forest canopy and interacts with tree trunks and the ground surface (Alemohammad et al., 2018). However, this report focuses on two secondary applications of this data: glaciology and ice sounding, and subsurface geological mapping in arid environments.

A.2. BIOMASS system and data acquisition

Synthetic Aperture Radar (SAR) is a microwave remote sensing technology that produces high-resolution imagery by synthesizing a large antenna aperture from a moving platform, in this case, a satellite. A SAR system transmits microwave pulses and records the signal backscattered from the Earth's surface or objects (Hajnsek & Desnos, 2021). As microwaves penetrate clouds, fog, and smoke, SAR enables continuous, all-weather data acquisition independent of daylight (Tsokas et al., 2022).

The BIOMASS mission employs a single low Earth orbit satellite carrying a fully polarimetric P-band Synthetic Aperture Radar payload. Instead of using separate transmit and receive antennas, the sys-

tem is based on an offset feed-reflector design (Sedehi et al., 2021). The payload consists of two main components: a 12-m Large Deployable Reflector (LDR) and an instrument unit that houses the electronics and the Feed Array (FA). The Feed Array illuminates the reflector, which directs the radar signal toward the Earth in a left-looking stripmap imaging mode (Sedehi et al., 2021).

Data acquisition is performed in a monostatic configuration, meaning that the same antenna system is used for both transmission and reception (Hajnsek & Desnos, 2021). The instrument operates in quad-polarization mode, transmitting horizontal (H) and vertical (V) polarised pulses alternately rather than simultaneously (Sedehi et al., 2021). The backscattered signals are received in both polarizations at the same time, allowing the radar to preserve the relative phase information between channels (Hajnsek & Desnos, 2021). This approach enables the measurement of all four linear polarization combinations (HH, VV, HV, and VH), providing fully polarimetric data. Such data capture complementary information on surface and volume scattering processes, which is critical for BIOMASS objectives, including separating canopy and ground scattering in forests and detecting three-dimensional subsurface structures in glacial and dry environments (Hajnsek & Desnos, 2021).

A.2.1. Applications into arid environments

Satellite-based P-band SAR represents a fundamentally new observation regime, as previous subsurface studies relied primarily on airborne systems with short baselines and flexible geometries. This section highlights key airborne campaigns over glacial ice sheets and arid deserts. shallow snowpacks (Oré et al., 2023).

In arid environments, P-band SAR discriminates subsurface geological and hydrological structures (Paillou et al., 2006). The NASA/JPL AIRSAR survey over Ward Terrace, Arizona, demonstrated that 68cm P-band radar can fully penetrate sand deposits opaque to C- and L-band, revealing buried terraces and dendritic paleochannels (Schaber & Breed, 1999). In the Eastern Sahara, P-band SAR mapped paleo-drainage systems, impact craters, and tectonic faults, with 4-6m penetration in loose sand. P-band also detects subsurface moisture via dielectric contrasts, serving as terrestrial analogues for Mars exploration (Paillou et al., 2006).

These studies demonstrate that P-band SAR enables subsurface sensing in both glacial and arid environments, though with varying robustness. Spaceborne systems such as BIOMASS face inherent constraints from low operating frequency, RFI, and ionospheric distortions like scintillation and Faraday Rotation (FR) (Xu et al., 2023). FR significantly distorts P-band signals by rotating their polarization plane, reaching magnitudes up to 30°, which would compromise the polarimetric scattering matrix if left uncorrected. (Sedehi et al., 2021) To mitigate these effects BIOMASS utilises a dawn-dusk Sun-synchronous orbit to avoid scintillation hotspots and leverages its fully polarimetric (Quad-Pol) data to mathematically remove the rotation via the Bickel and Bates algorithm. Furthermore, BIOMASS employs sliding spotlight mode to improve azimuth resolution within its strictly allocated 432-438 MHz frequency range (Sedehi et al., 2021). While essential for detailed subsurface characterisation, this extended integration time increases susceptibility to ionospheric fluctuations, requiring advanced correction and signal processing (Yu et al., 2019).

A.3. Physics of electromagnetic propagation and subsurface scattering

The BIOMASS P-band SAR operates at frequencies of approximately 435 MHz, corresponding to wavelengths of 0.5-0.7 metres (Sedehi et al., 2021). At these wavelengths, electromagnetic waves can penetrate low-loss materials such as dry sand or cold glacial ice, allowing radar returns to originate not only from the surface but also from subsurface structures. In this section, the fundamental physics and relevant electromagnetic relationships for P-band subsurface SAR are summarised.

The response of a medium to an electromagnetic wave is described by its complex relative permittivity (Hajnsek & Desnos, 2021) as given in Equation A.1,

$$\varepsilon_r = \varepsilon' - j\varepsilon''. \tag{A.1}$$

Here ε' governs phase velocity and refraction, and ε'' determines attenuation due to dielectric relaxation and conductive losses. The real part controls the propagation speed of the wave inside the medium,

while the imaginary part contributes to the attenuation constant. Materials with small ε'' relative to ε' therefore exhibit weak electromagnetic damping and are classified as low-loss media (Paillou et al., 2006).

Penetration depth depends on these dielectric properties. Under the low-loss approximation for plane-wave propagation in a homogeneous half-space the penetration depth can be approximated by Equation A.2 (Paillou et al., 2006),

$$\delta_p \approx \frac{\lambda}{2\pi\sqrt{\varepsilon'}\tan\delta}, \quad \tan\delta = \frac{\varepsilon''}{\varepsilon'}. \tag{A.2}$$

Here λ represents the free-space wavelength of the radar signal, and $\tan\delta$ is the loss tangent. The penetration depth δ_p corresponds to the distance at which the wave amplitude decreases to $1/e$ of its initial value. For $\varepsilon'' \ll \varepsilon'$, attenuation is weak and δ_p becomes large. This explains why low-loss materials such as dry sand and cold glacial ice permit significant P-band penetration, enabling detection of buried reflectors (Bekaert et al., 2014).

As the wave propagates within the medium, its velocity is reduced according to the dielectric constant (Equation A.3),

$$v = \frac{c}{\sqrt{\varepsilon'}}, \tag{A.3}$$

where c is the speed of light in vacuum. The two-way travel-time delay introduced by a reflector at depth z is given by Equation A.4,

$$\Delta t = \frac{2z\sqrt{\varepsilon'}}{c}. \tag{A.4}$$

If free-space propagation is assumed during SAR focusing, this reduced velocity leads to systematic overestimation of reflector depth. Therefore, accurate subsurface imaging requires the incorporation of medium-dependent propagation speed.

Refraction at the interface between air and the subsurface further bends the propagating wave toward the surface normal. This behaviour follows from Snell's law and is expressed as

$$\sin\theta_t = \frac{\sin\theta_i}{\sqrt{\varepsilon'}}. \tag{A.5}$$

Here θ_i denotes the angle of incidence, defined as the angle between the incident radar wave and the local surface normal in air, while θ_t is the transmitted angle inside the subsurface medium. Assuming a non-magnetic medium ($\mu_r \approx 1$) and air as the incident medium ($\varepsilon_r \approx 1$), materials with $\varepsilon' > 1$ yield $\theta_t < \theta_i$, i.e., refraction toward the normal. This altered propagation path introduces lateral shifts and depth bias of buried reflectors if not accounted for in focusing or inversion.

Beyond propagation, the SAR return is controlled by scattering within the resolution cell. Backscatter is often dominated by surface scattering from rough interfaces, while subsurface contributions arise from volume scattering and discrete internal or basal reflectors. Their relative contributions depend on dielectric contrast, roughness-to-wavelength ratio, and structural heterogeneity (Alemohammad et al., 2018). In low-loss media, subsurface scattering can remain coherent despite strong surface returns. Depth-resolved imaging, therefore, requires correction for reduced velocity and refraction. Model-based focusing, incorporates medium-dependent propagation to improve reflector localization (Wang et al., 2025). Tomographic SAR (TomoSAR) further enhances vertical discrimination by coherently combining acquisitions with varying perpendicular baselines (Wang et al., 2025). The vertical sampling is determined by the vertical wavenumber in Equation A.6,

$$k_z = \frac{4\pi B_\perp}{\lambda R}. \tag{A.6}$$

Here $B_\perp$ is the perpendicular (cross-track) baseline between successive SAR acquisitions, λ is the radar wavelength, and R is the slant range distance to the target. The vertical reflectivity profile is reconstructed using Equation A.7,

$$\gamma(z) = \int S(B_\perp) e^{jk_z z}\, dB_\perp, \tag{A.7}$$

where $S(B_\perp)$ denotes the measured complex SAR signal for each baseline and $\gamma(z)$ represents the reconstructed vertical reflectivity profile at depth z (Wang et al., 2025). In practice, this integral formulation is discretised over the available baselines.

The achievable resolution in the range direction within the medium depends on both radar bandwidth and dielectric properties and is described by Equation A.8,

$$\Delta z \approx \frac{c}{2B\sqrt{\varepsilon'}}. \tag{A.8}$$

This expression represents the medium-corrected range resolution, highlighting the influence of reduced propagation velocity on depth discrimination. In contrast, tomographic elevation resolution is primarily governed by the total perpendicular baseline extent. Together, these relationships illustrate the trade-offs between system design parameters, material properties, and the clarity of reconstructed subsurface features (Xu et al., 2023).

B

Methodological details and sensitivity analyses

B.1. Scene-centre baseline geometry

For experiments in which the perpendicular baseline was derived from orbit information, the scene-centre geometry was calculated from the BIOMASS orbit state vectors following standard InSAR formulations (Bamler & Hartl, 1998; Rosen et al., 2000). The scene-centre coordinates were first represented in Earth-Centred Earth-Fixed (ECEF) coordinates as $\mathbf{x}_t$. The baseline vector between the master and secondary acquisitions was then defined as

$$\mathbf{B} = \mathbf{s}_2 - \mathbf{s}_1, \tag{B.1}$$

where $\mathbf{s}_1$ and $\mathbf{s}_2$ denote the master and secondary satellite position vectors. The line-of-sight vector from the master acquisition to the scene centre was calculated as

$$\boldsymbol{\ell} = \mathbf{x}_t - \mathbf{s}_1, \tag{B.2}$$

with corresponding unit vector

$$\hat{\boldsymbol{\ell}} = \frac{\boldsymbol{\ell}}{\|\boldsymbol{\ell}\|}. \tag{B.3}$$

Using the master velocity vector $\mathbf{v}_1$, the along-track unit vector was computed as

$$\hat{\mathbf{t}} = \frac{\mathbf{v}_1}{\|\mathbf{v}_1\|}. \tag{B.4}$$

The unit normal to the track-LOS plane was then defined as

$$\hat{\mathbf{n}} = \frac{\hat{\mathbf{t}} \times \hat{\boldsymbol{\ell}}}{\|\hat{\mathbf{t}} \times \hat{\boldsymbol{\ell}}\|}. \tag{B.5}$$

The perpendicular baseline was obtained from

$$B_\perp = \mathbf{B} \cdot \hat{\mathbf{n}}, \tag{B.6}$$

while the scene-centre slant range was calculated as

$$R = \|\boldsymbol{\ell}\|. \tag{B.7}$$

This procedure provides the true geometrical perpendicular baseline directly from the acquisition geometry rather than relying on precomputed metadata fields.

B.2. Influence of multilooking on the co-polarization ratio

The dielectric-roughness inversion relies strongly on the observed co-polarization difference

$$VV - HH, \tag{B.8}$$

which was found to differ systematically from the polarization differences represented within the lookup table. Because polarization ratios can be influenced by speckle fluctuations and local averaging, an additional sensitivity analysis was performed to evaluate the effect of multilooking on the observed $VV - HH$ distribution.

The analysis was repeated using several multilooking configurations: 12×2, 24×4, and 36×6 pixels. For each case, the distribution of the observed co-polarization difference and the corresponding HH-VV scatter cloud were evaluated and compared with the minimum polarization difference represented within the LUT.

Figure B.1 demonstrates that the median observed polarization difference remains remarkably stable across all multilooking factors, varying only between approximately 0.21 and 0.22 dB. In contrast, the minimum polarization difference represented within the LUT remains approximately 0.75 dB.

The persistence of this discrepancy after substantial spatial averaging indicates that the mismatch between observations and the LUT is not primarily caused by speckle noise or insufficient averaging of the SAR observables. Instead, the results suggest that the observed polarization-ratio distribution is intrinsically shifted towards lower values than those naturally generated by the adopted forward model.

This finding supports the interpretation presented in Chapter 5, where LUT-boundary accumulation in the retrieved dielectric constant and roughness maps was linked to a systematic mismatch between the measured $VV - HH$ response and the range of polarization responses represented within the lookup table. Because the median polarization ratio remains essentially unchanged over a wide range of multilooking factors, the observed LUT-boundary effects cannot be attributed solely to speckle-induced variability.

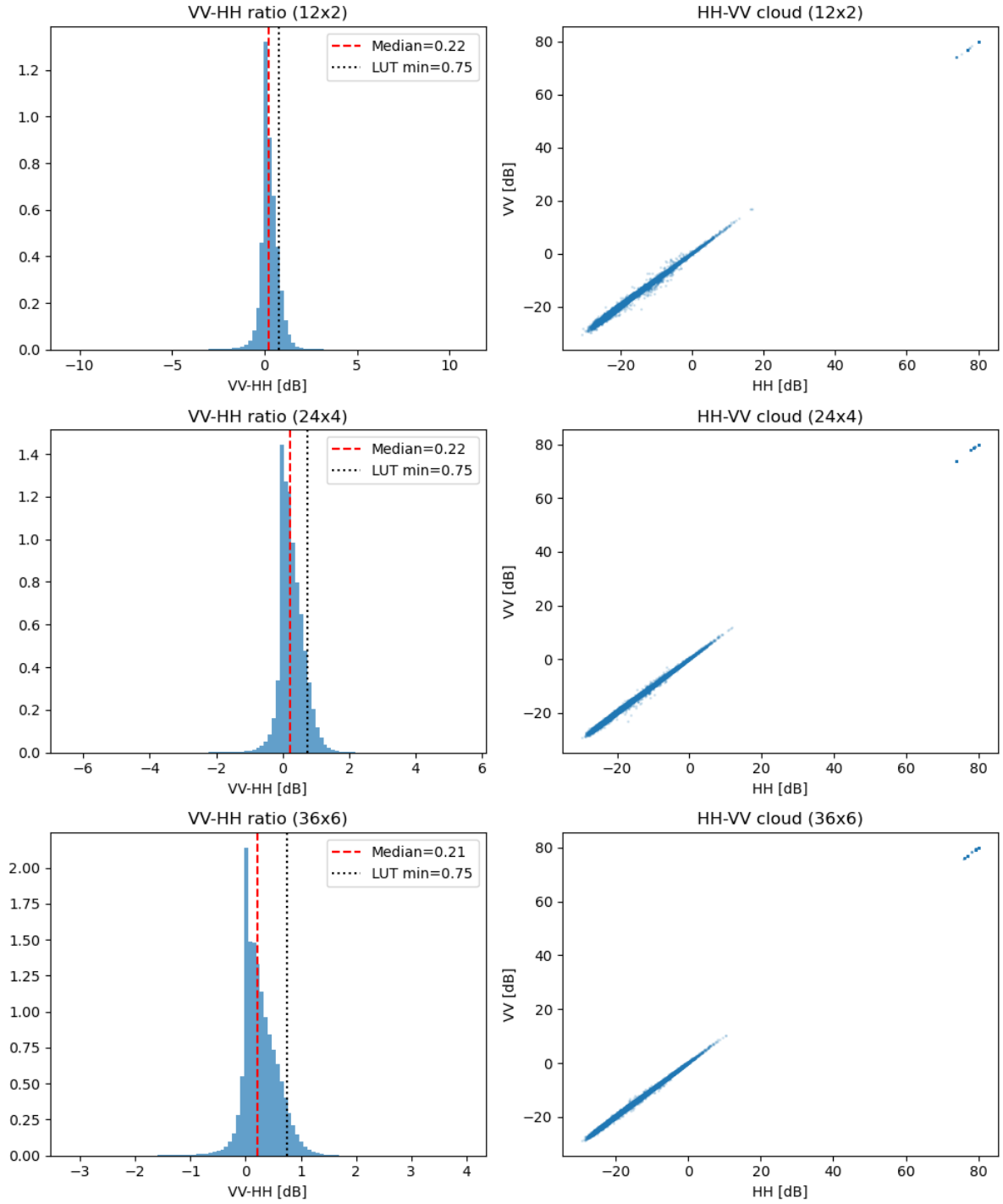

Figure B.1: Sensitivity of the observed co-polarization difference ($VV - HH$) to multilooking window size. Histograms (left column) and HH-VV scatter clouds (right column) are shown for multilooking factors of 12×2, 24×4, and 36×6 pixels. The red dashed line indicates the median observed polarization difference, whereas the black dotted line denotes the minimum $VV - HH$ value represented within the LUT. The discrepancy remains largely unchanged across all multilooking configurations.

B.3. Correlation-length parameterisation for the I2EM LUT

The Improved Integral Equation Model (I2EM) requires both the root-mean-square (RMS) surface height s and the correlation length L to describe surface roughness. While a spatially varying roughness estimate was available through the retrieval framework, independent measurements of correlation

length were not available for either study area. Consequently, a complete three-parameter inversion of dielectric constant, RMS height, and correlation length was not feasible.

To maintain a two-parameter inversion comparable to the nominal dielectric-roughness retrieval, the correlation length was linked to RMS height through a fixed proportionality relationship,

$$L = \eta s, \tag{B.9}$$

where η is the correlation-length-to-RMS-height ratio. The nominal I2EM lookup table used

$$\eta = 6. \tag{B.10}$$

This choice should not be interpreted as a universally valid physical constant. Published roughness studies show substantial variability in both RMS height and correlation length, and no single ratio has been demonstrated to be applicable across all surface types, frequencies, and measurement techniques. The adopted value was therefore treated as a pragmatic inversion parameter rather than a physically validated terrain property.

To evaluate the impact of this assumption, a sensitivity analysis was performed in which synthetic I2EM backscatter was generated for

$$\eta \in \{2, 4, 6, 8, 10, 15, 20\}, \tag{B.11}$$

while all other parameters were held fixed. The corresponding HH and VV backscatter responses were evaluated for several representative roughness values spanning the retrieval range,

$$k_s \in \{0.046,\ 0.15,\ 0.30,\ 0.456\}, \tag{B.12}$$

using a representative dielectric constant of $\varepsilon' = 3.0$ and an incidence angle of $26°$.

Figure B.2 shows the resulting sensitivity of HH and VV backscatter to the assumed correlation-length ratio. The influence of L/s is strongest for the smoothest surfaces ($k_s = 0.046$), where variations in correlation length produce substantial changes in predicted backscatter. In contrast, the sensitivity decreases with increasing roughness, indicating that the correlation-length assumption becomes progressively less important for rougher surfaces.

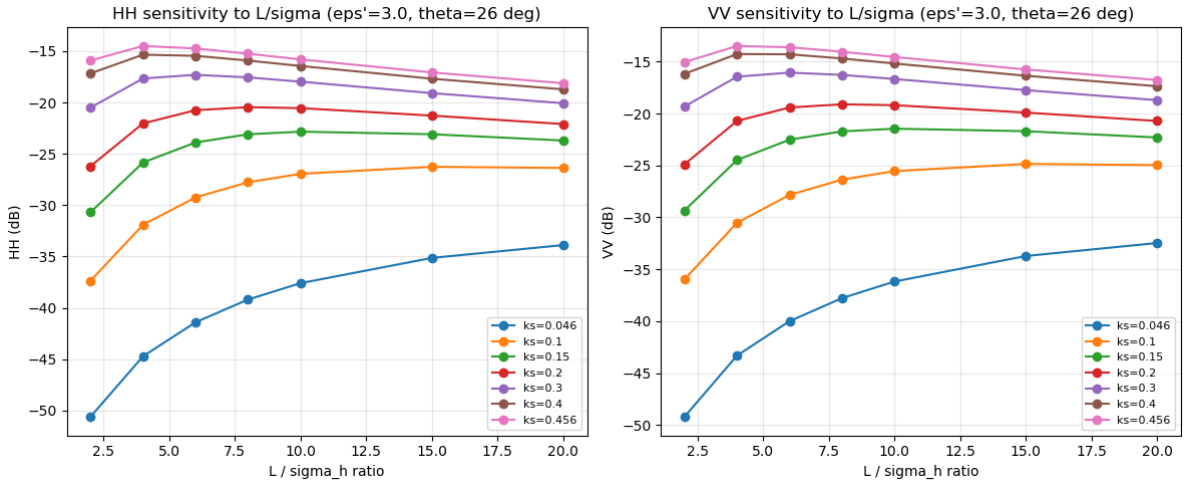

Figure B.2: Sensitivity of simulated HH and VV backscatter to the assumed correlation-length-to-RMS-height ratio (L/s) for representative roughness values at $\varepsilon' = 3.0$ and $\theta = 26°$.

A second experiment was performed to quantify the effect of correlation-length mismatch on the inversion itself. A lookup table was generated assuming a fixed ratio of

$$L/s = 6, \tag{B.13}$$

while synthetic observations were generated using alternative "true" ratios between 2 and 20. These synthetic observations were then inverted using the fixed-ratio LUT. The test was performed over the parameter space

$$\varepsilon' \in \{2.8,\ 3.0,\ 4.5,\ 6.0,\ 8.0\}, \tag{B.14}$$

and

$$k_s \in \{0.046,\ 0.15,\ 0.30,\ 0.456\}. \tag{B.15}$$

The resulting mean absolute retrieval biases are shown in Figure B.3. Both dielectric and roughness errors reach a minimum near the adopted value of $L/s = 6$. As the true ratio departs from the assumed value, retrieval bias increases progressively. The effect is particularly noticeable for dielectric constant, whereas the retrieved roughness parameter remains comparatively stable over much of the tested range.

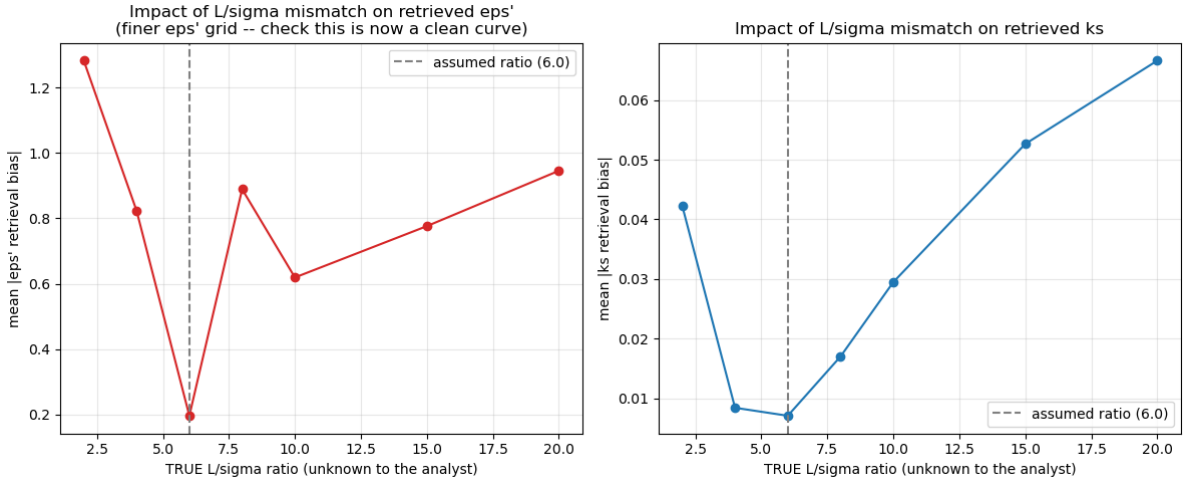

Figure B.3: Influence of L/s mismatch on the retrieved dielectric constant and roughness parameter. Synthetic observations were generated using different true correlation-length ratios and inverted using a LUT constructed with the nominal value $L/s = 6$. The dashed line indicates the ratio used in the LUT generation.

The sensitivity analysis indicates that the adopted value of $L/s = 6$ corresponds to a near-minimum retrieval-bias region for the investigated parameter space. However, this result should not be interpreted as proof that $L/s = 6$ is the physically correct ratio for the study areas. Instead, it demonstrates that the chosen parametrisation provides a stable compromise within the tested roughness and dielectric ranges. The retrieved dielectric and roughness products should therefore be interpreted as effective estimates obtained under a prescribed correlation-length assumption.

Future work could reduce this source of uncertainty through field-based roughness measurements, independent correlation-length observations, or the development of P-band-specific calibration relationships between RMS height and correlation length.

B.4. Calibration of the roughness-activation function

The reduced-parameter forward model described in Section 3.4.6 represents surface roughness through the empirical roughness-activation term

$$G_r(k_s) = 1 - \exp[-\beta(k_s)^a], \tag{B.16}$$

where $k_s = ks$ is the wavelength-normalised roughness parameter, $k = 2\pi/\lambda$ is the radar wavenumber, and s is the RMS surface height. Since k has units of m^{-1} and s has units of m, the product k_s is dimensionless. Consequently, the exponent $\beta(k_s)^a$ must also be dimensionless, implying that both β and a are dimensionless calibration parameters.

The choice of a dimensionless roughness parameter is consistent with rough-surface scattering theory, where radar sensitivity is controlled primarily by roughness relative to the wavelength rather than by absolute roughness alone. The adopted parameterization therefore approximates the dependence of backscatter on wavelength-normalised roughness predicted by IEM and I2EM while retaining a computationally simple analytical form.

The purpose of this function is not to reproduce the full rough-surface scattering physics represented by I2EM, but rather to provide a computationally efficient approximation suitable for generation of the reduced-parameter lookup table. The originally adopted parameterization was chosen to reproduce the expected qualitative increase in backscatter with increasing roughness. However, because an I2EM-based retrieval was also implemented in this thesis, the availability of a more physically based rough-surface scattering model provided an opportunity to evaluate whether the adopted roughness-activation formulation was consistent with the roughness dependence predicted by I2EM.

To assess this, the I2EM forward model was evaluated over the roughness interval used in the retrieval,

$$0.046 \leq k_s \leq 0.456, \tag{B.17}$$

while holding dielectric constant, incidence angle, and correlation-length parameterization fixed. For each roughness value, the corresponding co-polarized backscatter σ^0_{VV} was computed using the same I2EM implementation employed to generate the I2EM lookup table. The resulting backscatter curve was converted from decibel units to linear power and normalised to the interval $[0, 1]$ to obtain a dimensionless roughness-response curve directly comparable to $G_r(k_s)$.

The roughness-activation function was then fitted to the normalised I2EM response using nonlinear least squares,

$$G_r(k_s) = 1 - \exp(-\beta k_s^a). \tag{B.18}$$

Figure B.4 compares the normalised I2EM roughness response with the adopted activation function and the fitted solutions. The unconstrained fit yielded substantially larger values of β and a than the originally adopted formulation. However, when the exponent was fixed at

$$a = 1, \tag{B.19}$$

the fitted value was

$$\beta \approx 2.72, \tag{B.20}$$

which closely matched the observed roughness dependence over the retrieval range.

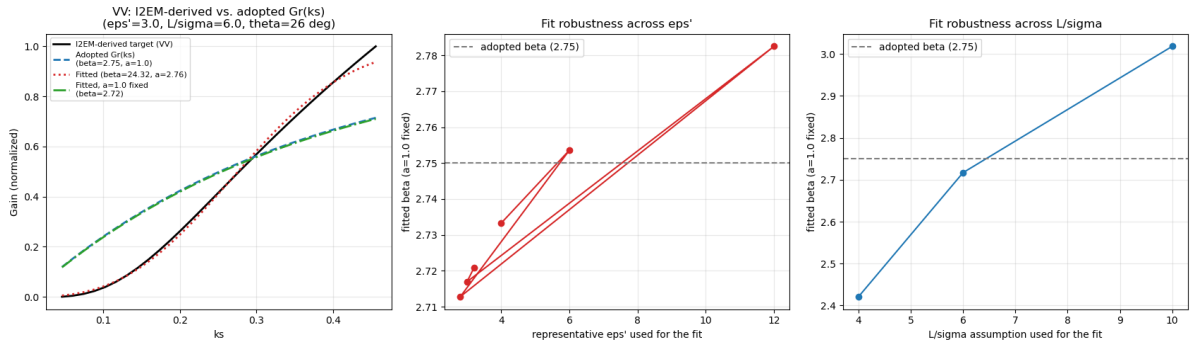

Figure B.4: Calibration of the empirical roughness-activation function against the normalised I2EM roughness response. Left: comparison between the normalised I2EM response and the adopted activation function. Middle: fitted β values obtained for different representative dielectric constants with $a = 1$ fixed. Right: fitted β values obtained for different correlation-length assumptions.

The robustness of the fitted coefficient was evaluated across representative dielectric constants,

$$\varepsilon' \in \{2.8,\ 3.0,\ 3.2,\ 4.0,\ 6.0,\ 12.0\}, \tag{B.21}$$

and across several correlation-length parameterizations,

$$L/s \in \{4,\ 6,\ 10\}. \tag{B.22}$$

The fitted coefficient remained highly stable across dielectric constant, varying only between approximately

$$2.71 \leq \beta \leq 2.78. \tag{B.23}$$

A somewhat larger variation was observed for different correlation-length assumptions, with fitted values ranging from approximately

$$2.42 \leq \beta \leq 3.02. \tag{B.24}$$

For the nominal retrieval configuration,

$$\varepsilon' = 3.0, \qquad L/s = 6, \qquad \theta = 26^\circ, \tag{B.25}$$

the fitted value was approximately

$$\beta = 2.72. \tag{B.26}$$

Consequently, the adopted coefficient was set to

$$\beta = 2.72, \qquad a = 1.0, \tag{B.27}$$

which provides a close approximation to the I2EM-predicted roughness response under the nominal retrieval conditions.

It is important to note that this procedure does not constitute independent validation. Rather, it provides internal consistency between the simplified forward model and the I2EM-based retrieval, because both depend on the same underlying rough-surface scattering framework. The calibration therefore reduces arbitrary parameter selection but does not eliminate uncertainty associated with roughness parameterization or the assumed correlation-length relationship described in Appendix B.3.

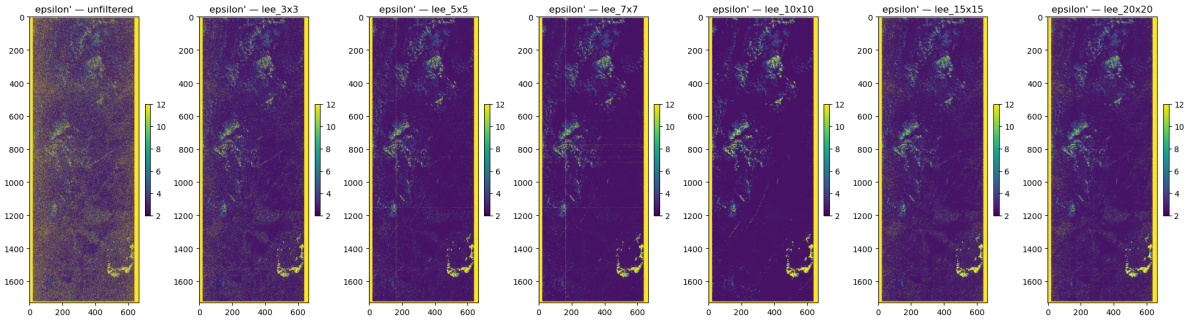

Figure B.5: Lee Filter Size Comparison

B.5. Lee filter window size selection

To determine an appropriate Lee filter window size, dielectric constant (ε') retrievals were generated using window sizes of 3×3, 5×5, 7×7, 10×10, 15×15, and 20×20 pixels and compared against the unfiltered result (Figure B.5). The evaluation considered both visual inspection and quantitative metrics describing speckle suppression and preservation of paleochannel contrast.

Speckle reduction was assessed using the median local standard deviation of the retrieved ε' values within a moving 5×5 window. The unfiltered image exhibited the highest variability (3.15), while progressively larger Lee filter windows reduced local variability to 1.51 (3×3), 0.38 (5×5), 0.14 (7×7), and 0.04 (10×10), demonstrating a substantial reduction in speckle with increasing filter size.

Preservation of geologically meaningful features was evaluated using the contrast between pixels associated with the inferred paleochannel network and the surrounding background. All filtered products showed improved channel-to-background contrast compared to the unfiltered image, increasing from 7.30 in the unfiltered case to values between approximately 8.0 and 8.3 after filtering. Although larger windows produced slightly higher contrast values, these gains were modest relative to the accompanying loss of spatial detail.

Based on the combined quantitative and visual assessment, a 5×5 Lee filter was adopted for the final workflow. This window size reduced local variability by nearly an order of magnitude relative to the unfiltered image while preserving the continuity, width, and morphology of the interpreted paleochannel features. Larger windows provided only marginal additional improvements in noise suppression and contrast, but increasingly smoothed fine-scale spatial variability and reduced the visibility of narrow channel structures. The 5×5 filter therefore represented the best compromise between speckle suppression and spatial-feature preservation.

B.6. Improved integral equation model (I2EM)

The rough-surface backscatter lookup table used in this study was generated using the Improved Integral Equation Model (I2EM). I2EM is a physically based electromagnetic scattering model that predicts radar backscatter from a statistically rough dielectric surface. The model extends the original Integral Equation Model (IEM) developed by Fung et al. (1992) and incorporates subsequent improvements to represent roughness-induced scattering over a wider range of surface conditions (Fung et al., 2002; Hsieh et al., 1997). The implementation used in this work was based on the open-source Python translation of the I2EM equations developed by Mallett (2024), which follows the formulation presented by Ulaby and Long (2014).

Within I2EM, the surface is represented statistically through its root-mean-square (RMS) height s, correlation length l, and an assumed autocorrelation function. Rather than explicitly representing individual surface facets, these quantities define a roughness spectrum that governs the contribution of different spatial scales to the scattered field (Fung et al., 2002; Hsieh et al., 1997). Surface roughness enters the model through the dimensionless parameters

$$k_s = k\, s, \tag{B.28}$$

and

$$kl = k\,l, \tag{B.29}$$

where k is the electromagnetic wavenumber,

$$k = \frac{2\pi f}{c}, \tag{B.30}$$

with f denoting radar frequency and c the speed of light.

The dielectric properties of the surface are introduced through the Fresnel reflection coefficients. For an incidence angle θ and complex relative permittivity ε_r, the horizontal and vertical reflection coefficients are

$$R_H(\varepsilon_r, \theta) = \frac{\cos\theta - \sqrt{\varepsilon_r - \sin^2\theta}}{\cos\theta + \sqrt{\varepsilon_r - \sin^2\theta}}, \tag{B.31}$$

and

$$R_V(\varepsilon_r, \theta) = \frac{\varepsilon_r\cos\theta - \sqrt{\varepsilon_r - \sin^2\theta}}{\varepsilon_r\cos\theta + \sqrt{\varepsilon_r - \sin^2\theta}}. \tag{B.32}$$

These coefficients determine the polarization dependence of the scattering response and constitute the principal mechanism through which variations in dielectric constant influence the predicted HH and VV backscatter (Fung et al., 1992, 2002).

Unlike empirical scattering models, I2EM is derived from electromagnetic theory and represents the scattered field as a spectral series. The number of terms included in the series is determined adaptively according to the surface roughness, allowing the solution to converge efficiently while retaining higher-order roughness contributions where necessary (Hsieh et al., 1997; Ulaby & Long, 2014). For each spectral order n, polarization-dependent scattering amplitudes are calculated for both HH and VV channels. The final normalised radar cross sections are obtained by summing the weighted contribution of all spectral orders:

$$\sigma^0_{VV} = \frac{k^2}{2}\exp\left[-s^2\left(k_z^2 + k_{sz}^2\right)\right] S \sum_{n=1}^{T_s} \frac{s^{2n}}{n!} W_n |I_{VV,n}|^2, \tag{B.33}$$

$$\sigma^0_{HH} = \frac{k^2}{2}\exp\left[-s^2\left(k_z^2 + k_{sz}^2\right)\right] S \sum_{n=1}^{T_s} \frac{s^{2n}}{n!} W_n |I_{HH,n}|^2, \tag{B.34}$$

where W_n denotes the roughness-spectrum weighting term, $I_{pp,n}$ represents the polarization-dependent scattering amplitude for polarization pp, k_z and k_{sz} are the vertical components of the incident and scattered wave vectors, respectively, and S is a shadowing correction factor (Fung et al., 2002; Hsieh et al., 1997).

To account for geometric masking of rough-surface facets at oblique incidence angles, I2EM applies a shadowing correction based on the statistical surface slope distribution. The shadowing term modifies the final backscatter prediction and becomes increasingly important for rough surfaces and larger incidence angles (Fung et al., 2002; Smith, 1967). The final backscatter coefficients are reported in decibels as

$$\sigma^0_{pp,\mathrm{dB}} = 10\log_{10}\left(\sigma^0_{pp}\right), \tag{B.35}$$

where pp denotes either HH or VV polarization.

B.6.1. Adaptations for Lookup-Table Inversion

The original I2EM implementation provides forward simulations of co-polarized and cross-polarized radar backscatter for specified dielectric and roughness conditions. In this study, the model was adapted for use within a lookup-table (LUT) retrieval framework.

First, only the co-polarized HH and VV channels were retained. Since the inversion relies on differences in the dielectric and roughness sensitivity of the co-polarized response, the cross-polarized component was not required and was therefore omitted. This modification reduces computational complexity while preserving the physical basis of the scattering model.

Second, the forward model was used to generate a precomputed multidimensional lookup table rather than being evaluated during each inversion iteration. The LUT contains predicted values of σ^0_{HH} and σ^0_{VV} over a discretized dielectric–roughness parameter space. During retrieval, observed backscatter measurements are compared against the precomputed model responses and the parameter combination that minimizes the mismatch is selected.

A generic form of the retrieval cost function is

$$J(\varepsilon'_i, \rho_j; \mathbf{x}) = w_{HH} \left[\log_{10} \sigma^0_{HH,\mathrm{obs}} - \log_{10} \widehat{\sigma}^0_{HH,ij}\right]^2 + w_{VV} \left[\log_{10} \sigma^0_{VV,\mathrm{obs}} - \log_{10} \widehat{\sigma}^0_{VV,ij}\right]^2, \tag{B.36}$$

where ε'_i is the candidate dielectric constant, ρ_j is the candidate roughness state, σ^0_{obs} denotes the observed backscatter, and $\widehat{\sigma}^0$ represents the corresponding I2EM prediction from the lookup table. The optimal solution is obtained through

$$(\widehat{\varepsilon}', \widehat{\rho}) = \arg\min_{\varepsilon'_i, \rho_j} J(\varepsilon'_i, \rho_j). \tag{B.37}$$

An optional roughness prior was introduced within the inversion procedure to stabilize the retrieval in regions where multiple dielectric–roughness combinations produce similar backscatter responses. Importantly, this prior acts only during the inverse step and does not modify the I2EM forward calculations. Consequently, all predicted backscatter values remain fully consistent with the original electromagnetic scattering formulation.

The adaptations implemented in this study therefore modify the computational workflow rather than the underlying physics of I2EM. The forward model retains its original representation of Fresnel reflection, roughness-spectrum weighting, multiple-scattering contributions, adaptive spectral-series truncation, and shadowing correction, while the LUT framework enables efficient inversion of large SAR datasets.

C

Additional Results

C.1. HH-VV phase difference analysis

As an additional investigation, the co-polarized phase difference between the HH and VV channels was evaluated as a potential indicator of buried paleochannel structures. Two representative regions of interest containing candidate paleochannel features were selected within the Sahara study area. Cross-sections were extracted in both the range and azimuth directions through the mapped channel regions, and the resulting phase-difference profiles were compared with the surrounding terrain. Figure C.1 shows the location of the extracted cross-sections for the first region of interest. The selected range and azimuth profiles intersect the mapped paleochannel and were visualized on both the stacked backscatter image and the HH-VV phase-difference map. The corresponding phase-difference profiles are shown in Figure C.2. Figure C.3 presents the cross-sections for a second region of interest within the same BIOMASS scene, while the corresponding phase-difference profiles are shown in Figure C.4. In both regions of interest, the HH-VV phase difference exhibits substantial local variability over short spatial scales.

Although small fluctuations are observed within the mapped paleochannel boundaries, comparable variations are also present throughout the surrounding terrain. No distinct transition or systematic phase anomaly is evident at the channel boundaries in either the range or azimuth profiles. Furthermore, the mean phase values within the paleochannel are broadly comparable to those outside the channel, indicating limited channel-background contrast. These results demonstrate that the HH-VV phase difference captures spatial variability related to landscape structure but does not exhibit a consistent paleochannel-specific signature within the analysed BIOMASS observations.

While several candidate paleochannel features can be visually identified in the HH-VV phase-difference imagery, the extracted profiles do not provide clear evidence of a reproducible phase response associated with paleochannel occurrence. Future work could investigate whether additional phase filtering or averaging techniques improve the visibility of paleochannel-related signatures.

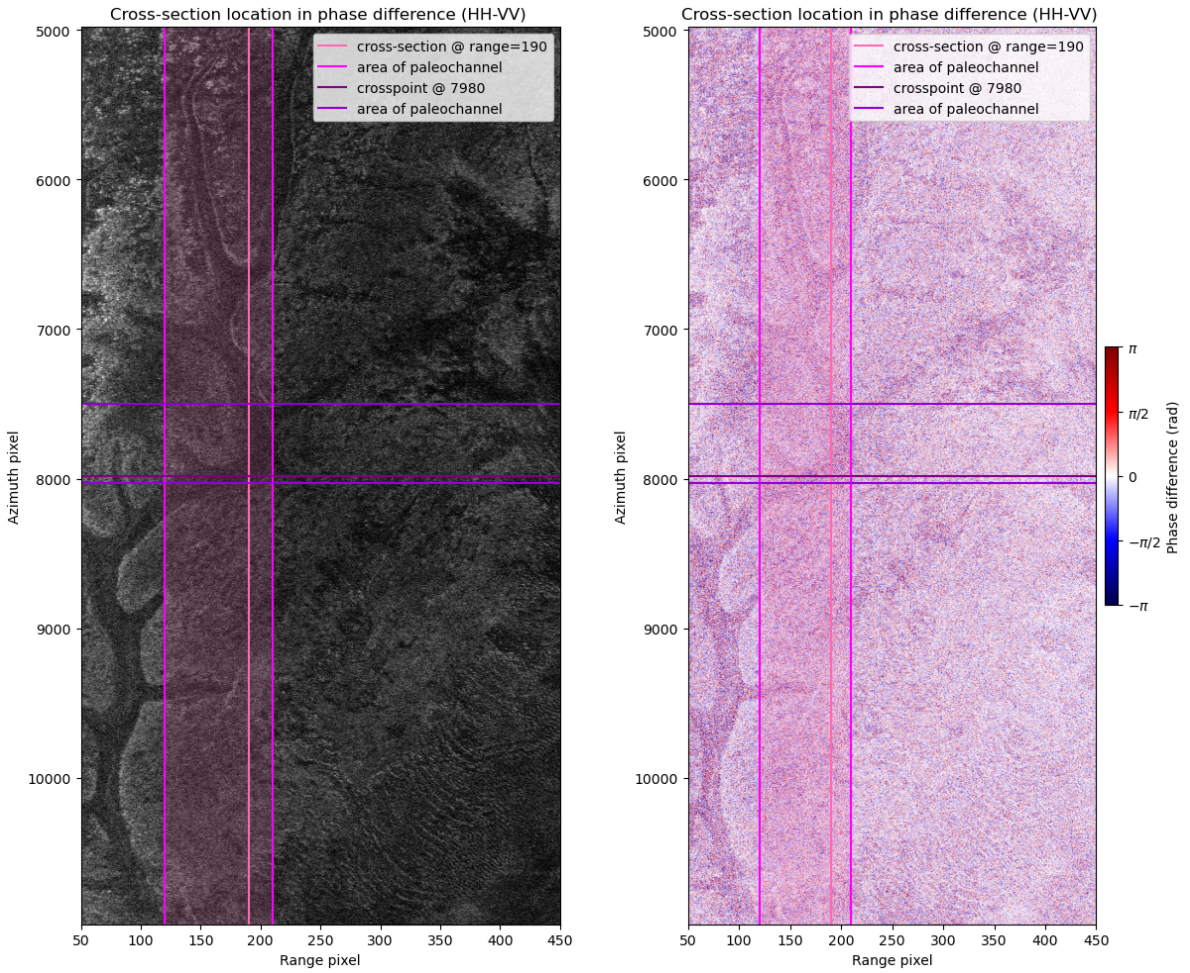

(a) Backscatter image.

(b) HH-VV phase-difference map.

Figure C.1: Location of the extracted HH-VV phase-difference cross-sections for the first Sahara region of interest. The highlighted regions indicate the mapped paleochannel extent and the profile locations used for analysis.

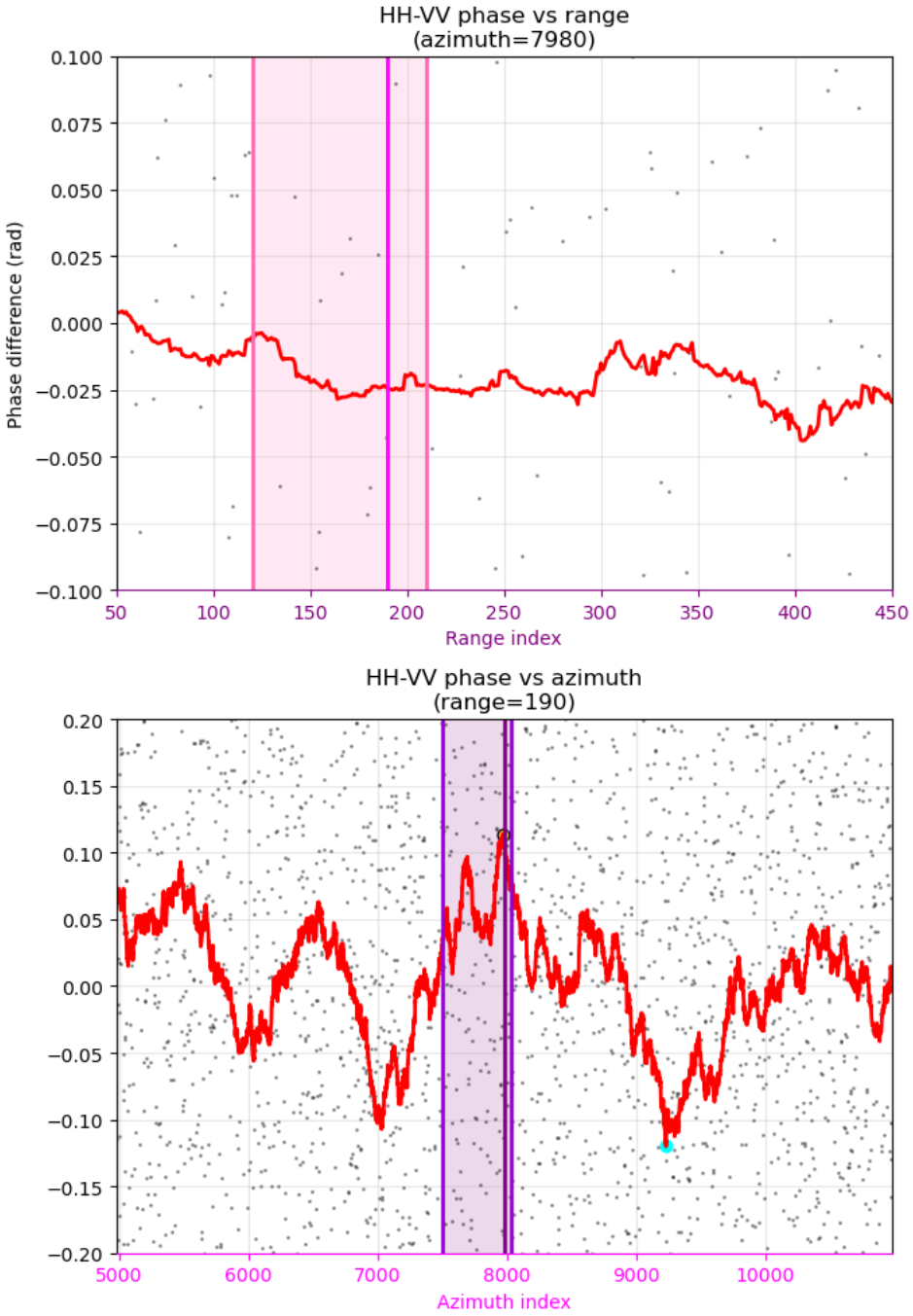

Figure C.2: Range and azimuth profiles of the HH-VV phase difference extracted through the paleochannel in the first Sahara region of interest. Shaded regions indicate the mapped channel extent.

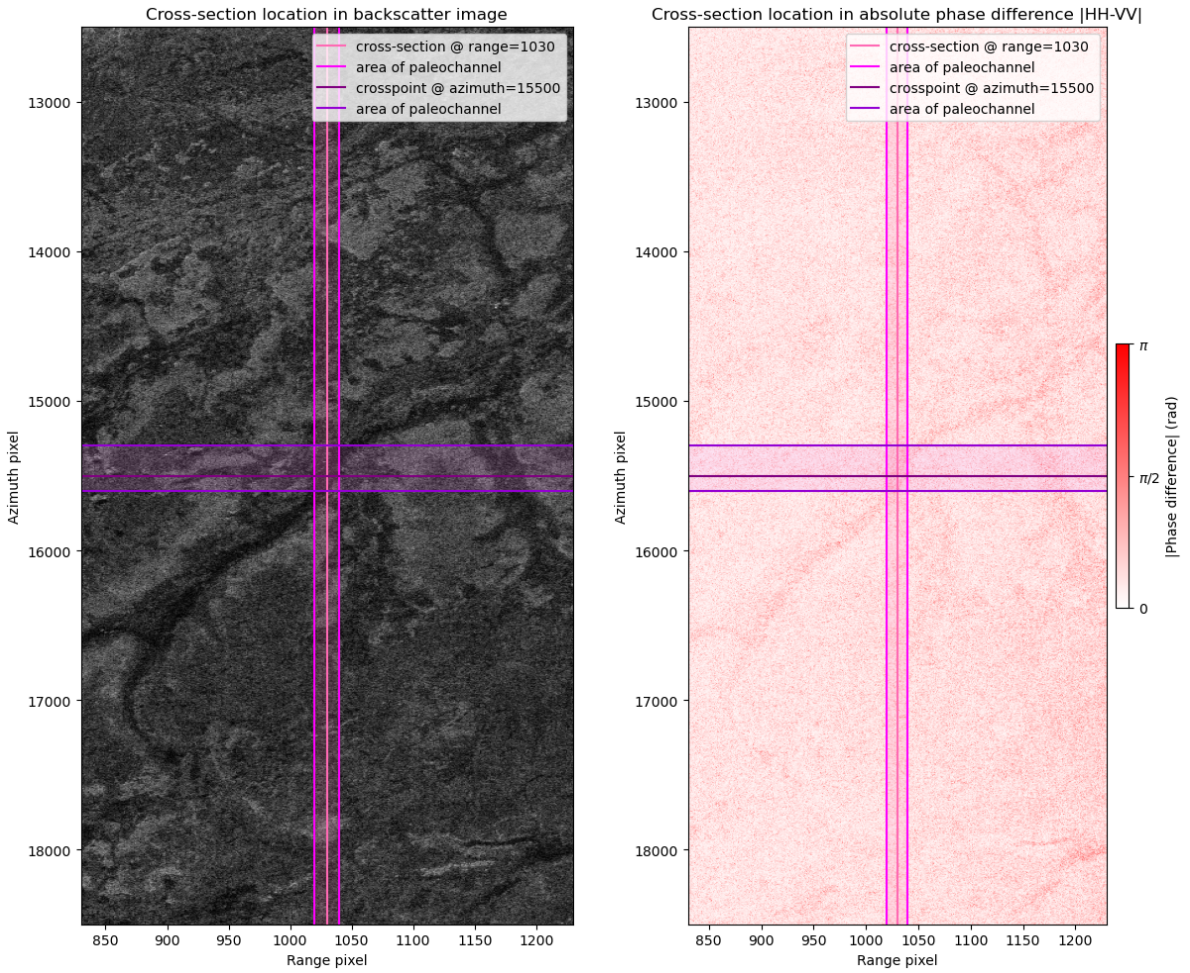

(a) Backscatter image.

(b) HH-VV phase-difference map.

Figure C.3: Location of the extracted HH-VV phase-difference cross-sections for the second Sahara region of interest. The highlighted regions indicate the mapped paleochannel extent and the profile locations used for analysis.

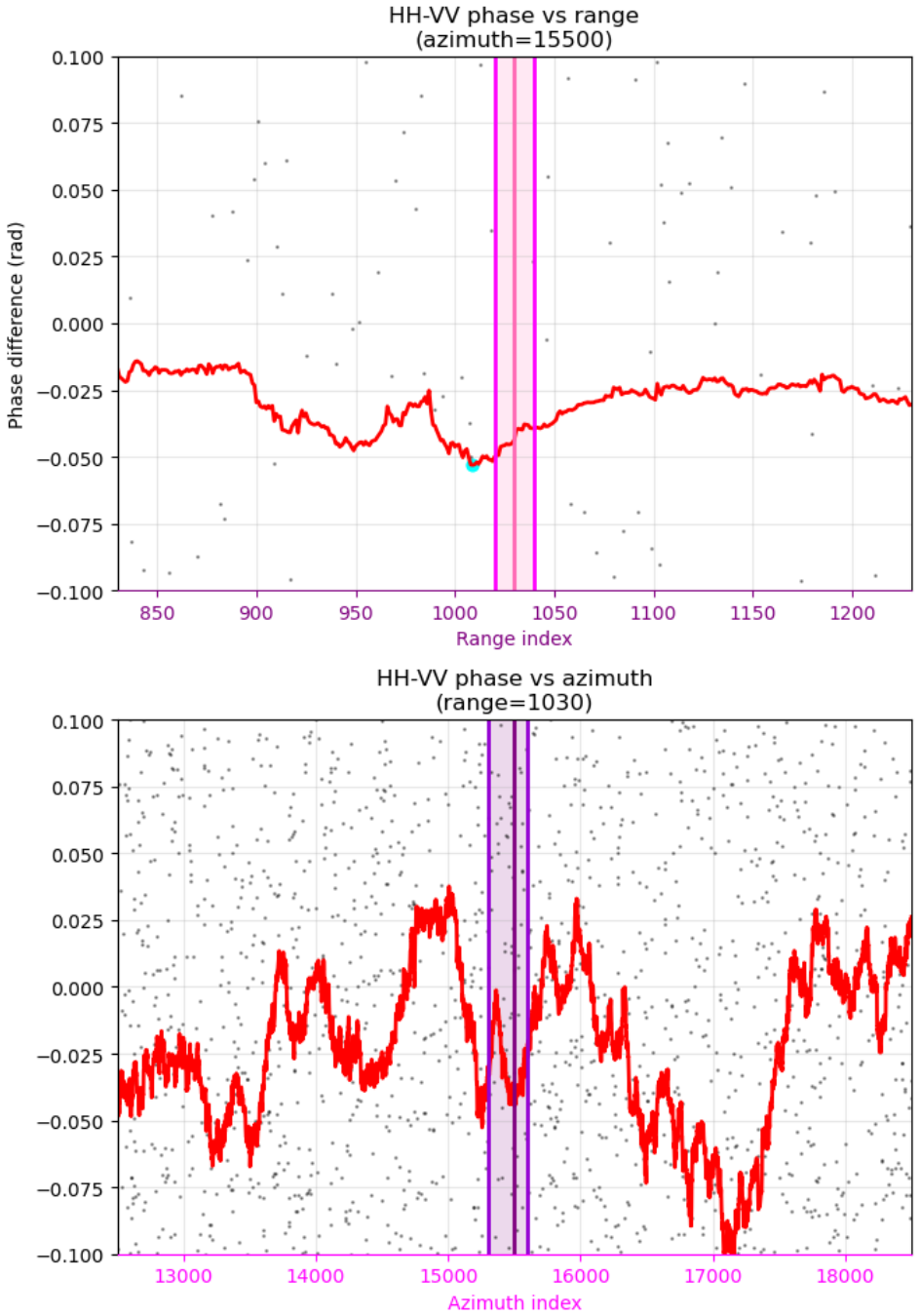

Figure C.4: Range and azimuth profiles of the HH-VV phase difference extracted through the paleochannel in the second Sahara region of interest. Shaded regions indicate the mapped channel extent.

To further evaluate the spatial behaviour of the HH-VV co-polarised phase difference, additional regions of interest (ROIs) were analysed using channel-background comparisons. For each ROI, a channel region and adjacent background regions were selected from the phase-difference image, and azimuth-averaged range profiles were extracted. The resulting profiles were examined to assess whether the mapped paleochannel exhibits a reproducible phase signature relative to the surrounding terrain.

Figure C.5 shows the selected channel and background regions used for the analysis, while Figure C.6 presents the corresponding azimuth-averaged HH-VV phase-difference profile.

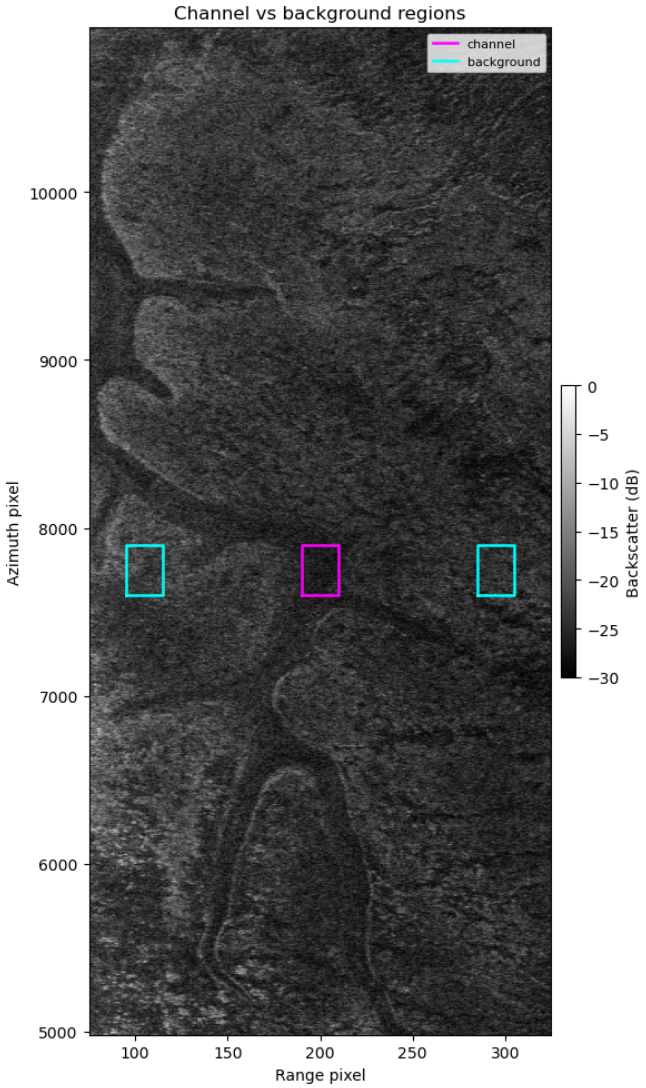

Figure C.5: Definition of the channel and background regions used for the HH-VV phase-difference analysis in the region of interest. The magenta box denotes the interpreted paleochannel region, while the cyan boxes denote neighbouring background regions used for comparison. The grayscale image corresponds to the stacked BIOMASS backscatter.

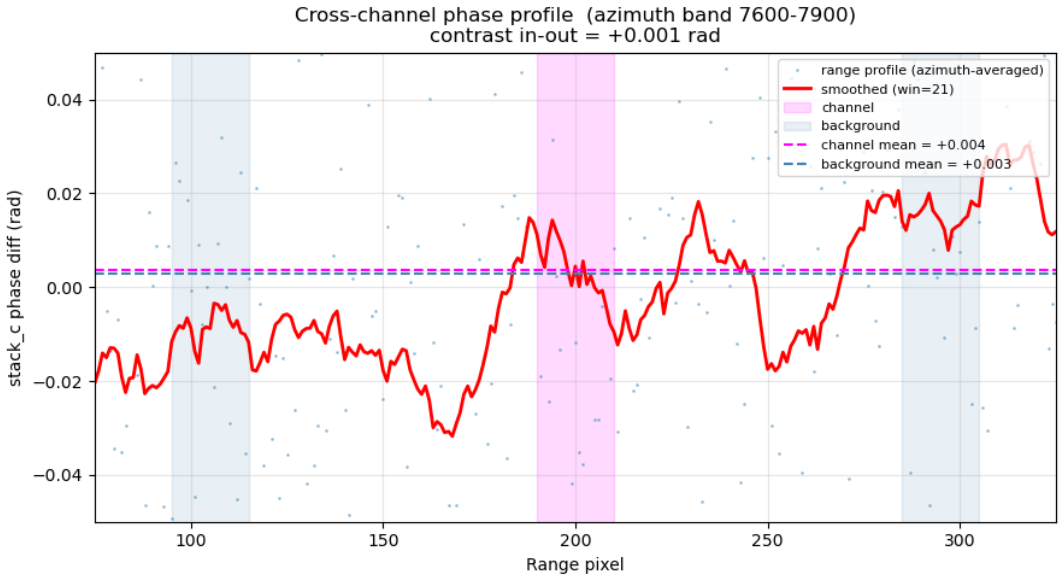

Figure C.6: Azimuth-averaged HH-VV phase-difference profile extracted across the region of interest. The magenta shaded region indicates the interpreted paleochannel extent, while the grey shaded regions indicate the background reference areas. Horizontal dashed lines denote the mean phase differences within the channel and background regions. Although local phase variations are present, the channel and background means differ by only approximately 0.001 rad, indicating no pronounced paleochannel-specific phase signature.

The extracted profile exhibits local fluctuations throughout the scene, but the mean phase difference within the paleochannel region differs only marginally from the surrounding background. Consistent with the results presented in Section 4.2, the profile does not reveal a distinct or reproducible paleochannel-specific HH-VV phase signature, despite the presence of broader geomorphological variability within the phase-difference image.

C.1.1. HV-VV phase difference analysis

To investigate whether cross-polarized phase information provides additional sensitivity to paleochannel features, the phase difference between the HV and VV channels was analysed. Figure C.7 presents the wrapped HV phase, wrapped VV phase, and the corresponding HV-VV phase difference for the Sahara study area.

Similar to the HH-VV analysis presented in the main text, the individual HV and VV phase images exhibit a predominantly speckled appearance and do not reveal readily interpretable spatial patterns. This behaviour is expected because the absolute phase of each channel is dominated by geometric and scattering-related contributions and is therefore difficult to interpret in isolation.

The HV-VV phase-difference image reveals substantially greater spatial variability than the HH-VV phase difference. Several geomorphic features visible in the amplitude imagery, including drainage-like and topographic structures, are expressed in the phase-difference product. In particular, some linear and dendritic features appear with enhanced contrast relative to the co-polarized phase-difference image.

However, the observed phase variations are accompanied by a noticeably noisier appearance. This behaviour is consistent with the lower backscatter intensity and reduced signal-to-noise ratio of the HV channel, which results in increased phase uncertainty. Consequently, it is difficult to distinguish between variability arising from genuine differences in scattering behaviour and variability introduced by measurement noise.

While the HV-VV phase difference demonstrates that cross-polarized phase information contains spatially coherent patterns that are related to surface morphology, no consistent paleochannel signature could be identified. Furthermore, because the subsequent coherence-based retrieval framework relies primarily on co-polarized observables, the HV-VV phase difference was not considered further in the

analysis.

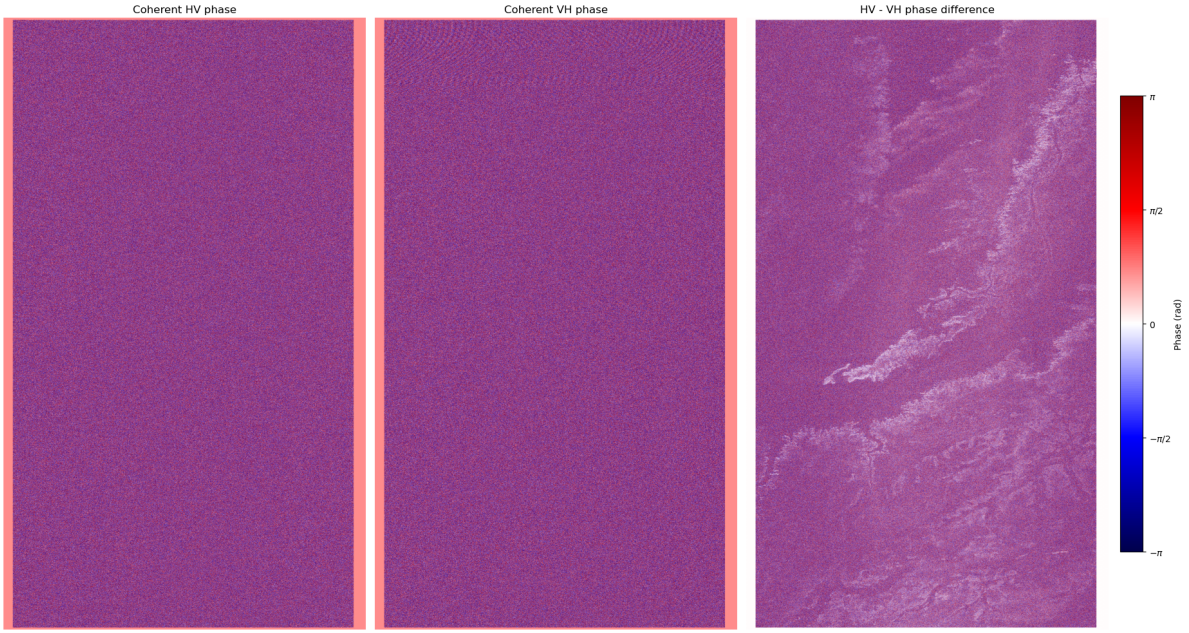

Figure C.7: Wrapped HV phase, wrapped VV phase, and the corresponding HV-VV phase difference for the Sahara study area. Phase values are displayed in the range $[-\pi, \pi]$ rad.

C.2. Additional Fresnel-I2EM retrieval diagnostics

Figure C.8 compares the intermediate roughness and vertical-wavenumber products generated by the Fresnel and I2EM inversion frameworks. The normalised roughness and RMS roughness retrievals exhibit noticeable model dependence, with systematic differences occurring throughout the scene and particularly along several geomorphological features. These differences reflect the alternative partitioning of the observed backscatter between dielectric and roughness contributions within the two forward models. In contrast, the dielectric-corrected vertical wavenumber products are more similar in both magnitude and spatial organisation. Although localized differences remain visible, the principal spatial patterns are preserved between models. This consistency contributes to the relatively strong agreement observed in the final effective-depth retrievals despite substantial differences in the intermediate roughness estimates.

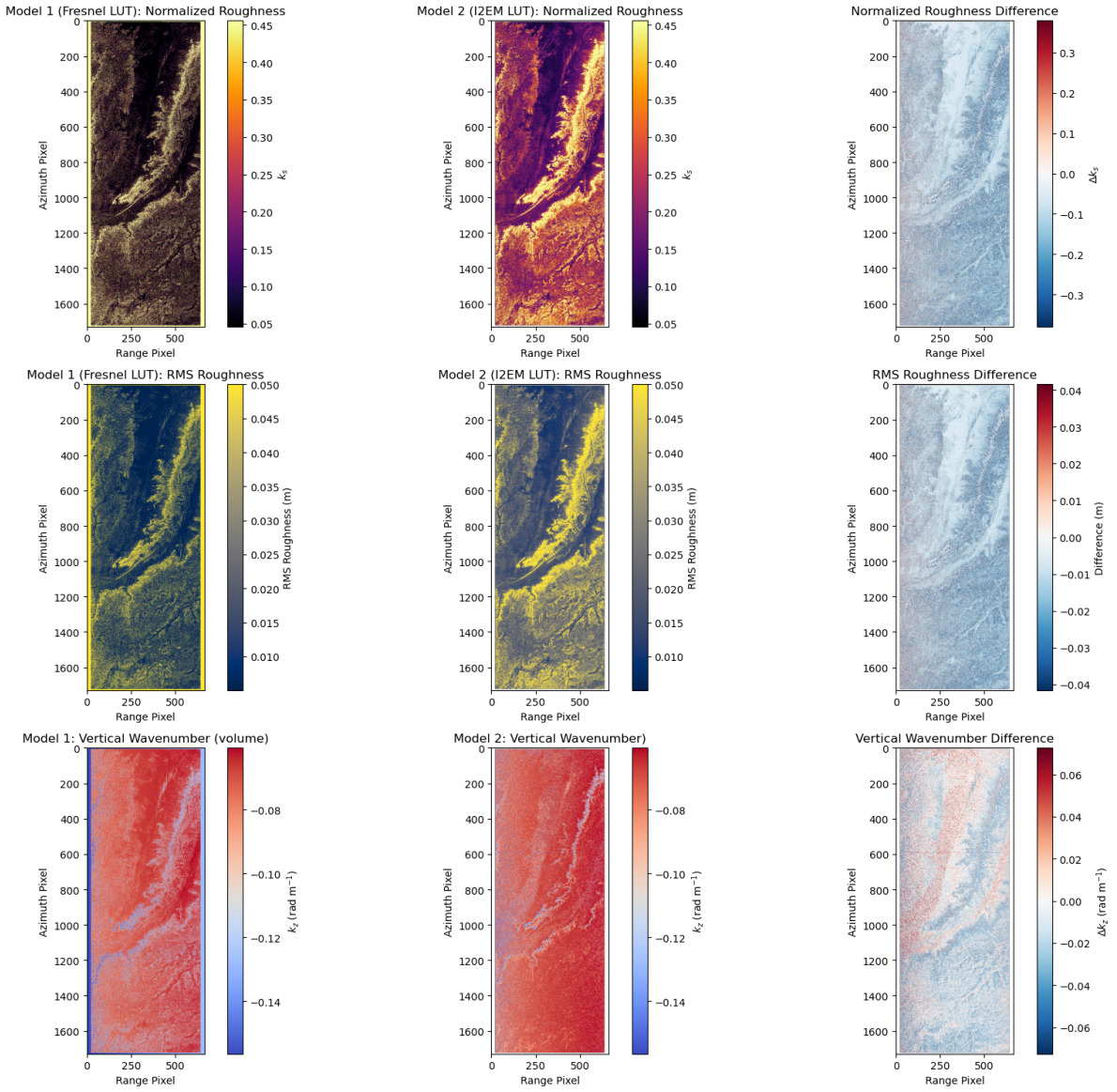

Figure C.8: Comparison of intermediate retrieval products derived using the Fresnel LUT (Model 1) and I2EM LUT (Model 2). Rows show normalised roughness (k_s), RMS roughness, and dielectric-corrected vertical wavenumber (k_z). The right column presents the corresponding difference maps (Model 1 minus Model 2). Substantial differences are observed in the retrieved roughness parameters, whereas the resulting vertical wavenumber products exhibit greater spatial consistency despite localized variations.

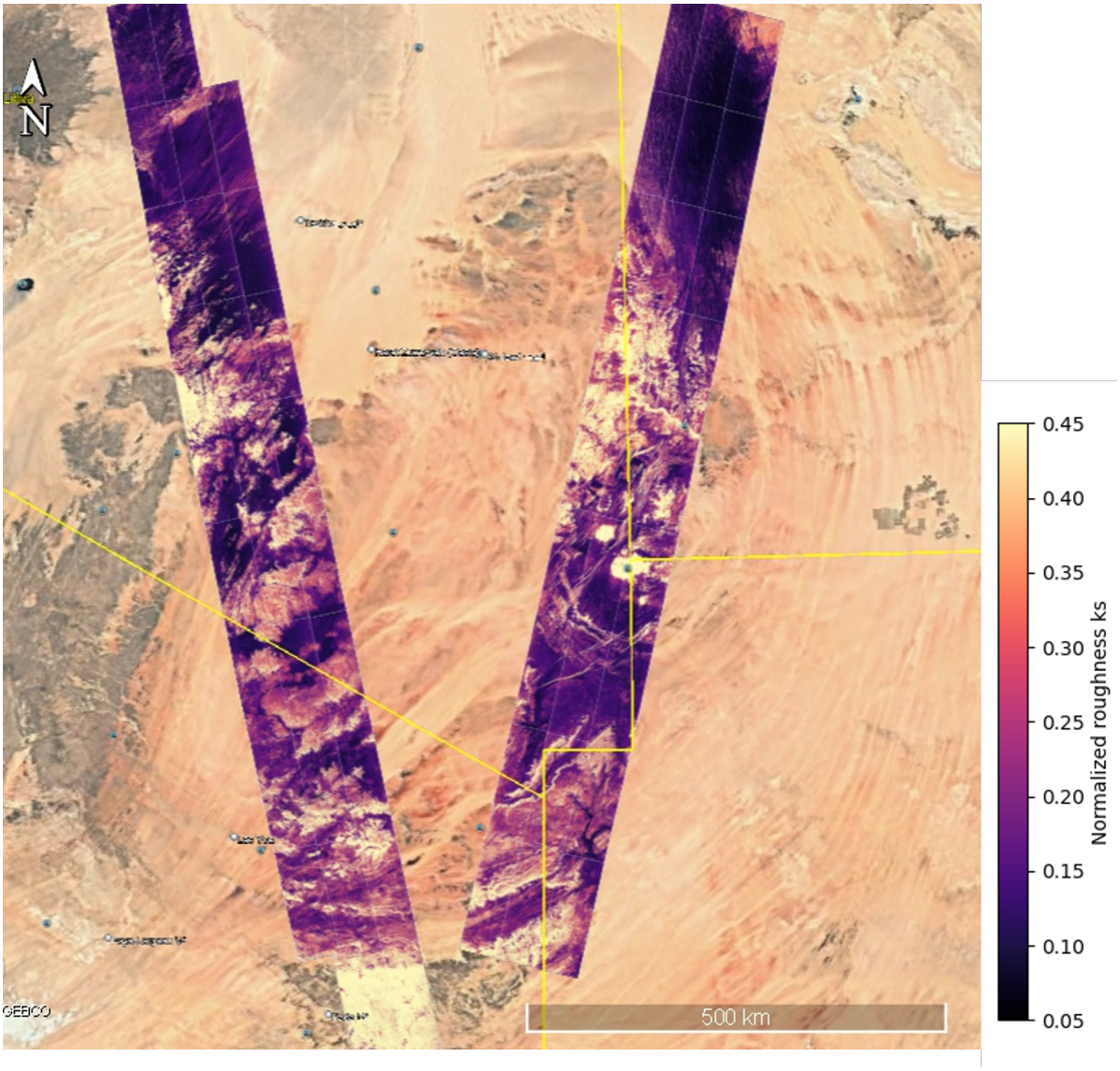

Figure C.9: Regional normalised surface roughness (k_s) retrieval derived from the I2EM inversion framework for the full BIOMASS coverage of the Kufrah Basin. The product exhibits substantial spatial variability across the regional mosaic and highlights broad geomorphological contrasts between homogeneous desert surfaces and more heterogeneous terrain. Several linear, branching, and localized anomalies remain visible across multiple BIOMASS frames, while scene-to-scene variations are also apparent throughout the regional swath.

C.3. Additional ascending-descending comparison diagnostics

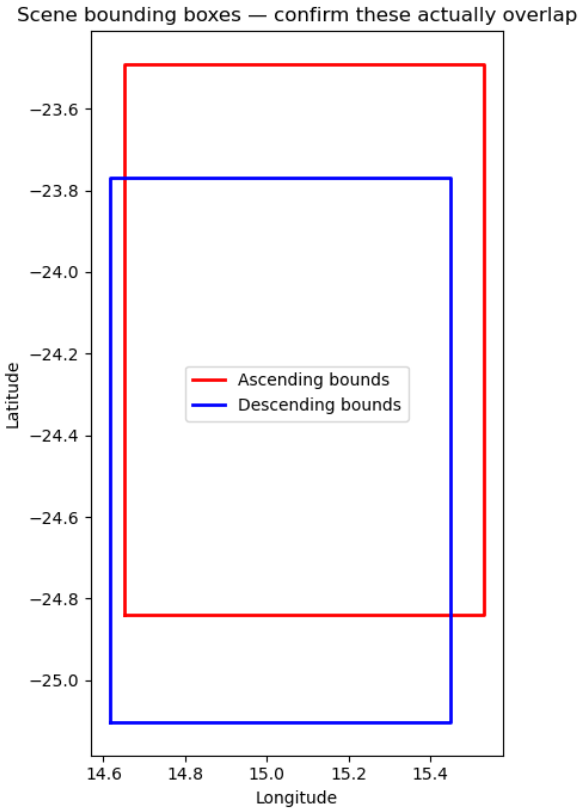

Figure C.10: Overlap between the ascending and descending BIOMASS acquisitions.

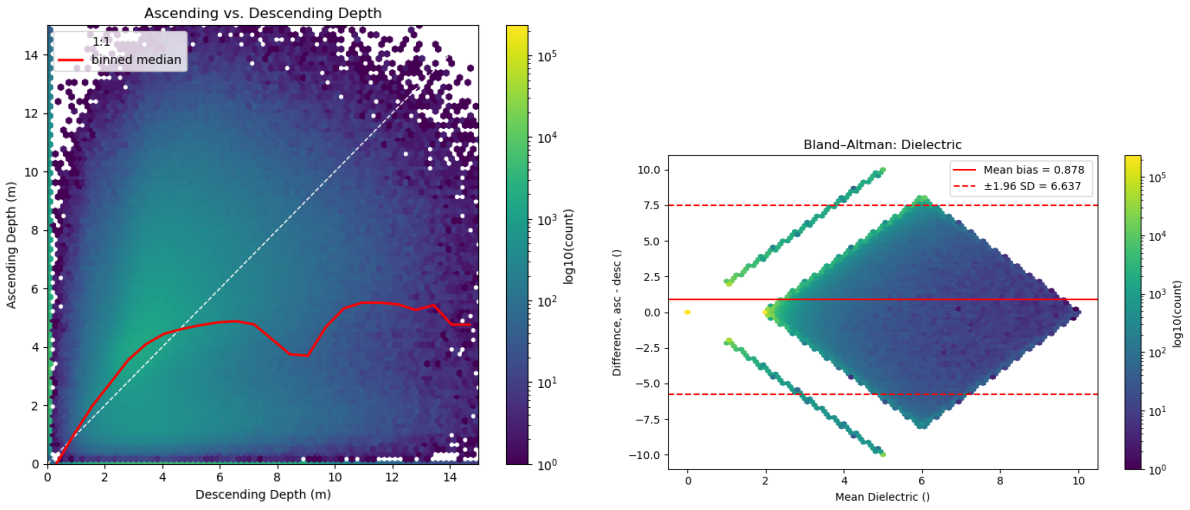

(a) Pixel-wise comparison

(b) Bland-Altman analysis

Figure C.11: Comparison of effective penetration depth retrievals derived from ascending and descending acquisitions.

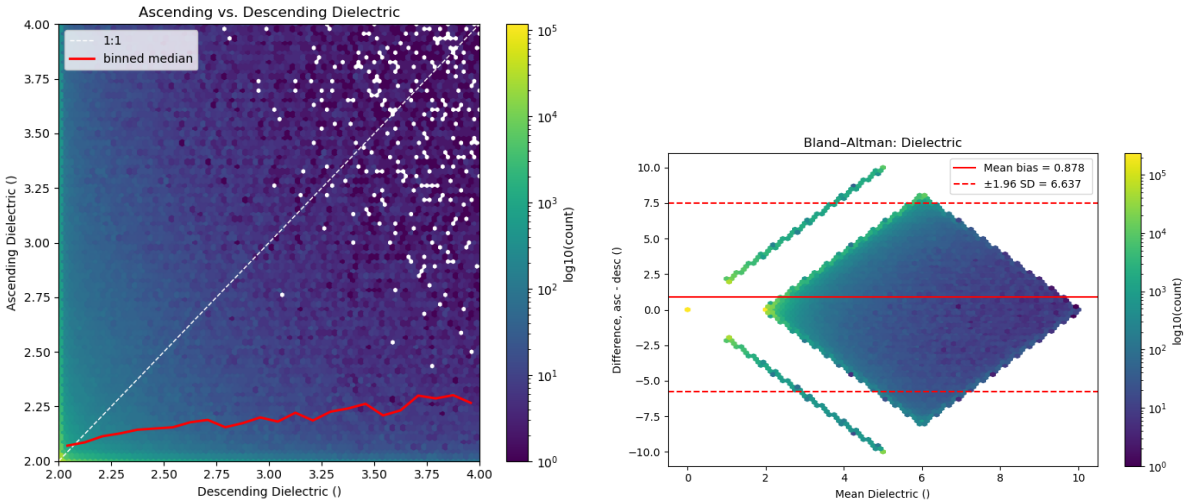

(a) Pixel-wise comparison

(b) Bland-Altman analysis

Figure C.12: Comparison of dielectric constant retrievals derived from ascending and descending acquisitions.

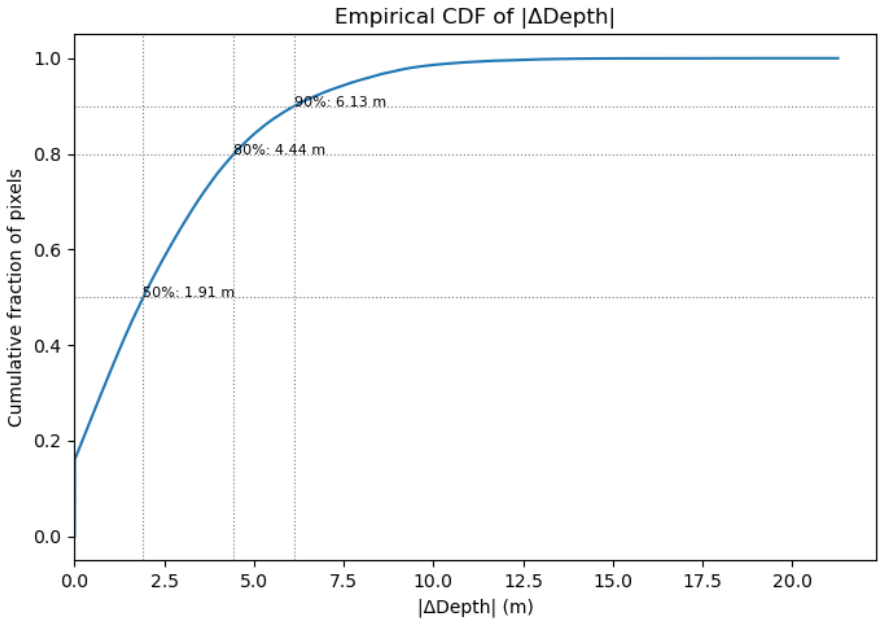

Figure C.13: Empirical cumulative distribution of absolute depth differences between ascending and descending retrievals.

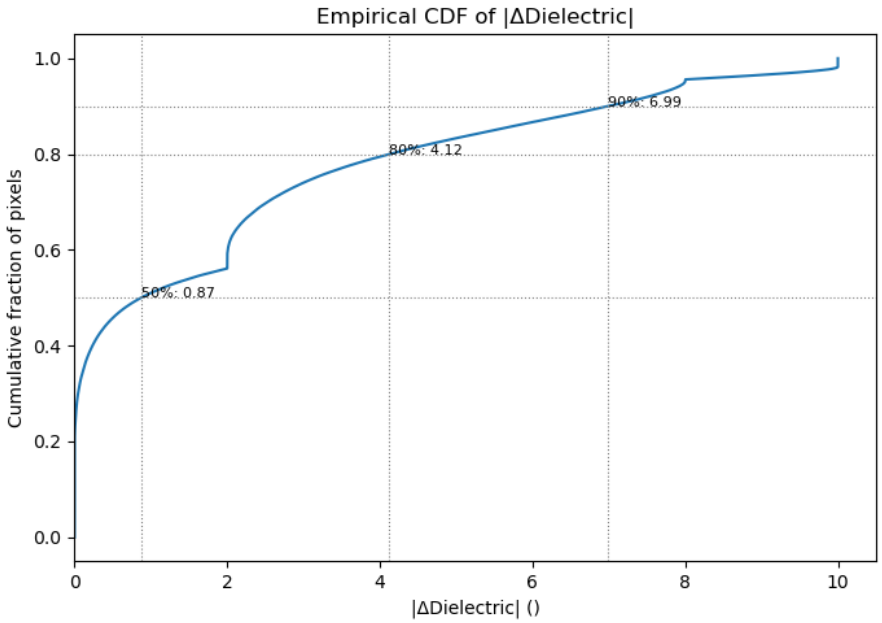

Figure C.14: Empirical cumulative distribution of absolute dielectric differences between ascending and descending retrievals.

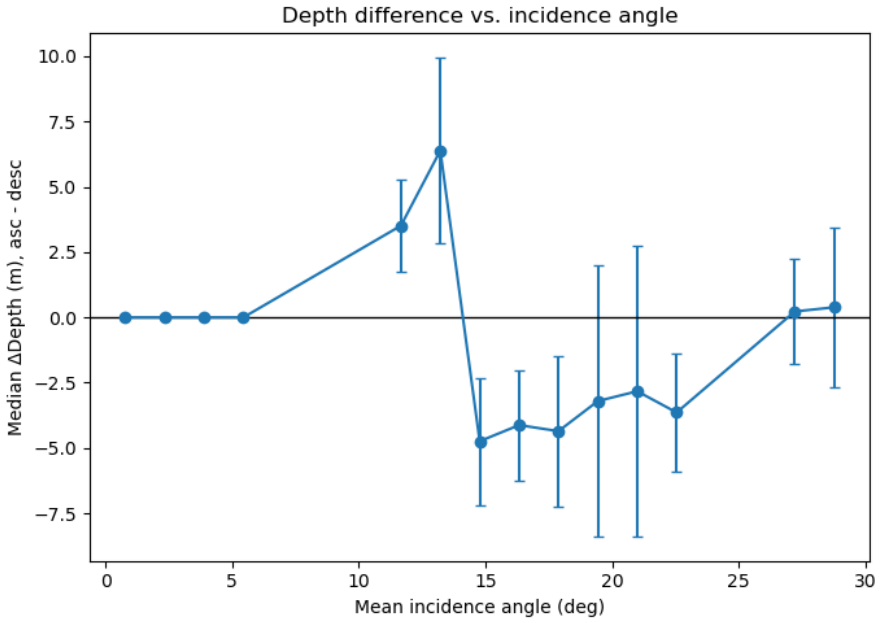

Figure C.15: Median depth difference as a function of incidence angle.

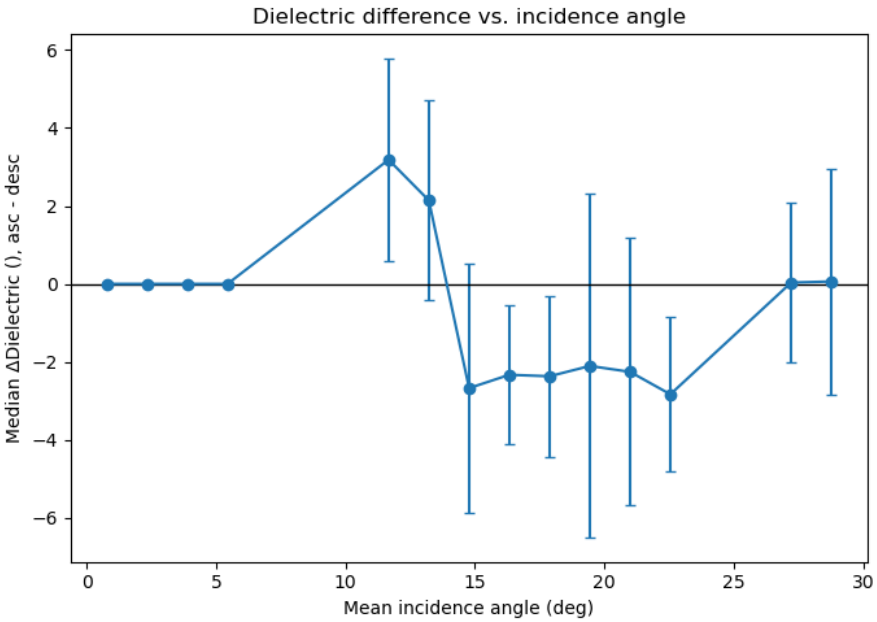

Figure C.16: Median dielectric difference as a function of incidence angle.

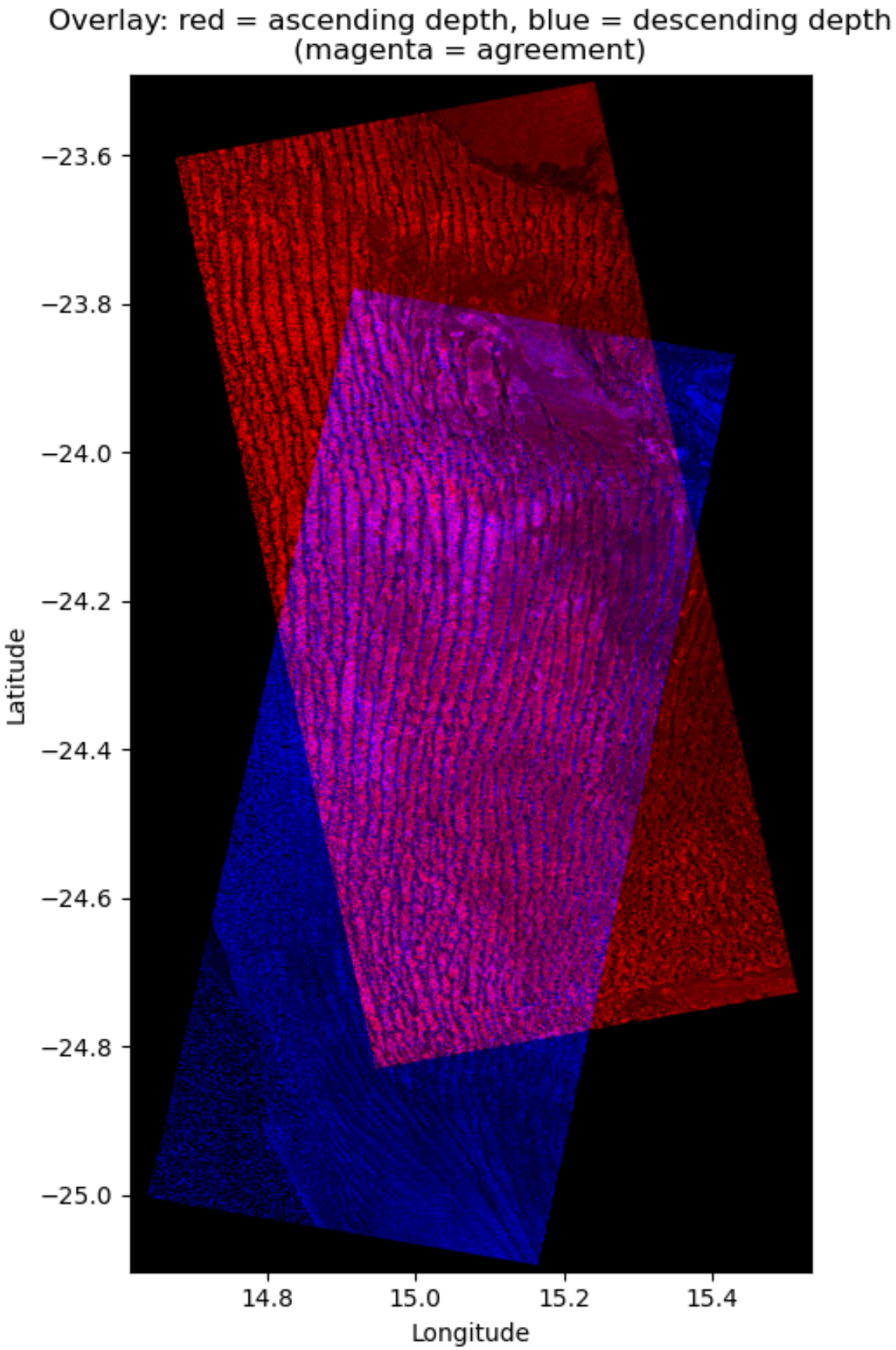

Figure C.17: Overlay of ascending and descending depth products within the overlapping region.

C.4. Validation model

C.4.1. Phase-profile response

To investigate the polarimetric response in greater detail, a profile was extracted through the centre of the synthetic paleochannel. Figure C.18 shows the resulting HH-VV phase difference together with the channel-membership function and prescribed reflector geometry.

The phase anomaly follows the spatial extent of the buried channel and reaches its maximum magnitude near the channel centre. The close correspondence between phase response and reflector position demonstrates the sensitivity of the simulated CPD observable to buried dielectric structure.

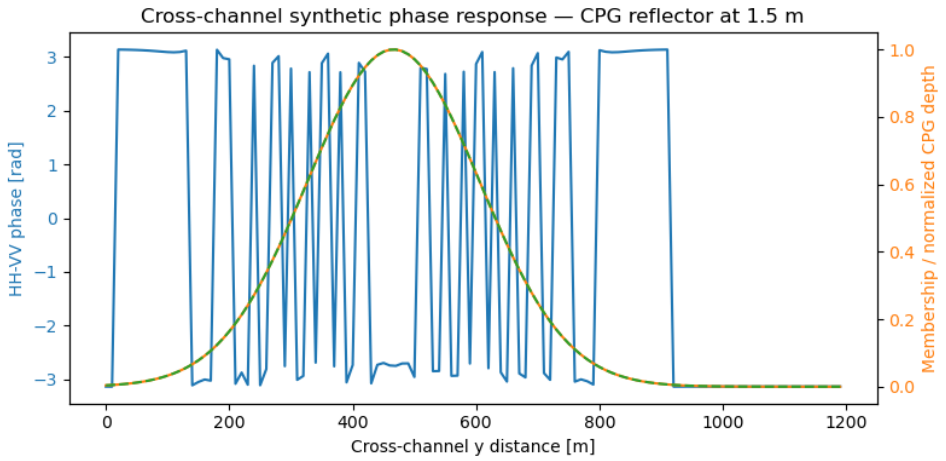

Figure C.18: Cross-channel profile through the centre of the synthetic paleochannel showing the HH-VV phase difference together with the normalised channel-membership function and buried-reflector geometry.

C.4.2. Monte Carlo retrieval statistics

Monte Carlo uncertainty propagation was performed by perturbing acquisition geometry, coherence, dielectric properties, and simulated measurement noise. Figure C.19 presents the resulting mean and standard deviation maps for dielectric constant, moisture content, and buried-reflector depth.

The mean retrievals reproduce the prescribed channel geometry in all variables. Standard deviations remain relatively low within the homogeneous background and increase within the channel region, where dielectric contrasts are strongest and retrieval sensitivity is greatest.

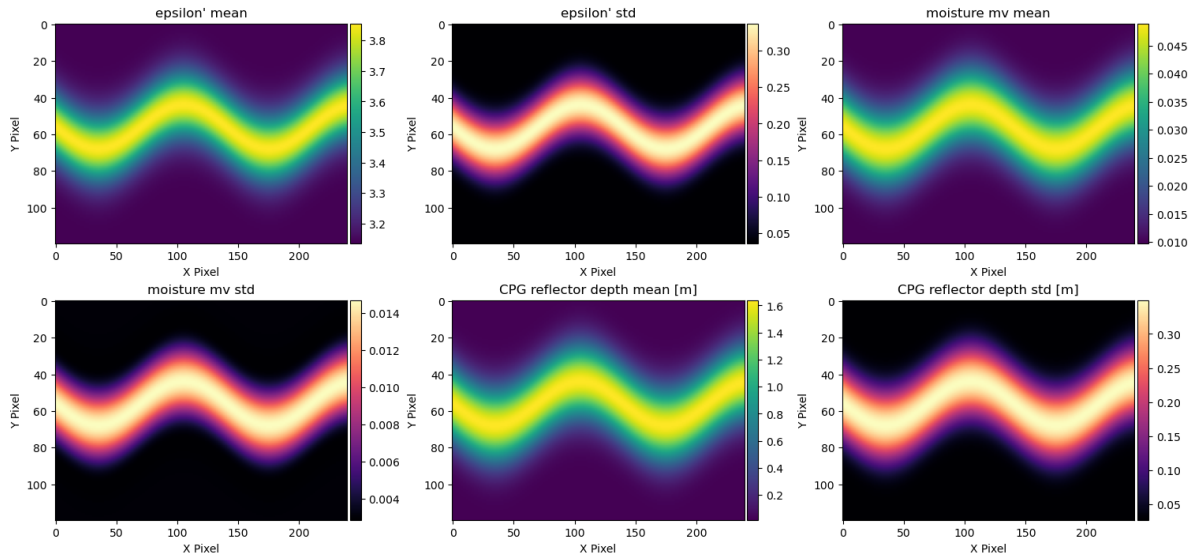

Figure C.19: Monte Carlo mean and standard-deviation maps for dielectric constant, moisture content, and buried-reflector depth obtained from repeated perturbations of acquisition and environmental parameters.

C.4.3. Profile-based retrieval assessment

Figure C.20 compares the nominal retrieval with the Monte Carlo ensemble along a profile crossing the centre of the channel.

All three retrieved variables reproduce the prescribed paleochannel anomaly. The Monte Carlo mean remains close to the nominal solution throughout the profile, while uncertainty increases within the channel where parameter contrasts are largest. Maximum dielectric constant, moisture content, and burial depth occur near the centre of the reflector and decrease toward background values away from the channel.

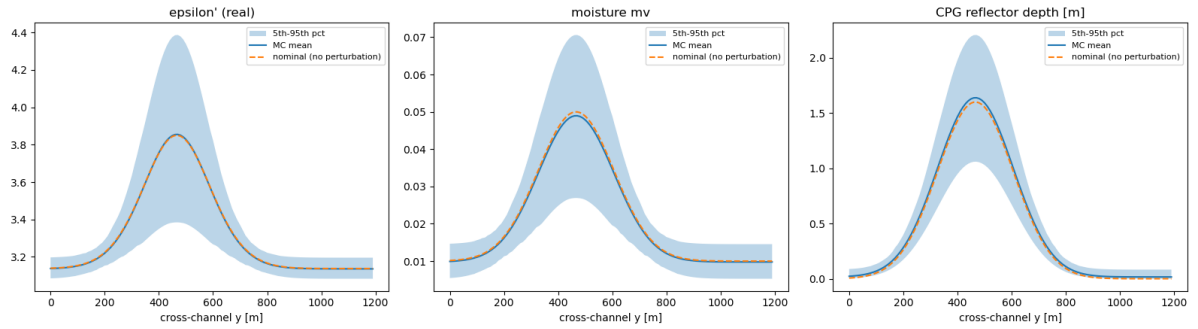

Figure C.20: Cross-channel profiles showing Monte Carlo mean estimates, nominal solutions, and 5th-95th percentile uncertainty bounds for dielectric constant, moisture content, and buried-reflector depth.

Effective depth-retrieval uncertainty

Figure C.21 shows the coherence-derived depth retrieval together with the uncertainty bounds obtained from Monte Carlo analysis.

The recovered depth profile follows the prescribed reflector geometry and reproduces the location of maximum burial depth within the channel centre. Retrieval uncertainty increases with depth, leading to broader confidence intervals for deeper portions of the reflector.

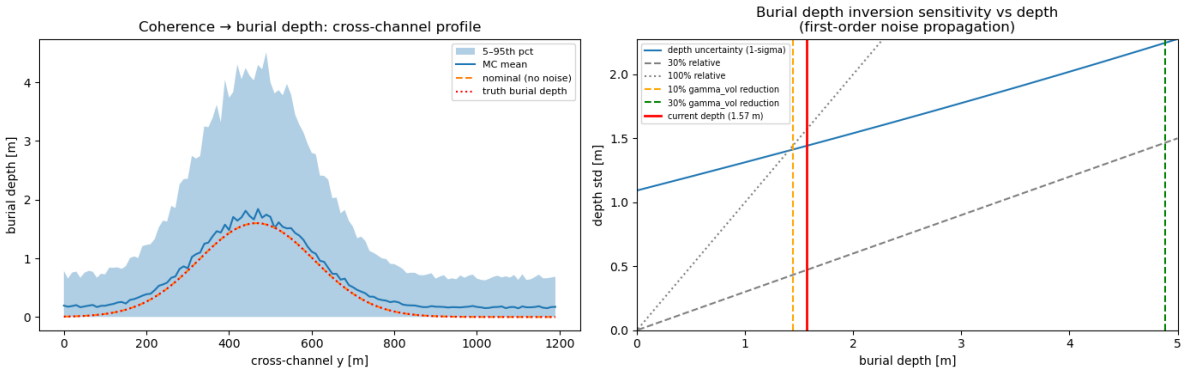

Figure C.21: Coherence-derived burial-depth estimation. The left panel shows the retrieved depth profile together with Monte Carlo uncertainty bounds and the prescribed burial depth. The right panel illustrates the predicted relationship between burial depth and retrieval uncertainty obtained from first-order noise propagation.

D

Methods Evaluated During Development and Future Research Directions

Several alternative retrieval frameworks were developed and evaluated during the course of this research before the final methodology presented in Chapter 3 was adopted. These approaches formed part of the iterative development process and contributed significantly to the understanding of how dielectric properties, moisture content, coherence behaviour, and subsurface scattering influence P-band SAR observations in arid environments.

The methods described in this appendix were implemented and tested but were ultimately excluded from the final retrieval chain. In most cases, this decision was motivated by a combination of limited input data, insufficient physical constraints, uncertainty in model calibration at P-band frequencies, or instability of the inversion process. Nevertheless, these approaches remain scientifically relevant and may provide promising directions for future work if additional calibration data, field observations, or polarimetric products become available.

The purpose of documenting these methods is therefore twofold. First, it provides a transparent record of the methodological evolution of the thesis. Second, it identifies potential research directions that may become feasible as BIOMASS datasets mature and additional validation measurements become available.

D.1. Empirical HV-based moisture retrieval using the Oh et al. (1992) Model

D.1.1. Original model

One of the earliest retrieval approaches investigated in this thesis was based on the semi-empirical soil moisture inversion model of Oh et al. (1992). The original model was developed from extensive scatterometer observations over bare agricultural soils and relates radar backscatter to surface roughness, incidence angle, and volumetric soil moisture through a series of empirical relationships.

The full formulation jointly exploits co-polarized and cross-polarized scattering ratios,

$$p = \frac{\sigma^0_{hh}}{\sigma^0_{vv}}, \tag{D.1}$$

and

$$q = \frac{\sigma^0_{hv}}{\sigma^0_{vv}}, \tag{D.2}$$

together with the observed cross-polarized backscatter coefficient

$$\sigma^0_{hv}, \tag{D.3}$$

to retrieve both volumetric moisture content m_v and surface roughness ks simultaneously.

The model was attractive because it provided a direct link between radar observations and soil moisture while avoiding the explicit use of dielectric mixing models.

D.1.2. Implemented simplification

The complete polarimetric inversion could not be applied within the available BIOMASS processing chain. Consequently, a simplified implementation was developed in which only the cross-polarized backscatter component was used:

$$\sigma^0_{HV} = 0.11 m_v^{0.7} \cos^{2.2}\theta \left[1 - \exp\left(-0.32 k_s^{1.8}\right)\right]. \tag{D.4}$$

A roughness proxy derived from the SAR image was supplied externally, reducing the inversion to a single unknown parameter (m_v).

The retrieved moisture values were subsequently converted into dielectric constants using the empirical relationship of Topp et al. (1980),

$$\varepsilon_r = 3.03 + 9.3 m_v + 146 m_v^2 - 76.7 m_v^3. \tag{D.5}$$

The resulting dielectric estimates were then used in subsequent penetration-depth calculations.

D.1.3. Reasons for exclusion

Initial investigations demonstrated that the retrieval produced physically plausible moisture patterns; however, several major limitations became apparent.

First, the Oh model was originally calibrated using L-band, C-band, and X-band measurements over agricultural test sites. No validated coefficient set exists for P-band observations. Application of the model therefore required extrapolation far beyond its calibration domain.

Second, the retrieved moisture fields were highly sensitive to the adopted roughness proxy. Because no independent roughness measurements were available for either the Sahara or Namib study sites, uncertainty in surface roughness propagated directly into uncertainty in moisture estimates.

Third, the model assumes that observed scattering originates primarily from a surface interaction process. In contrast, one of the principal motivations of this thesis is that P-band signals may contain significant contributions from subsurface interfaces and buried paleochannel structures. Consequently, moisture retrievals derived purely from surface-scattering assumptions could not be uniquely interpreted.

Finally, the resulting dielectric estimates frequently acted more as relative spatial indicators than as physically defensible moisture measurements. While useful for exploratory analysis, they could not be sufficiently validated for inclusion in the final workflow.

D.1.4. Future research directions

The methodology could potentially be revisited if future BIOMASS datasets provide:

1. independently calibrated P-band roughness measurements,
2. field measurements of volumetric soil moisture,
3. polarimetric observations acquired alongside in-situ sampling,

4. dedicated P-band calibration campaigns over arid soils.

Under such circumstances, P-band-specific empirical coefficients could be developed, potentially making the approach considerably more robust.

D.2. AIEM-Mironov physical moisture retrieval framework

D.2.1. Original model

To address the empirical nature of the Oh inversion, a second retrieval framework was developed based on explicit electromagnetic scattering physics.

Surface scattering was represented using the Advanced Integral Equation Model (AIEM), an extension of the Integral Equation Model developed by K.-S. Chen et al. (2000), Fung (1994), and Fung et al. (1992). In its complete form, AIEM predicts radar backscatter as a function of dielectric properties, RMS roughness height, roughness correlation length, incidence angle, wavelength, and polarization.

The dielectric properties required by AIEM were obtained from the Generalized Refractive Mixing Dielectric Model (GRMDM) of Mironov et al. (2004, 2009), which relates volumetric soil moisture to complex dielectric permittivity through a physically based refractive-index mixing formulation.

The theoretical forward chain was therefore:

$$m_v \rightarrow \varepsilon^* \rightarrow \sigma^0. \tag{D.6}$$

In principle, this framework is substantially more physical than the Oh model because both dielectric behaviour and radar scattering are represented explicitly.

D.2.2. Implemented simplification

Although the full AIEM–Mironov framework was initially investigated, several simplifications were required to obtain a numerically stable implementation.

The full Mironov dielectric model was replaced by a simplified polynomial approximation,

$$\varepsilon' = \varepsilon_{\mathrm{dry}} + a_1 m_v + a_2 m_v^2, \tag{D.7}$$

which approximated the moisture–dielectric relationship while avoiding the complexity of bound-water and free-water parameterization.

Similarly, AIEM was reduced to a simplified roughness-activation formulation,

$$G_r(k_s) = 1 - \exp\left(-\beta k_s\right), \tag{D.8}$$

which retained the qualitative influence of roughness without requiring the evaluation of multiple-scattering integrals.

A lookup-table inversion was then performed to estimate moisture from observed backscatter.

D.2.3. Reasons for exclusion

Despite being more physically motivated than the Oh approach, the AIEM–Mironov workflow ultimately suffered from a much larger number of unconstrained parameters.

The first difficulty was the absence of measured roughness statistics. AIEM requires both RMS height and correlation length, neither of which were available for the study areas. A backscatter-derived roughness proxy was therefore substituted, partially defeating the purpose of introducing a physically rigorous roughness model.

A second limitation was the absence of spatially resolved soil texture information. The Mironov model depends on clay content, porosity, and mineral composition. These quantities are poorly constrained in remote desert environments and can vary substantially over short distances.

The inversion also exhibited equifinality. Multiple combinations of dielectric constant, roughness, and calibration parameters frequently reproduced similar backscatter values. Consequently, physically different solutions often produced nearly identical inversion results.

Most importantly, the computational complexity of the framework was difficult to justify given the available observations. The increase in physical realism was accompanied by a corresponding increase in parameter uncertainty, leading to a more complicated model without a demonstrable improvement in retrieval reliability.

For these reasons, the final methodology adopted a more transparent dielectric inversion strategy based on Fresnel reflectivity and lookup-table matching.

D.2.4. Future research directions

Future developments could revisit this framework if:

1. field measurements of RMS surface roughness become available,
2. roughness correlation lengths can be estimated independently,
3. representative sediment samples are collected for laboratory dielectric characterisation,
4. texture maps and porosity estimates are available for the study areas,
5. BIOMASS observations can be calibrated against dedicated P-band field experiments.

Under these conditions, AIEM–Mironov retrievals could provide a more physically rigorous estimate of dielectric properties than the simplified methodology adopted in this thesis.

D.3. Decomposition-constrained multilayer coherence inversion

D.3.1. Original concept

One of the most complex retrieval strategies developed during this research was a multilayer coherence inversion framework designed to explicitly separate different scattering mechanisms contributing to the observed coherence.

Rather than treating coherence as a direct indicator of depth, the observed coherence was modelled as a combination of:

- surface scattering,
- shallow-volume scattering,
- deeper subsurface scattering.

The model was formulated as

$$\gamma_{\mathrm{model}} = \mu_s + (1-\mu_s)\left[\mu_v e^{-\frac{1}{2}(k_z L_v)^2} + (1-\mu_v)e^{-\frac{1}{2}(k_z L_b)^2}\right], \tag{D.9}$$

where μ_s and μ_v describe the relative contributions of surface and shallow-volume scattering.

These parameters were intended to be constrained using entropy-alpha decomposition and Freeman-Durden/Yamaguchi decomposition products.

D.3.2. Implemented approach

Several prototype implementations were developed in which decomposition-derived surface and volume fractions were incorporated as inversion priors.

The goal was to suppress non-penetrating scattering contributions before estimating the deeper coherence-producing depth scale L_b.

Analytical inversion formulas were derived and implemented, allowing the subsurface depth parameter to be solved directly from the observed coherence.

D.3.3. Reasons for exclusion

Although conceptually appealing, the approach ultimately proved underconstrained.

The primary difficulty was that stable decomposition products require full quad-polarimetric processing and sufficient independent looks. While the BIOMASS datasets contained the required polarizations, a consistent decomposition chain was not available alongside the coherence products ultimately used for depth estimation.

A second problem was the ambiguity of decomposition outputs themselves. Entropy, alpha angle, and scattering powers do not directly measure depth. Instead, they provide indirect information about scattering mechanisms. Translating these quantities into physically meaningful surface and volume fractions introduced another layer of assumptions.

The inversion therefore evolved into a highly parameterised problem in which multiple uncertain quantities influenced the final depth estimate.

Although feasible in principle, the complexity of the approach could not be justified within the scope of this thesis.

D.3.4. Future research directions

This remains one of the most promising future developments identified during the project.

Future implementation would require:

1. full quad-polarimetric BIOMASS processing,
2. consistent decomposition products,
3. multilooked covariance matrices,
4. independent validation of decomposition-derived scattering fractions,
5. fully integrated polarimetric-interferometric processing.

Such an approach could eventually provide a physically richer separation of surface and subsurface scattering contributions than the single-component coherence inversion adopted in the final methodology.

E

Automated topographic modeling using the D8 algorithm

Although paleochannels are frequently buried beneath aeolian sand and disconnected from present-day surface hydrology, many retain a relict drainage organisation that reflects former flow-routing patterns (Howard, 1994; Jenson & Domingue, 1988). Consequently, topographic flow-routing derived from modern Digital Elevation Models (DEMs) can serve as a valuable, independent geomorphic prior for paleochannel detection and validation. In this thesis, a raster-based DEM is processed using the deterministic eight-node (D8) algorithm to estimate likely drainage pathways and stream-network structure, providing contextual information against which radar-derived subsurface indicators can be assessed (O'Callaghan & Mark, 1984).

Prior to flow-routing, DEM pre-processing is required to ensure topological continuity. Raw DEMs commonly contain artificial depressions caused by measurement noise, interpolation artefacts, or void-filling procedures. These spurious sinks interrupt downslope connectivity and lead to erroneous drainage patterns if left uncorrected (Jenson & Domingue, 1988; Planchon & Darboux, 2001). Let $z(i, j)$ denote the elevation at grid cell (i, j). A depression-filled surface $\tilde{z}(i, j)$ is computed such that each interior cell possesses at least one downslope outlet draining towards the domain boundary or a valid edge cell, thereby enforcing global drainage continuity while preserving large-scale topographic structure.

Flow direction is subsequently computed using the D8 scheme, which assigns drainage from each cell to exactly one of its eight neighbouring cells (N, NE, E, SE, S, SW, W, NW) by selecting the neighbour with the maximum downslope gradient (O'Callaghan & Mark, 1984). For a neighbouring cell k, the local downslope gradient is defined as

$$s_k(i, j) = \frac{\tilde{z}(i, j) - \tilde{z}_k}{d_k}, \tag{E.1}$$

where $\tilde{z}_k$ denotes the elevation of neighbour k and d_k is the planimetric distance between cell centres, given by

$$d_k = \begin{cases} \Delta, & \text{for orthogonal neighbours,} \\ \sqrt{2}\,\Delta, & \text{for diagonal neighbours.} \end{cases} \tag{E.2}$$

The flow receiver for cell (i, j) is then selected as

$$k^*(i, j) = \arg\max_k \; s_k(i, j), \tag{E.3}$$

with the constraint

$$s_{k^*} > 0. \tag{E.4}$$

If no positive downslope gradient exists following sink filling, the cell is treated as a residual flat or locally undrained element. The resulting flow-direction grid defines a directed acyclic graph representing potential drainage pathways across the landscape.

Flow accumulation is derived by traversing this directed D8 network and counting the total number of upslope cells contributing drainage through each grid cell (Tarboton, 1997). Let $A(i, j)$ denote the accumulation at cell (i, j) and $U(i, j)$ the set of upstream donor cells draining into it. Accumulation is computed recursively as

$$A(i,j) = 1 + \sum_{(m,n)\in U(i,j)} A(m,n). \tag{E.5}$$

Large values of $A(i, j)$ correspond to zones of convergent flow and are interpreted as likely drainage axes, even in the absence of observable surface channels.

To extract candidate stream networks, the flow accumulation field is thresholded to produce binary channel masks:

$$S_T(i,j) = \begin{cases} 1, & A(i,j) \geq T, \\ 0, & A(i,j) < T, \end{cases} \tag{E.6}$$

where T is a user-defined accumulation threshold (Montgomery & Foufoula-Georgiou, 1994). Because paleochannel systems may range from fine tributary networks to large regional trunk channels, multiple thresholds are evaluated (e.g. $T = 10^2$, 5×10^2, 2×10^3, and 10^4 contributing cells). Lower thresholds highlight dense minor drainage patterns, whereas higher thresholds isolate persistent, large-scale drainage elements that are more likely to represent regional paleohydrological structures.

The D8-derived flow accumulation fields and stream masks are not interpreted as evidence of present-day hydrological activity. Instead, they are used strictly as a geomorphic prior that complements radar-based subsurface observations. In arid and relict terrains, spatial correspondence between D8-inferred drainage pathways and SAR-derived subsurface anomalies strengthens the plausibility of paleochannel interpretations. Conversely, systematic mismatches may indicate deeply buried channels that are decoupled from modern surface relief or modified by subsequent aeolian deposition, tectonic deformation, or erosion (Ghoneim & El-Baz, 2007; Paillou et al., 2009). In this manner, D8-based topographic modelling provides essential contextual support for the interpretation and validation of radar-detected paleochannel signatures.

F

Code availability and statement on the use of artificial intelligence

Code availability

The Python scripts developed for the processing, analysis, retrieval workflows, and figure generation presented in this thesis are publicly available at: https://github.com/femke2001/MSc-Thesis.git The repository is provided to support transparency and reproducibility of the presented results.

Use of artificial intelligence

Generative artificial intelligence (AI) tools were used during the preparation of this thesis as writing-support and programming-assistance tools. These tools were primarily used to improve readability and clarity of text, identify grammatical issues, assist with scientific writing, and support code development and debugging.

All scientific analyses, methodological decisions, data processing, results, interpretations, figures, and conclusions were developed, evaluated, and verified by the author. AI-generated content was critically reviewed and edited before inclusion in the thesis. No AI tools were used to generate, analyse, or interpret the BIOMASS data independently, and all scientific responsibility for the content of this thesis remains with the author.